Pacific Northwest
NATIONAL LABORATORY

PNNL-38580, Rev. 0
WTPSP-RPT-261, Rev. 0

Compositing and Characterization of SE Quadrant Waste Exemplars

December 2025

Richard C Daniel
Carolyne A Burns
Amy M Westesen
Austin A Bachmann
Juan S Avila
Reid A Peterson

U.S. DEPARTMENT of ENERGY

Prepared for the U.S. Department of Energy under
Contract DE-AC05-76RL01830

DISCLAIMER

This report was prepared as an account of work sponsored by an agency of the United States Government. Neither the United States Government nor any agency thereof, nor Battelle Memorial Institute, nor any of their employees, makes **any warranty, express or implied, or assumes any legal liability or responsibility for the accuracy, completeness, or usefulness of any information, apparatus, product, or process disclosed, or represents that its use would not infringe privately owned rights.** Reference herein to any specific commercial product, process, or service by trade name, trademark, manufacturer, or otherwise does not necessarily constitute or imply its endorsement, recommendation, or favoring by the United States Government or any agency thereof, or Battelle Memorial Institute. The views and opinions of authors expressed herein do not necessarily state or reflect those of the United States Government or any agency thereof.

PACIFIC NORTHWEST NATIONAL LABORATORY
operated by
BATTELLE
for the
UNITED STATES DEPARTMENT OF ENERGY
under Contract DE-AC05-76RL01830

Printed in the United States of America

Available to DOE and DOE contractors from
the Office of Scientific and Technical Information,
P.O. Box 62, Oak Ridge, TN 37831-0062
www.osti.gov
ph: (865) 576-8401
fax: (865) 576-5728
email: reports@osti.gov

Available to the public from the National Technical Information Service
5301 Shawnee Rd., Alexandria, VA 22312
ph: (800) 553-NTIS (6847)
or (703) 605-6000
email: info@ntis.gov
Online ordering: http://www.ntis.gov

PNNL-38580, Rev. 0
WTPSP-RPT-261, Rev. 0

Compositing and Characterization of SE Quadrant Waste Exemplars

December 2025

Richard C Daniel
Carolyne A Burns
Amy M Westesen
Austin A Bachmann
Juan S Avila
Reid A Peterson

Prepared for
the U.S. Department of Energy
under Contract DE AC05 76RL01830

Pacific Northwest National Laboratory
Richland, Washington 99354

Summary

This report outlines the experimental investigation and characterization of transport properties in Hanford Southeast (SE) quadrant High-Level Waste. The goal of the study was to establish baseline behaviors of bulk composite rheology and settling characteristics to facilitate waste treatment process design for the Waste Treatment and Immobilization Plant (WTP) and to avoid waste conditions and properties that could challenge pipeline transport and vessel mixing operations.

The study focused on two major objectives: 1) identifying, obtaining, and preparing relevant Hanford tank waste samples for evaluation and 2) quantifying the "as-received" rheology and transport properties of the samples. Twenty-three centrifuged core segments originating from tanks AN-101, AN-106, and AW-105 were selected based on compositional relevance to SE quadrant PUREX cladding waste. These materials were composited into five waste composites enriched with target analytes: aluminum (Al), iron (Fe), phosphate (PO_4), uranium (U), and zirconium (Zr).

Physical property and transport testing examined particle size distributions, bulk densities, settling behaviors, rheological properties, shear strengths, and just-suspended mixing speeds (NJS). Testing revealed two distinct composite classifications based on rheological characteristics: non-Newtonian composites (Fe and PO_4) and Newtonian composites (Al, U, and Zr). The Fe and PO_4 composites exhibited slow settling rates and reduced mobilization proclivity, attributable to strong particle-particle interactions and the formation of yield structures within non-Newtonian slurries. In contrast, the Al, U, and Zr composites displayed rapid settling and dense compaction behaviors, indicative of minimal structuring and interactions.

Shear strengths for all composites were generally low relative to prior studies of SE quadrant waste, with only the U composite showing elevated strength approaching values reported in previous literature. Repeat shear strength measurements revealed contributions from dense granular material in the U composite and stronger cohesive properties in the Al composite. Settling data highlighted hindered settling behavior, with rates falling more than one order of magnitude below estimates based on Stokes' law and rate decreasing as composite undissolved solids content increased.

NJS testing demonstrated different mobilization behaviors between cohesive and granular composites. The Fe composite required the highest mixing rate for resuspension, while the Al composite was the easiest to resuspend. Comparison of measured NJS against predictions made using the Zwietering correlation suggests non-Newtonian behavior alters resuspension mechanics, rendering non-Newtonian systems more stable against resuspension lift forces relative to their granular counterparts.

Overall, the present study identified divergent transport behaviors for SE quadrant wastes as a function chemistry for the five chemistries evaluated (Al, Fe, PO_4, U, and Zr). And while unique combination of transport properties (e.g., NJS, settling, rheology) were observed for each chemistry studied, as noted in preceding paragraphs, their overall behaviors can be broadly categorized by rheology, with the non-Newtonian Fe and PO_4 composites exhibiting low-rates of settling, low shear strengths on the order of 10 Pa, and large NJS (relative to expectations) and the Al, U, and Zr Newtonian composites exhibiting fast behavior, larger shear strengths, and NJS in-line with expectations based on composite solid density and size. This broad behavior reflects Fe- and PO_4-specific particle chemistries and sizes that promote the formation low density, space-filling structures with packing fractions on the order of 10 % by volume. These low density structures limit solids compaction, lead to emergent non-Newtonian rheology, appear to stabilize settled beds against gradual erosion by overhead mixing, and limit overall settled bed strength in shear to $\sim$50 Pa or less. The confluence of observed behaviors for the Fe and PO_4 composites suggests potential challenges in the mixing and transport of iron and natrophosphate-rich wastes, and more broadly, for wastes exhibiting non-Newtonian rheology.

The findings of the present study provide a foundational framework for analyzing SE quadrant waste transport properties and developing predictive models for settling rates, mobilization, and operational parameters. Future work will focus on studying the effects of waste blending and incorporation of glass-forming chemicals. Year-two activities will continue to refine data and models, enabling enhanced waste transport management for WTP operations.

Acknowledgments

This study was sponsored by Bechtel National, Inc. (BNI). The authors extend their heartfelt gratitude to John Reyff of BNI for his invaluable support and guidance throughout the course of this work. Additional thanks are due to Justin Slone of Pacific Northwest National Laboratory (PNNL), Michael Lindberg and Daniel Sparks of Hanford Laboratory Management and Integration, and Matthew Landon of Hanford Tank Waste Operations and Closure (H2C) [formerly Washington River Protection Solutions] for their critical role in identifying, procuring, and shipping the 24 Hanford waste core segments used in this study. The authors also acknowledge the dedicated efforts of the PNNL Shielded Facility Operations staff, including Johnny Trevino, Jordan Condray, Hollan Brown, Victor Aguilar, Erick Larios, and Michael Rojas, whose expertise in handling and characterizing the waste samples was instrumental to the success of this study. Quality assurance for this report was overseen by David MacPherson, whose guidance as the quality engineer ensured adherence to high standards. Independent reviews conducted by Heather Colburn and Jesse Willett provided additional rigor and precision to the document. Administrative support for this effort was graciously provided by Chrissy Charron.

This report was edited with the assistance of the PNNL AI Incubator. The AI Incubator's contributions included enhancing the document's grammar, refining technical clarity, and elevating its professional tone. AI-assisted document revisions preceded programmatic technical and quality reviews.

Acronyms and Abbreviations

APA	Automated Particle Analysis
ASO	Analytical Services Organization
BNI	Bechtel National, Inc.
DFHLW	Direct Feed High Level Waste
DI	Deionized (Water)
DS	Dissolved Solids
DOE	U.S. Department of Energy
EDS	X-Ray Energy Dispersive Spectroscopy
H2C	Hanford Tank Waste Operations and Closure
HDPE	High Density Polyethylene
HLMI	Hanford Laboratory Management and Integration, LLC
HLW	High Level Waste
NJS	Just-Suspended Mixing Speed
NQAP	Nuclear Quality Assurance Program
IC	Ion Chromatography
ICP-OES	Inductively Coupled Plasma Optical Emission Spectroscopy
LH	Lower-Half (of a Core Segment)
PNNL	Pacific Northwest National Laboratory
PSD	Particle Size Distribution
PSDD	Particle Size Density Distribution
PTF	Pretreatment Facility
RPL	Radiochemical Processing Laboratory
SAL	Shielded Analytical Laboratory
SE	Southeast
TIC	Total Inorganic Carbon
TOC	Total Organic Carbon
TS	Total Solids
UDS	Undissolved Solids
UH	Upper-Half (of a Core Segment)
WTP	Waste Treatment and Immobilization Plant

Contents

Contents vi

List of Figures ix

List of Tables xiv

1 Introduction 1

1.1 Objectives . . . 2

1.2 Approach . . . 2

2 Quality Assurance 4

3 Waste Selection and Compositing Strategy 5

4 Waste Receipt and Compositing 14

4.1 Sample Receipt . . . 14

4.2 Initial Inspection . . . 14

4.3 Compositing Activities . . . 18

4.4 Compositing Results . . . 24

5 Characterization Methods and Basis 28

5.1 Composite Chemistry . . . 28

5.2 Particle Size Distribution . . . 29

5.3 Flow Behavior . . . 30

5.4 Shear Strength . . . 31

5.5 Settling Rate, Settled Solids Volume, and Sludge Density . . . 34

5.6 Composite Serial Dilution . . . 36

5.7 Composite Transfers and Sampling . . . 37

6 Results and Discussion 38

6.1 Solid and Liquid Phase Chemistry . . . 38

6.2 Particle Size Distribution . . . 38

6.3 Solid Phase Density . . . 43

6.4 Flow Curve and Shear Strength . . . 43

6.5 Settling Volumes, Rates, and Density 50
6.6 NJS 58

7 Conclusions 61
7.1 Waste Selection and Receipt 61
7.2 Waste Compositing 61
7.3 Physical Property and Transport Testing 63
7.4 Key Takeaways and Next Steps 66

8 References 68

A Waste Sample Jar Inspection A.1
A.1 Tank AN-101, Core Segment 340-12 LH A.2
A.2 Tank AN-101, Core Segment 340-12 UH A.4
A.3 Tank AN-101, Core Segment 340-13 LH A.6
A.4 Tank AN-101, Core Segment 340-13 UH A.8
A.5 Tank AN-101, Core Segment 340-14 UH A.10
A.6 Tank AN-101, Core Segment 340-18 LH A.12
A.7 Tank AN-101, Core Segment 340-18 UH A.14
A.8 Tank AN-101, Core Segment 340-19 LH A.16
A.9 Tank AN-106, Core Segment 339-14 . . . . . A.18
A.10 Tank AN-106, Core Segment 339-15 LH A.20
A.11 Tank AN-106, Core Segment 339-15 UH A.22
A.12 Tank AN-106, Core Segment 339-16 LH A.24
A.13 Tank AN-106, Core Segment 339-16 UH A.26
A.14 Tank AN-106, Core Segment 339-18 UH A.28
A.15 Tank AN-106, Core Segment 339-19 LH A.30
A.16 Tank AN-106, Core Segment 339-19 UH A.32
A.17 Tank AN-106, Core Segment 339-20 UH A.34
A.18 Tank AN-106, Core Segment 339-21 UH A.36
A.19 Tank AN-106, Core Segment 339-22 UH A.38
A.20 Tank AW-105, Core Segment 322-8 LH A.40
A.21 Tank AW-105, Core Segment 322-8 LH A.42
A.22 Tank AW-105, Core Segment 322-8 UH A.44
A.23 Tank AW-105, Core Segment 322-8R2 CS 1 . . . . . A.46

A.24 Tank AW-105, Core Segment 322-8R2 CS 2 . . . . . A.48

B Composite Settling Curves **B.1**

C Composite Flow Curves **C.1**

List of Figures

1 Distribution of select analyte concentrations observed in the centrifuged liquid portion of AN-101, AN-106, and AW-105 core segments. . . . 7
2 Distribution of select analyte concentrations observed in the undissolved (insoluble) solids fraction of centrifuged solids of AN-101, AN-106, and AW-105 core segments. . . . 7
3 Per-core centrifuged solids concentrations for six selected analytes of interest. . . . 10
4 Image of solids within Jar 21415 (AN-101 Segment 18 LH). . . . 15
5 Image of solids within Jar 21006 (AN-106 Segment 15 LH). . . . 15
6 Image of solids within Jar 20507 (AW-105 Segment 8R2). . . . 16
7 Image of solids within Jar 21378 (AN-101 Segment 13 LH). . . . 16
8 Image of solids within Jar 21404 (AN-101 Segment 13 UH). . . . 17
9 Image of solids within Jar 20326 (AW-105 Segment 8 LH). . . . 17
10 Comparison of estimated and actual (as measured) composite solid chemistries. . . . 26
11 Comparison of estimated and actual composite solid chemistries for primary analytes with PO_4 excluded. . . . 27
12 Typical shear strength experimental setup. . . . 32
13 Example shear strength torque versus time curve. . . . 33
14 Example settling rate measurement showing the evolution of settled solids volume as a function of time. . . . 35
15 Fractional solid-phase composition for the five composites. . . . 39
16 Volume-based size distributions for key analyte-associated mineral phases. . . . 40
17 Estimated size distributions for the five SE quadrant waste composites. . . . 42
18 Example flow curve for the 20 % Fe composite showing non-Newtonian behavior. . . . 45
19 Example flow curve for the 20 % U composite showing Newtonian behavior. . . . 46
20 A worst-case example of “binding” behavior observed in 20 % composite testing. . . . 47
21 Measured SE quadrant composite rheology as a function of UDS content. . . . 48
22 Measured settling curves for Al composites. . . . 51
23 Measured settling curves for all nominally 10 % composites. . . . 51
24 Measured linear settling rates for the five SE quadrant composites as a function of UDS content. . . . 53
25 Measured 24 h settled solids volume percents for the five SE quadrant wastes as a function of UDS content. . . . 54

26 Volume percent of solids within the settled layer for the five SE quadrant waste composites as a function of UDS content. 56

27 Measured linear settling rates as a function of the reduced volume fraction solids content of the composite. 57

28 Parity plot comparing measured and predicted NJS values for the SE quadrant composites. . 59

A.1 Side view of Jar 21402 (Tank AN-101, Core Segment 340-12 LH) A.2

A.2 Bottom view of Jar 21402 (Tank AN-101, Core Segment 340-12 LH) A.3

A.3 Solids view of Jar 21402 (Tank AN-101, Core Segment 340-12 LH) A.3

A.4 Side view of Jar 21403 (Tank AN-101, Core Segment 340-12 UH) A.4

A.5 Bottom view of Jar 21403 (Tank AN-101, Core Segment 340-12 UH) A.5

A.6 Solids view of Jar 21403 (Tank AN-101, Core Segment 340-12 UH) A.5

A.7 Side view of Jar 21378 (Tank AN-101, Core Segment 340-13 LH) A.6

A.8 Bottom view of Jar 21378 (Tank AN-101, Core Segment 340-13 LH) A.7

A.9 Solids view of Jar 21378 (Tank AN-101, Core Segment 340-13 LH) A.7

A.10 Side view of Jar 21404 (Tank AN-101, Core Segment 340-13 UH) A.8

A.11 Bottom view of Jar 21404 (Tank AN-101, Core Segment 340-13 UH) A.9

A.12 Solids view of Jar 21404 (Tank AN-101, Core Segment 340-13 UH) A.9

A.13 Side view of Jar 21407 (Tank AN-101, Core Segment 340-14 UH) A.10

A.14 Bottom view of Jar 21407 (Tank AN-101, Core Segment 340-14 UH) A.11

A.15 Solids view of Jar 21407 (Tank AN-101, Core Segment 340-14 UH) A.11

A.16 Side view of Jar 21415 (Tank AN-101, Core Segment 340-18 LH) A.12

A.17 Bottom view of Jar 21415 (Tank AN-101, Core Segment 340-18 LH) A.13

A.18 Solids view of Jar 21415 (Tank AN-101, Core Segment 340-18 LH) A.13

A.19 Side view of Jar 21416 (Tank AN-101, Core Segment 340-18 UH) A.14

A.20 Bottom view of Jar 21416 (Tank AN-101, Core Segment 340-18 UH) A.15

A.21 Solids view of Jar 21416 (Tank AN-101, Core Segment 340-18 UH) A.15

A.22 Side view of Jar 21417 (Tank AN-101, Core Segment 340-19 LH) A.16

A.23 Bottom view of Jar 21417 (Tank AN-101, Core Segment 340-19 LH) A.17

A.24 Solids view of Jar 21417 (Tank AN-101, Core Segment 340-19 LH) A.17

A.25 Side view of Jar 20913 (Tank AN-106, Core Segment 339-14) A.18

A.26 Bottom view of Jar 20913 (Tank AN-106, Core Segment 339-14) A.19

A.27 Solids view of Jar 20913 (Tank AN-106, Core Segment 339-14) A.19

A.28 Side view of Jar 21006 (Tank AN-106, Core Segment 339-15 LH) A.20

A.29 Bottom view of Jar 21006 (Tank AN-106, Core Segment 339-15 LH) A.21

A.30 Solids view of Jar 21006 (Tank AN-106, Core Segment 339-15 LH) A.21
A.31 Side view of Jar 20918 (Tank AN-106, Core Segment 339-15 UH) A.22
A.32 Bottom view of Jar 20918 (Tank AN-106, Core Segment 339-15 UH) A.23
A.33 Solids view of Jar 20918 (Tank AN-106, Core Segment 339-15 UH) A.23
A.34 Side view of Jar 21314 (Tank AN-106, Core Segment 339-16 LH) A.24
A.35 Bottom view of Jar 21314 (Tank AN-106, Core Segment 339-16 LH) A.25
A.36 Solids view of Jar 21314 (Tank AN-106, Core Segment 339-16 LH) A.25
A.37 Side view of Jar 21315 (Tank AN-106, Core Segment 339-16 UH) A.26
A.38 Bottom view of Jar 21315 (Tank AN-106, Core Segment 339-16 UH) A.27
A.39 Solids view of Jar 21315 (Tank AN-106, Core Segment 339-16 UH) A.27
A.40 Side view of Jar 21357 (Tank AN-106, Core Segment 339-18 UH) A.28
A.41 Bottom view of Jar 21357 (Tank AN-106, Core Segment 339-18 UH) A.29
A.42 Solids view of Jar 21357 (Tank AN-106, Core Segment 339-18 UH) A.29
A.43 Side view of Jar 21360 (Tank AN-106, Core Segment 339-19 LH) A.30
A.44 Bottom view of Jar 21360 (Tank AN-106, Core Segment 339-19 LH) A.31
A.45 Solids view of Jar 21360 (Tank AN-106, Core Segment 339-19 LH) A.31
A.46 Side view of Jar 21361 (Tank AN-106, Core Segment 339-19 UH) A.32
A.47 Bottom view of Jar 21361 (Tank AN-106, Core Segment 339-19 UH) A.33
A.48 Solids view of Jar 21361 (Tank AN-106, Core Segment 339-19 UH) A.33
A.49 Side view of Jar 21362 (Tank AN-106, Core Segment 339-20 UH) A.34
A.50 Bottom view of Jar 21362 (Tank AN-106, Core Segment 339-20 UH) A.35
A.51 Solids view of Jar 21362 (Tank AN-106, Core Segment 339-20 UH) A.35
A.52 Side view of Jar 21366 (Tank AN-106, Core Segment 339-21 UH) A.36
A.53 Bottom view of Jar 21366 (Tank AN-106, Core Segment 339-21 UH) A.37
A.54 Solids view of Jar 21366 (Tank AN-106, Core Segment 339-21 UH) A.37
A.55 Side view of Jar 21367 (Tank AN-106, Core Segment 339-22 UH) A.38
A.56 Bottom view of Jar 21367 (Tank AN-106, Core Segment 339-22 UH) A.39
A.57 Solids view of Jar 21367 (Tank AN-106, Core Segment 339-22 UH) A.39
A.58 Side view of Jar 19257 (Tank AW-105, Core Segment 322-8 LH) A.40
A.59 Bottom view of Jar 19257 (Tank AW-105, Core Segment 322-8 LH) A.41
A.60 Solids view of Jar 19257 (Tank AW-105, Core Segment 322-8 LH) A.41
A.61 Side view of Jar 20326 (Tank AW-105, Core Segment 322-8 LH) A.42
A.62 Bottom view of Jar 20326 (Tank AW-105, Core Segment 322-8 LH) A.43
A.63 Solids view of Jar 20326 (Tank AW-105, Core Segment 322-8 LH) A.43

A.64 Side view of Jar 19262 (Tank AW-105, Core Segment 322-8 UH) A.44
A.65 Bottom view of Jar 19262 (Tank AW-105, Core Segment 322-8 UH) A.45
A.66 Solids view of Jar 19262 (Tank AW-105, Core Segment 322-8 UH) A.45
A.67 Side view of Jar 20507-1 (Tank AW-105, Core Segment 322-8R2 CS 1) A.46
A.68 Bottom view of Jar 20507-1 (Tank AW-105, Core Segment 322-8R2 CS 1) A.47
A.69 Solids view of Jar 20507-1 (Tank AW-105, Core Segment 322-8R2 CS 1) A.47
A.70 Side view of Jar 20507-2 (Tank AW-105, Core Segment 322-8R2 CS 2) A.48
A.71 Bottom view of Jar 20507-2 (Tank AW-105, Core Segment 322-8R2 CS 2) A.49
A.72 Solids view of Jar 20507-2 (Tank AW-105, Core Segment 322-8R2 CS 2) A.49

B.1 Measured settling curves for Al composites. B.2
B.2 Measured settling curves for Fe composites. B.2
B.3 Measured settling curves for PO_4 composites. B.3
B.4 Measured settling curves for U composites. B.3
B.5 Measured settling curves for Zr composites. B.4
B.6 Measured settling curves for all nominally 5 % composites. B.4
B.7 Measured settling curves for all nominally 10 % composites. B.5
B.8 Measured settling curves for all nominally 15 % composites. B.5
B.9 Measured settling curves for all nominally 20 % composites. B.6

C.1 Measured down-ramp flow curve for the 5 % UDS Fe composite. C.2
C.2 Measured down-ramp flow curve for the 3.7 % UDS PO_4 composite. C.2
C.3 Measured down-ramp flow curve for the 5 % UDS Zr composite. C.3
C.4 Measured down-ramp flow curve for the 10 % UDS Fe composite. C.3
C.5 Measured down-ramp flow curve for the 7.3 % UDS PO_4 composite. C.4
C.6 Measured down-ramp flow curve for the 10 % UDS Zr composite. C.4
C.7 Measured down-ramp flow curve for the 15 % UDS Al composite. C.5
C.8 Measured down-ramp flow curve for the 15 % UDS Fe composite. C.5
C.9 Measured down-ramp flow curve for the 11.0 % UDS PO_4 composite. C.6
C.10 Measured down-ramp flow curve for the 15 % UDS U composite. C.6
C.11 Measured down-ramp flow curve for the 15 % UDS Zr composite. C.7
C.12 Measured down-ramp flow curve for the 20 % UDS Fe composite. C.7
C.13 Measured down-ramp flow curve for the 20 % UDS Fe composite. C.8
C.14 Measured down-ramp flow curve for the 14.6 % UDS PO_4 composite. C.8
C.15 Measured down-ramp flow curve for the 20 % UDS U composite. C.9

C.16 Measured down-ramp flow curve for the 20 % UDS Zr composite. C.9

List of Tables

1 Tank AN-101, AN-106, and AW-105 core segments sourced for the present study. 5
2 Association of samples used to derive exemplar SE quadrant wastes. 11
3 Individual solids chemistries of associated SE exemplars. 11
4 Simplified supernatant compositions for six SE quadrant waste sub-chemistries. 12
5 Estimated solid compositions for the six SE quadrant waste sub-chemistries. 12
6 Simplified supernatant properties for the six SE quadrant sub-chemistries. 13
7 Chemical recipes used to prepare simulated supernatants for the five composite sub-chemistries tested. 19
8 Measured composition of the as-prepared simulated supernatant. 19
9 Measured properties for the as-made simulated supernatant liquids. 19
10 Mass of solids recovered for each composite sub-chemistry. 21
11 Composite dilution schedule for a target UDS of 25 %. 21
12 As-measured Stage 1 dilution composite UDS and DS contents. 22
13 Stage 2 composite dilutions as originally planned. 24
14 Final as-prepared “20 %” UDS composite masses and solid contents. 24
15 Comparison of estimated and measured (actual) composite chemistry for the five prepared SE waste exemplars. 25
16 Summary of physical and chemical characterization techniques used to assess transport and transport-relevant properties of the five Hanford SE waste composites. 28
17 Analytical methods requested for composite and simulated supernatant samples. 29
18 AN-101, AN-106, and AW-105 waste jar samples for particle size analysis. 30
19 Vane immersion depth and container geometry constraints for shear strength tests using the vane technique. 34
20 UDS contents realized during serial dilution of the PO_4 composite. 37
21 Summary of measured (actual) composite solid and liquid phase chemistry. 39
22 Association of target analytes with mineral phases identified in Buck et al. (2025). 40
23 Estimate of solid phase bulk density for each composite. 43
24 Summary of constitutive rheological parameters for the five SE quadrant composites. 44
25 Shear strength measurements for 20 % composites. 49
26 Slurry density measurements derived from 100 mL volumetric settling flask characterization. 52

27 Linear settling rate estimates for the five SE quadrant wastes as a function of UDS content. 52

28 Percent settled solid volumes after approximately 24 h of settling as a function of composite UDS concentration. 53

29 Composite terminal settling velocity and the parameters used to estimate it. 55

30 Comparison of measured and estimated NJS for the five SE quadrant wastes. 59

31 Summary of measured (actual) composite solid and liquid phase chemistry. 62

32 High-level summary of SE waste exemplar transport properties. 67

C.1 Summary of measured flow curves for the SE quadrant composites. C.1

1.0 Introduction

The U.S. Department of Energy's (DOE's) Hanford Site in southeastern Washington State stores approximately 55 million gallons of legacy nuclear defense waste. The current disposition pathway for these wastes involves immobilizing the radioactive components in a glass matrix (i.e., vitrifying the waste) at Hanford's Waste Treatment and Immobilization Plant (WTP). High-Level Waste (HLW) sludges containing high insoluble solids content comprise a significant quantity of the waste (~20 % by volume). Historically, these sludges have been subjected to planned chemical alteration and sludge washing processes at WTP's Pretreatment Facility (PTF) to remove glass-limiting analytes, such as aluminum and chromium, prior to vitrification. Advances in waste form chemistry have relaxed waste-loading requirements, enabling direct feed of "unaltered" HLW to WTP's HLW melter.

The design of the HLW melter feed preparation and melter feed vessels is based on a melter feed rheology range defined by Bingham consistencies of 0.4 to 40 mPa s, Bingham yield stresses below 30 Pa, and settled solids shear strengths below 625 Pa (24590-HLW-MVC-HFP-00001, 2021; Poloski et al., 2006). Melter feed rheological data are limited, and those available are derived primarily from melter feed using pre-treated (washed and leached) sludges (Bredt and Swoboda, 2000; Bredt et al., 2003). Consequently, the WTP project will quantify melter feed rheology using waste feed qualification samples that undergo prototypic pretreatment and melter feed preparation. If the rheology of a qualification sample falls outside the acceptable range, corrective process actions will be required to bring the feed into compliance. Simple dilution may serve as one corrective measure; however, altering melter feed chemistry carries inherent risk. Dilution can significantly change solution chemistry and, in some cases, inadvertently increase feed rheology, such as through the precipitation of additional solids.

WTP vessels and transfer lines are subject to critical deposition velocity requirements to maintain the suspension of dense solid particles, prevent pipeline plugs, and limit the accumulation of dense solids in melters at the HLW vitrification facility. Assessments of critical deposition velocity can be conducted either via direct calculation using standard equations—such as the Oroskar-Turian correlation for deposition velocity (Oroskar and Turian, 1980)—or through direct testing in a feed qualification loop. The calculation-based approach relies on accurate knowledge of the waste particle size density distribution (PSDD). However, measured PSDD values often display broad distributions and are subject to significant uncertainty with respect to density. Such uncertainty drives conservative design approaches, necessitating robust testing.

While feed qualification testing can reduce uncertainties related to waste rheology and transport properties prior to sludge treatment at the WTP HLW Facility, such testing has the potential to delay melter feed delivery. This is particularly true if iterative testing is required to identify optimal feed adjustment strategies, such as appropriate dilution or blending of wastes to reduce critical deposition velocity.

An alternative approach involves performing rheological and transport evaluations on as-received wastes, blended wastes, and melter feeds well in advance of operations. These data could be utilized to develop first-order models to relate critical waste attributes—such as solids concentration, pH, and waste feed type—and acceptable transport properties. Historically, correlation between Hanford waste simulants and the transport properties of actual Hanford melter feeds has been largely coincidental, as noted by Matlack et al. (2005). Therefore, testing of melter feed transport properties requires the use of actual waste sludges rather than simulated materials.

The DOE is currently evaluating the feasibility of direct feed high-level waste (DFHLW), which would allow HLW vitrification to proceed without requiring the PTF. This study recommends the use of DFHLW-based melter feeds derived from a variety of Hanford southeast (SE) quadrant waste sludges in place of simulated sludge wastes. Establishing transport models based on actual wastes would enable the

preparation of rheologically acceptable waste feeds with improved accuracy and timely operations, mitigating the iterative testing process. Furthermore, if these models are sufficiently validated, upfront research could eliminate the need for melter feed rheology and transport property qualification tests on waste feed qualification samples—a significant improvement in operational efficiency.

1.1 Objectives

The present study is part of a larger multi-year program aimed at characterizing Hanford SE quadrant tank waste and waste melter feed rheology (e.g., viscosity, yield strength, and consistency) alongside transport properties (e.g., critical deposition velocity, settling rates, and just-suspended mixing speed). The primary objective of this characterization effort is twofold:

1. Provide a baseline dataset to evaluate the transport properties of waste blends and waste melter feeds relative to current tank and facility agitator/pumping designs.
2. Inform potential feed alteration strategies to mitigate waste transport and mixing challenges.

To achieve this objective, the study encompasses the following specific activities:

1. Identifying and obtaining relevant SE quadrant wastes for evaluation.
2. Measuring as-received waste rheology and transport properties (e.g., settling rates, just-suspended mixing speed, etc.).
3. Measuring the rheology and transport properties of waste blends.
4. Measuring the rheology and transport properties of waste melter feeds.
5. Developing, where feasible, first-order models to establish strategies for controlling the rheological and transport properties of waste and melter feeds during operations at the WTP HLW Facility.

This report outlines the progress achieved during the first year of the program, specifically focusing on efforts to identify available SE quadrant wastes (Activity #1) and to measure the “as-received” rheological and transport properties of those wastes (Activity #2).

1.2 Approach

For the present study, SE quadrant wastes were selected due to the prevalence of PUREX cladding wastes in this quadrant, which exhibit challenging waste rheology and settling behaviors (Snow et al., 2009). In particular, Snow et al. (2009) observed that PUREX cladding wastes, which contain substantial quantities of Al-bearing solids, settled rapidly and formed high-strength (100 to 1000 Pa) settled layers. More generally, SE quadrant waste also contains (as will be shown in later sections of this report) substantial quantities of high-density solids, including iron, zirconium, and uranium-bearing solids, which may pose challenges for resuspension in vessels and deposition during pipeline transport. Broadly, these waste characteristics are expected to pose end-case challenges related to the transport and resuspension of waste solids during potential DFHLW processing.

An initial review of the available waste inventory identified twenty-three centrifuged waste solid core segments from SE quadrant tanks AN-101, AN-106, and AW-105. These samples were originally collected between 2006–2008 (AW-105) and 2021–2022 (AN-101 and AN-106). With the assistance of staff from Bechtel National, Inc. (BNI), Hanford Tank Waste Operations and Closure (H2C, formerly Washington River Protection Solutions), and Hanford Laboratory Management and Integration (HLMI),

these samples were procured by PNNL for testing. However, no single sample within the set of twenty-three core segments contained sufficient solids for full characterization. Moreover, due to extended storage, many of the samples had lost their associated moisture and appeared as dry granular solids or solidified pucks.

To address these limitations, the core segment solids were combined and rehydrated to yield five composited wastes of sufficient quantity for characterization. Twenty-one of the samples were selectively combined to generate composites enriched in one of five targeted chemistries: natrophosphate, iron, aluminum, uranium, and zirconium. The remaining two samples, enriched in bismuth solids, were excluded from the current study but can potentially be used in the future to create a sixth "bismuth-rich" composite sub-chemistry.

Development of the five waste composites—referred to as "exemplars"—was guided by analytical data from Tanks AN-101, AN-106, and AW-105, as reported in (Jordan, 2022a,b; Disselkamp, 2009). Both the composition of the solids in each composite and the simulated supernatant used to rehydrate the solids were informed by this analytical data. The rheology and transport properties of these five "as-prepared" (untreated) waste composites were quantified as baseline metrics against which waste blending and treatment protocols can be evaluated. This characterization effort sought to identify specific waste chemistries that pose challenges in transport, mixing, and handling, particularly those enriched in aluminum, uranium, and zirconium solids.

The results presented in this report summarize the "as-prepared" measurements and highlight potential challenges associated with SE quadrant wastes. The baseline data collected during year one, along with the methods used to prepare and characterize the composites, are detailed in the following sections. This dataset provides a robust reference point for assessing the transport properties of waste blends and waste melter feeds. When paired with counterpart characterization data collected during subsequent project years, these findings will inform strategies for waste feed alteration to mitigate transport and mixing challenges.

2.0 Quality Assurance

This work was performed in accordance with Pacific Northwest National Laboratory's (PNNL) Nuclear Quality Assurance Program (NQAP). The NQAP adheres to DOE Order 414.1D, *Quality Assurance*, and 10 CFR 830, Subpart A, *Quality Assurance Requirements*. The program employs NQA-1-2012, *Quality Assurance Requirements for Nuclear Facility Applications*, as its consensus standard, and utilizes NQA-1-2012, Subpart 4.2.1, as the basis for its graded approach to quality assurance (NQA-1-2012, 2012).

The NQAP is designed to function in conjunction with PNNL's laboratory-level Quality Management Program, which is rooted in the same requirements established by DOE Order 414.1D and 10 CFR 830, Subpart A.

The activities described in this report were conducted under a technology readiness level of 5. Furthermore, all contributing staff members completed necessary technical and quality assurance training prior to undertaking any work that could impact quality.

3.0 Waste Selection and Compositing Strategy

Start-up of DFHLW treatment campaigns is expected to target wastes stored in Hanford's SE quadrant, specifically the A-, AN-, AP-, AW-, AX-, and AZ-tanks. To provide meaningful transport and handling characterization data for SE quadrant wastes, the present study focused on selecting Hanford waste samples derived from one or more of these tanks.

In 2024, a review of the Laboratory 222-S waste inventory identified twenty-three centrifuged solids core segments from two SE quadrant tanks, AN- and AW-, that were available for evaluation. These core segments originated from in-tank sampling of Hanford tanks AN-101, AN-106, and AW-105. The sampling campaigns spanned 2006 to 2008 for AW-105 samples and 2020 to 2021 for AN-101 and AN-106 samples. The twenty-three core samples, itemized in Table 1, were shipped to PNNL's Shielded Analytical Laboratory (SAL) in 2024 with the support of staff from BNI, H2C, and HLMI.

Table 1. Tank AN-101, AN-106, and AW-105 core segments sourced for the present study. Samples were provided by 222-S in labelled jars. The unique Jar and Sample ID derive from previous sample chemical characterization efforts documented in Jordan (2022a,b) and Disselkamp (2009). Here, UH and LH refer to the upper- and lower-half of each core segment, respectively.

Jar ID	Sample ID	Description	Sample Mass, g
21402	S21T021171	AN-101, Segment 12 LH	69.8
21403	S21T021172	AN-101, Segment 12 UH	13.2
21378	S21R000250	AN-101, Segment 13 LH	57.7
21404	S21T021201	AN-101, Segment 13 UH	57.6
21407	S21T021230	AN-101, Segment 14 UH	15.4
21415	S21T021675	AN-101, Segment 18 LH	44.6
21416	S21T021676	AN-101, Segment 18 UH	100
21417	S21T021747	AN-101, Segment 19 LH	49.4
20913	S20T016919	AN-106, Segment 14	79.4
21006	S20T017241	AN-106, Segment 15 LH	33.3
20918	S20T017242	AN-106, Segment 15 UH	41.5
21314	S20T017587	AN-106, Segment 16 LH	46.7
21315	S20T017588	AN-106, Segment 16 UH	52.4
21357	S20T017662	AN-106, Segment 18 UH	39.6
21360	S20T017884	AN-106, Segment 19 LH	11.4
21361	S20T017885	AN-106, Segment 19 UH	23.2
21362	S20T018179	AN-106, Segment 20 UH	15.3
21366	S20T018217	AN-106, Segment 21 UH	18.4
21367	S20T018254	AN-106, Segment 22 UH	39.5
19257	S06T000221	AW-105, Segment 8 LH	38.4
20326	S06T000217	AW-105, Segment 8 LH	29.3
19262	S06T000220	AW-105, Segment 8 UH	47.9
20507	S08T009997	AW-105, Segment 8R2	88.6

The chemistry of the twenty-three individual core segments listed in Table 1 has been previously characterized. Analytical data for AN-101 samples were reported in (Jordan, 2022a), for AN-106 samples in (Jordan, 2022b), and for AW-105 samples in (Disselkamp, 2009). The AN-101 and AN-106 characterization data from (Jordan, 2022a) and (Jordan, 2022b) provide detailed compositional information, including both centrifuged liquid and centrifuged solids chemistries for each sample segment in Table 1. Additionally, since the chemical data for AN-101 and AN-106 were reported by the same author using consistent sampling and reporting templates, the results for these segments are directly comparable and were combined into a single aggregated chemical dataset.

For the AW-105 core samples utilized in this study, equivalent analytical scope and format to that available for AN-101 and AN-106 samples were not accessible. Specifically, Hanford-sourced chemistry reports for the AW-105 samples listed in Table 1 could not be reliably and confidently matched to corresponding data in the literature. The closest available data were found in Disselkamp (2009), a 2009 report that includes liquid chemistry results for core segments sampled in 2006, such as the segment labeled "8L." While this report provides data that appear similar to liquid data for Segment UH (listed as S06T000217 in Table 1), the results in (Disselkamp, 2009) cannot be unambiguously connected to the segments procured for this study. Moreover, the data weakly associated with AW-105 samples, such as those for "8L," only include composition measurements for the liquid fraction, with no reported data for centrifuged or slurry solids.

As a result, in the absence of direct analytical data for the sourced AW-105 samples, estimates of AW-105 core sample chemistries were derived from the 2008 best-basis inventory estimate as reported in Disselkamp (2009).

Although AN-101, AN-106, and AW-105 are all SE quadrant waste tanks, significant variations in chemistry are observed both between tanks and within individual tanks as a function of sample depth. This variability is consistent with the heterogeneous chemical characteristics commonly observed across all Hanford tanks.

Figures 1 and 2 present violin plots illustrating the distribution of key analyte concentrations in the liquid and solid fractions of core segments from AN-101, AN-106, and AW-105 tanks. These plots provide insights into the variability in analyte concentrations across the tank core segments. Specifically, for each analyte, the minimum, median, and maximum concentrations are indicated by blue horizontal bars. The distribution of analyte concentrations is shown as shaded blue regions based on relevant centrifuged liquid data reported in Jordan (2022a,b) and Disselkamp (2009).

The analyte concentrations shown in Figure 2 are normalized to a per-gram basis of dry centrifuged solids, a measurement that may include both undissolved (insoluble) solids and potentially soluble salts originating from dried interstitial liquid.

Regarding the liquid phase chemistry, the ranges for the most common liquid phase analytes—namely, aluminate [$Al(OH)_4^-$], nitrite/nitrate, carbonate, and sulfate—are broad, spanning at least two orders of magnitude. This variability is associated with differences in both the overall soluble salt content (or moisture content) and the concentration of individual analytes. The total sodium molarity of wastes, a commonly used metric for waste ion content, varies from approximately 1 to 8 M, with an average of 4.4 M. Free hydroxide concentrations range from 0.016 to 2.4 M, with an average of 0.8 M.

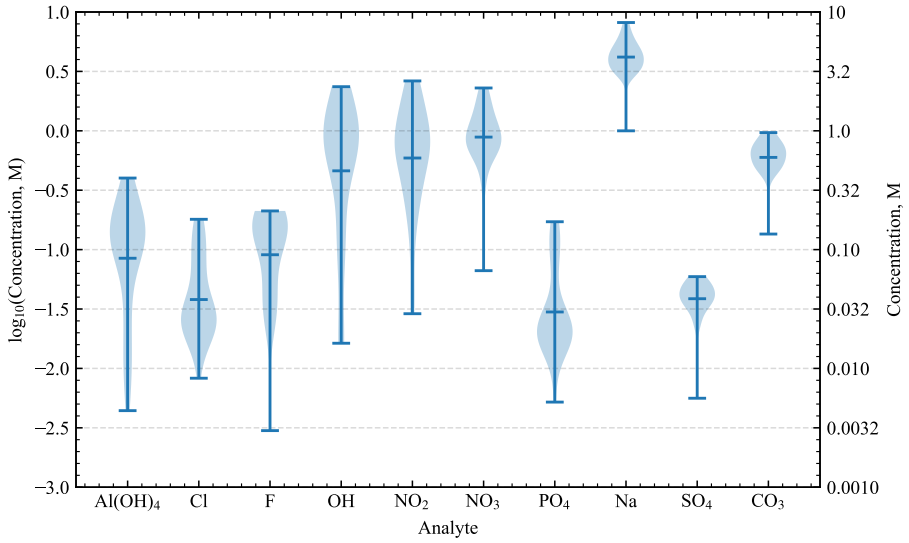


Figure 1. Distribution of select analyte concentrations observed in the centrifuged liquid portion of AN-101, AN-106, and AW-105 core segments listed in Table 1. Concentrations are reported in molarity (i.e., moles analyte per liter liquid). Blue horizontal bars indicate the minimum, median, and maximum analyte concentrations, while the shaded blue regions represent the distribution of analyte concentrations.

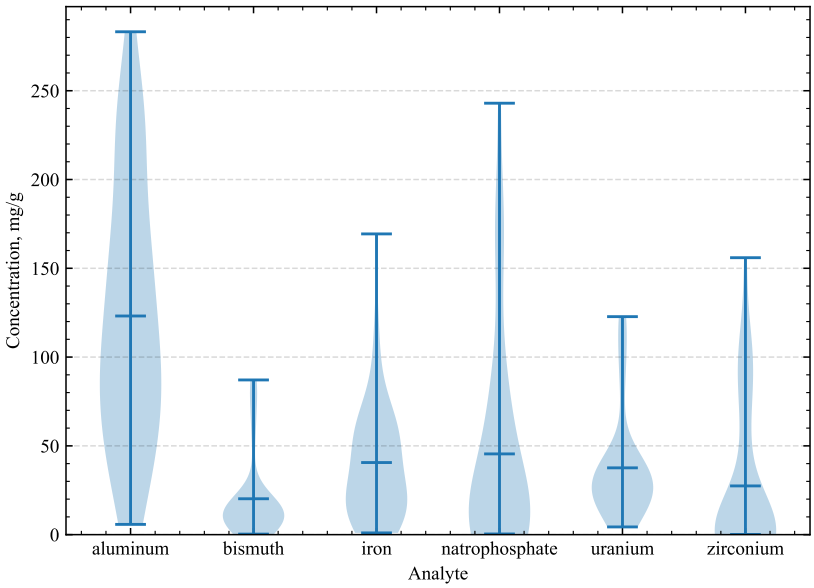


Figure 2. Distribution of select analyte concentrations observed in the undissolved (insoluble) solids fraction of centrifuged solids of AN-101, AN-106, and AW-105 core segments listed in Table 1. Concentrations are reported in milligrams of analyte per gram of dry centrifuged solid. Blue horizontal bars indicate the minimum, median, and maximum analyte concentrations, while the shaded blue regions represent the distribution of analyte concentrations.

Notably, the maximum concentrations of other common analytes approach—or, in the case of two analytes, exceed—their reported solubility limits in waste, as documented by Barney (1976):

- Aluminate: Maximum concentration 0.4 M (Solubility limit: 0.70 M)
- Nitrate: Maximum concentration 2.6 M (Solubility limit: 3.9 M)
- Nitrite: Maximum concentration 2.3 M (Solubility limit: 4.19 M)
- Carbonate: Maximum concentration 0.96 M (Solubility limit: 0.27 M)
- Sulfate: Maximum concentration 0.059 M (Solubility limit: 0.0453 M)

For comparison, solubility limits are estimated based on Sample 3A at 20 °C reported in Table IV of Barney (1976). This sample has a total free hydroxide content of 1.26 M, making it closest to the average reported in Figure 1. However, caution should be exercised when comparing solubility results from Barney (1976) to the maximum liquid concentrations reported herein, as the ion backgrounds may differ substantially. In particular, the simulated wastes in Barney (1976) did not contain salts with F^-, PO_4^{-3}, or Cl_1^-, which limits the present report's ability to direct compare Figure 1 analyte contents against solubility limits. As natrophosphate-rich wastes are of particular interest to the present report, the typical range of dissolved F^- and PO_4^{3-} anions contents derived from the natrophosphate salt ($Na_7(PO_7)_2F \cdot 19\,H_2O$) is also of interest. Recent studies by Mahoney et al. (2020) and Westesen et al. (2023, 2025) explore waste typical ranges for natrophosphate derived F^- and PO_4^{3-}. As should be expected, natrophosphate solubility and dissolution equilibrium depends on the respective contents of Na^+, F^-, and PO_4^{3-}. For wastes with 3.5 M Na, Westesen et al. (2023) model the covariation in soluble fluoride and phosphate as:

$$c_{PO_4} = -7923 \ln(c_F) + 42192, \quad (1)$$

where c_{PO_4} and c_F are the concentrations phosphate and fluoride in solution, respectively, and have units of $\mu g\,mL^{-1}$. Using this expression in conjunction with the observed range of F^- contents in Figure 1 ($\sim$0.003 to 0.2 M), the range of estimated dissolved PO_4^{3-} contents is found to be $\sim$0.017 to 0.23 M. This range falls near the order of magnitude observed in PO_4^{3-} variation within Figure 1 of $\sim$0.005 to 0.18 M.

In the solid phase, Figure 2 emphasizes the contributions of key SE quadrant solid waste analytes, specifically natrophosphate (referred to hereafter as simply PO_4), , bismuth, uranium, aluminum, iron, and zirconium. Among these solids, aluminum-bearing solids exhibit the largest median contributions, at 120 $mg\,g^{-1}$ (or 12 % by mass). Aluminum content displays a broad variance, ranging from 10 to 280 $mg\,g^{-1}$. Iron, zirconium, uranium, and phosphate solids have similar median contributions of 30 to 40 $mg\,g^{-1}$, though their distributions differ slightly. Iron, zirconium, and phosphate exhibit a wider range of solid concentrations compared to uranium, with phosphate showing the largest maximum concentration of 240 $mg\,g^{-1}$. Bismuth contributions are the lowest among the six analytes, with a median content of approximately 25 $mg\,g^{-1}$.

For the present study, SE quadrant waste exemplars enriched in each of the solid phase analytes shown in Figure 2 can be proposed by selectively combining the core segments listed in Table 1. This approach enables the formation of up to six distinct SE quadrant waste solid sub-chemistries: aluminum, bismuth, natrophosphate, uranium, iron, and zirconium.

To achieve this goal, the individual chemistries of the 23 available core segments must first be considered, followed by the exclusive selection of specific jars to combine into groups that yield dominant enrichment of the targeted analytes. Figure 3 provides an overall unsorted view of the concentrations of each analyte of interest in the core segments listed in Table 1. This view reveals that many core segments exhibit chemistries largely dominated by a single analyte of interest.

Examples of core segments dominated by specific analytes include:

- **Aluminum**: AN-101 Segment 18 and AN-106 Segments 14 through 16.
- **Phosphate**: AN-106 Segments 16 through 20.
- **Zirconium**: AW-105 core segments.

Uranium chemistry is prominent in several core segments, specifically AN-101 Segments 12 and 13. However, these segments also contain appreciable amounts of aluminum and phosphate, resulting in mixed analyte enrichment. For iron, a single dominant segment (AN-106-22UH) exists, though this core also contains nearly equal amounts of aluminum. Similarly, other iron-rich segments (e.g., AN-106 Segment 18UH) are also heavily influenced by aluminum. Finally, all segments that exhibit appreciable bismuth chemistry are dominated by phosphate, making it difficult to isolate bismuth-enriched sub-chemistries from SE quadrant wastes.

Using the chemical compositions presented in Figure 3, waste composites can be derived in which the undissolved solids are selectively enriched in bismuth, natrophosphate, uranium, aluminum, iron, or zirconium. The exclusive sample selections corresponding to these sub-chemistries are detailed in Table 2, with the chemical compositions of the associated jars provided in Table 3. For AW-105, a single composition is presented due to the unavailability of per-jar chemical information in the Hanford literature accessible to the authors at the time of this report.

The estimated chemistries presented in Table 3 highlight some challenges and issues with the compositing strategy selected herein. First, while some samples show clear enrichment in a single analyte (e.g., Al dominates the chemistry of Al-rich composite samples), many show enrichment in one or more target components, and some target composite chemistries are have equal or more dominant amounts of other analytes. Examples of the latter include the Bi-composite, which is composed of samples that contain relatively large quantities of Bi (when compared to other samples) but whose chemistry is dominated by PO_4. Similarly, the U-composite chemistry is U-dominated but also contains appreciate quantities of Al and PO_4 solids. Overall, the selected compositing plan listed in Table 2 represents a balance between the chemistry of available samples and an attempt to isolate target chemistries. It should be noted that Jar 20360 (AN-106-19LH) was inadvertently binner as a U-rich sample due to incomplete or inaccurate preliminary assessments of its U content; this sample would have been better suited as a PO_4 rich solid. The overall impact of its inadvertent inclusion in the U-composite is minimal due to the samples limited solids inventory of $\sim$11 g, relative to a total inventory of $\sim$185 g.

From the selected samples, representative solid phase analyte compositions were established by averaging the centrifuged solids contents of each sample selection set. Similarly, representative liquid phase (supernatant) ion compositions were derived by averaging the per-jar centrifuged liquid contents. The results of these solid and liquid averaging activities are shown in Tables 5 and 4, respectively. The solid phase analytes in Table 5 correspond to the analytes of interest, while the liquid phase analytes in Table 4 are limited to the following key species: $Al(OH)_4^-$, Cl^-, F^-, OH^-, NO_3^-, NO_2^-, PO_4^{3-}, Na^+, SO_4^{2-}, and CO_3^{2-}.

For liquid-phase chemistries, translation of the as-characterized liquid waste components into bench-scale simulated liquid compositions followed established protocols, as outlined in Russell et al. (2009) and Peterson et al. (2017). This methodology has been successfully implemented in PNNL-led studies, including Russell et al. (2017), Daniel et al. (2022), and Schonewill et al. (2024). The resulting compositions focus on major analytes to simplify the chemistry of simulated supernatant derived from these averaged liquid-phase chemistries.

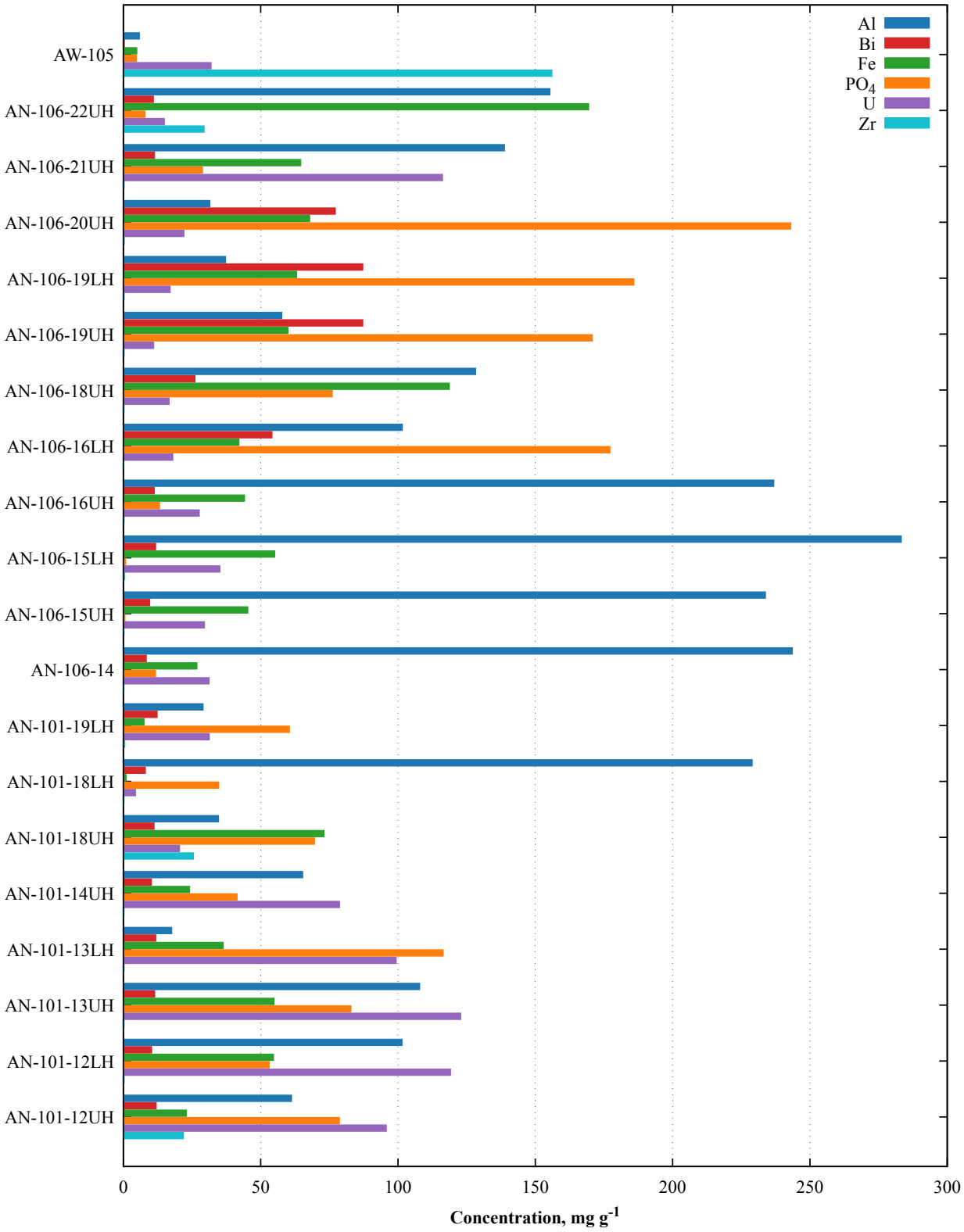


Figure 3. Per-core centrifuged solids concentrations for six selected analytes of interest. The core segments (y-axis labels) are described in Table 1. Concentrations are reported in milligrams of analyte per gram of centrifuged solid (dry basis).

Table 2. Association of samples used to derive exemplar SE quadrant wastes with solids rich in natrophosphate (PO_4), uranium, aluminum, iron, zirconium, or bismuth. Jar IDs are defined in Table 1. The solids mass column provides an estimated mass of the combined jars (on a wet sludge basis).

Solid Chemistry	Jar IDs for Associated Samples	Solids Mass, g
Al-rich	21415, 20913, 20918, 21006, and 21315	251.15
Bi-rich	21361 and 21362	38.42
Fe-rich	21416, 21357, and 21367	179.04
PO_4-rich	21378, 21417, and 21314	153.80
U-rich	21403, 21402, 21404, 21407, 21360, and 21366	185.88
Zr-rich	19257, 20326, 19262, 20507-1, and 20507-2	115.59

Table 3. Individual solids chemistries of associated SE quadrant exemplars. Jar IDs are defined in Table 1. All solids contents are provided in terms of milligram analyte per gram centrifuged solid (mg g^{-1}). Here, the analyte content is expected to primarily include contributions from the solid phase; however, Al and PO_4 likely include contributions from the interstitial liquid as well. For AW-105, a single composition is presented due to the unavailability of per-jar chemical information in the Hanford literature accessible to the authors at the time of this report

Jar ID	Description	Insoluble Solids Concentration, mg g^{-1}					
		Al	Bi	Fe	PO_4	U	Zr
Al-rich Composite							
21415	AN-101-18LH	229	7.93	0.988	34.7	4.34	0.166
20913	AN-106-14	244	8.27	26.7	11.7	31.2	0.165
20918	AN-106-15UH	234	9.53	45.3	0.507	29.5	0.194
21006	AN-106-15LH	283	11.7	55.1	0.726	35.1	0.440
21315	AN-106-16UH	237	11.2	44.0	13.1	27.6	0.200
Bi-rich Composite							
21361	AN-106-19UH	57.6	87.1	59.9	171	11.0	0.230
21362	AN-106-20UH	31.4	77.1	67.8	243	22.0	0.285
Fe-rich Composite							
21416	AN-101-18UH	34.6	11.1	73.0	69.5	20.4	25.4
21357	AN-106-18UH	128	26.0	119	76.0	16.6	0.200
21367	AN-106-22UH	155	10.9	169	7.83	14.9	29.3
PO_4-rich Composite							
21378	AN-101-13LH	17.5	11.7	36.3	116	99.3	0.221
21417	AN-101-19LH	29.0	12.2	7.48	60.4	31.2	0.454
21314	AN-106-16LH	102	54.0	42.0	177	17.9	0.109
U-rich Composite							
21403	AN-101-12UH	61.2	11.9	22.9	78.6	95.7	21.8
21402	AN-101-12LH	101	10.2	54.6	53.0	119	0.235
21404	AN-101-13UH	108	11.3	54.8	82.8	123	0.209
21407	AN-101-14UH	65.2	10.2	24.1	41.4	78.6	0.197
21360	AN-106-19LH	37.2	87.1	63.0	186	17.0	0.248
21366	AN-106-21UH	139	11.3	64.5	28.7	116	0.237
Zr-rich Composite							
19257 20326 19262 20507-1 20507-2	AW-105	5.78	0.302	4.83	4.65	31.9	156

Table 4. Simplified supernatant compositions for six SE quadrant waste sub-chemistries, derived from the sample combinations listed in Table 2 and core segment chemistries as reported in Jordan (2022a,b) and Disselkamp (2009). All liquid analyte concentrations are in M.

Analyte	Supernatant Concentration, M, for Composite					
	Al	**Bi**	**Fe**	**PO_4**	**U**	**Zr**
$Al(OH)_4$	0.232	0.009 03	0.279	0.215	0.0837	0.006 31
Cl	0.0563	0.0154	0.112	0.0955	0.0589	0.007 41
F	0.112	0.0315	0.0504	0.124	0.121	0.171
OH	1.25	0.0516	1.04	0.956	0.504	0.254
NO_3	0.881	0.262	1.63	1.48	0.956	0.394
NO_2	1.11	0.808	1.64	1.48	1.15	0.0595
PO_4	0.0241	0.159	0.0357	0.0205	0.0364	0.003 86
Na	4.88	3.09	6.49	5.76	4.56	1.13
SO_4	0.0431	0.0479	0.0380	0.0464	0.0366	0.004 55
CO_3	0.543	0.669	0.780	0.622	0.750	0.11

Table 5. Estimated solid compositions for the six SE quadrant waste sub-chemistries, derived from the sample combinations listed in Table 2 and core segment chemistries as reported in Jordan (2022a,b) and Disselkamp (2009). The per-composite concentrations were estimated by weight averaging the known analyte contents of the individual sample jars that comprise the composite using their expected jar masses. All solid analyte concentrations are in mg g^{-1} (dry solids basis).

Analyte	Solids Concentration, mg g^{-1}, for Composite					
	Al	**Bi**	**Fe**	**PO_4**	**U**	**Zr**
Al	242	47.9	85.7	49.4	98.5	5.78
Bi	9.32	83.4	14.6	26.1	14.6	0.302
Cr	0.794	0.745	2.58	2.13	0.546	1.87
Fe	31.0	62.8	107	28.9	51.9	4.83
PO_4	13.4	197	56.4	119	67.4	4.65
P	6.54	74.8	9.61	47.9	22.4	1.52
Na	95.9	248	174	259	149	217
U	25.3	15.1	18.2	50.1	111	31.9
Zr	0.206	0.251	20.3	0.259	1.45	156

Table 6 lists the estimated properties of the six SE quadrant sub-chemistries. These property estimates are derived using equivalent salt-based recipes, where individual ions are replaced by their associated salts (e.g., $NaNO_3$ for NO_3^-), leveraging density and viscosity models from Laliberté and Cooper (2004), Laliberté (2007a,b, 2009), and refinements made by Reynolds and Carter (2007, 2008b,a), as well as Reynolds et al. (2018, 2019).

It is important to note that the compositions presented in Tables 4 and 5 represent estimated contents based on previously characterized core segment chemistry and expected core masses provided by Laboratory 222-S to PNNL prior to the receipt of the 23 samples. For the present study, these estimates were instrumental in the planning and preparation of representative supernatant solutions used to "re-slurry" the dried waste solids into the derived composites.

Table 6. Simplified supernatant properties for the six SE quadrant sub-chemistries, estimated using the density and viscosity models of Laliberté and Cooper (2004) and Laliberté (2007a,b, 2009). Estimates are based on equivalent salt-based chemistries derived from the compositions listed in Table 4 and assume a temperature of 20 °C.

Composite	Density, kg m^{-3}	Viscosity, mPa s	Dissolved Solids, %
Al	1216	3.04	25.0
Bi	1148	2.09	16.3
Fe	1288	4.53	33.3
PO_4	1256	3.52	30.2
U	1206	2.71	24.0
Zr	1053	1.20	6.55

The data presented in this section provided the basis for combining samples to form selected SE quadrant waste composites enriched in one (or more) of the targeted analytes: aluminum (Al), bismuth (Bi), iron (Fe), PO_4, uranium (U), and zirconium (Zr). Comparison of the proposed composite chemistries in Table 5 with the distributions shown in Figure 2 indicates that the compositions of these composites are at or near the upper bounds of the distributions for their respective analytes. For example, the proposed Al-rich composite would have an aluminum content of 242 mg g^{-1}. This composite's aluminum content falls at the higher end of the distribution observed across the 23 SE quadrant samples, which is characterized by a median aluminum content of 120 and a maximum aluminum content of 283 mg g^{-1}.

As will be discussed in the next section, only five of the six proposed composites were prepared, utilizing 21 of the 23 sample jars received. These prepared composites include the Al-, Fe-, PO_4-, U-, and Zr-rich variants. The bismuth composite was not prepared due to the limited quantity of solids available.

4.0 Waste Receipt and Compositing

The previous section outlined a compositing strategy for preparing six SE quadrant waste exemplars to support the assessment of transport properties for Hanford SE quadrant wastes. Specifically, the strategy focused on creating exemplars enriched in Al-, Bi-, Fe-, natrophosphate (PO_4-), U-, and Zr-bearing solids using twenty-three existing waste samples from tanks AN-101, AN-106, and AW-105. Of the six potential exemplars, sufficient inventory was available for all except the Bi composite, allowing for the characterization of transport properties of interest (including just-suspended mixing speed [NJS], settling rate, and rheology, as described in Section 5). This section discusses the compositing methods implemented in preparing these five composites. It addresses the physical state of the twenty-three received samples (including select sample images captured during preliminary visual inspections), outlines the procedures used to recover dried solids from their parent jars into larger composites, and details the methods used to re-slurry the dried solids back to an initial undissolved solids content of 20 % by mass for initial testing.

4.1 Sample Receipt

The twenty-three waste jar samples itemized in Table 1 and selected for this study were sourced from the 222-S Laboratory, operated by HLMI. These samples were obtained by PNNL for use in the current study, with support from H2C staff. The samples were packaged by HLMI staff and shipped to PNNL's Radiochemical Processing Laboratory (RPL) under contract with Hanford Mission Integration Solutions. The shipment arrived in two separate deliveries in July 2024. Upon receipt, the samples were transferred to the RPL's SAL, where all compositing activities and the main series of transport testing were conducted.

4.2 Initial Inspection

The initial inspection of the 23 samples involved measuring the gross mass of the sample jars and performing visual imaging of both the exterior surfaces of the sample jars and the solids contained within. Visual imaging was conducted to document the initial state of the samples and to confirm the integrity of the containers. A total of 24 sample jars were received, with Sample 20507 being split across two separate jars to address potential shipping concerns related to material accountability. A complete itemization of the initial inspection, including exterior and interior images for all sample jars, is provided in Appendix A.

With few exceptions, the sample solids were typically well-dried and presented as either loose granular or powdery solids, or as solid chunks/blocks of aggregated material. Representative examples of dry solids from tanks AN-101, AN-106, and AW-105 are shown in Figures 4 through 6.

Some sample jars, however, contained solids with inherent moisture. These samples varied between slightly humid solids and paste-like materials, consistent with the form expected for settled sludges. Samples exhibiting this wet behavior include:

- Jar 21378 (AN-101 Segment 13 LH),
- Jar 21404 (AN-101 Segment 13 UH),
- Jar 21417 (AN-101 Segment 19 LH), and
- Jar 20326 (AW-105 Segment 8 LH).

Examples of these wet or pasty sludges are provided in Figures 7 through 9.



Figure 4. Image of solids within Jar 21415 (AN-101 Segment 18 LH). The solids appear dry powder with intermediate-sized aggregates.



Figure 5. Image of solids within Jar 21006 (AN-106 Segment 15 LH). The solids include large aggregates with limited powder.



Figure 6. Image of solids within Jar 20507 (AW-105 Segment 8R2). The solids appear as large aggregates.

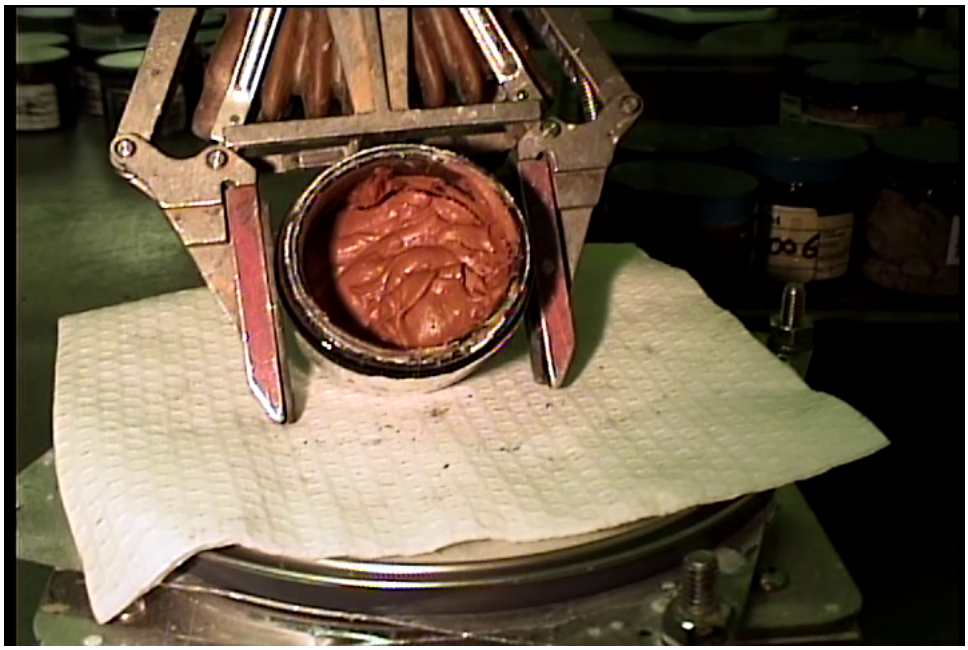


Figure 7. Image of solids within Jar 21378 (AN-101 Segment 13 LH). The solids exhibit a sticky paste-like consistency with inherent moisture.

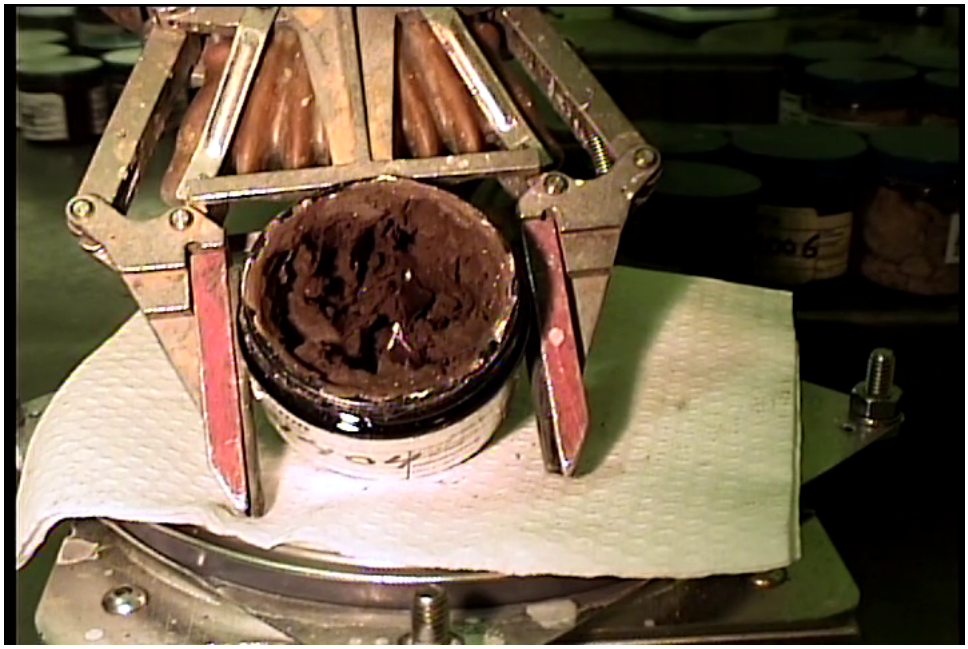


Figure 8. Image of solids within Jar 21404 (AN-101 Segment 13 UH). The solids exhibited a dense paste-like consistency with limited inherent moisture.

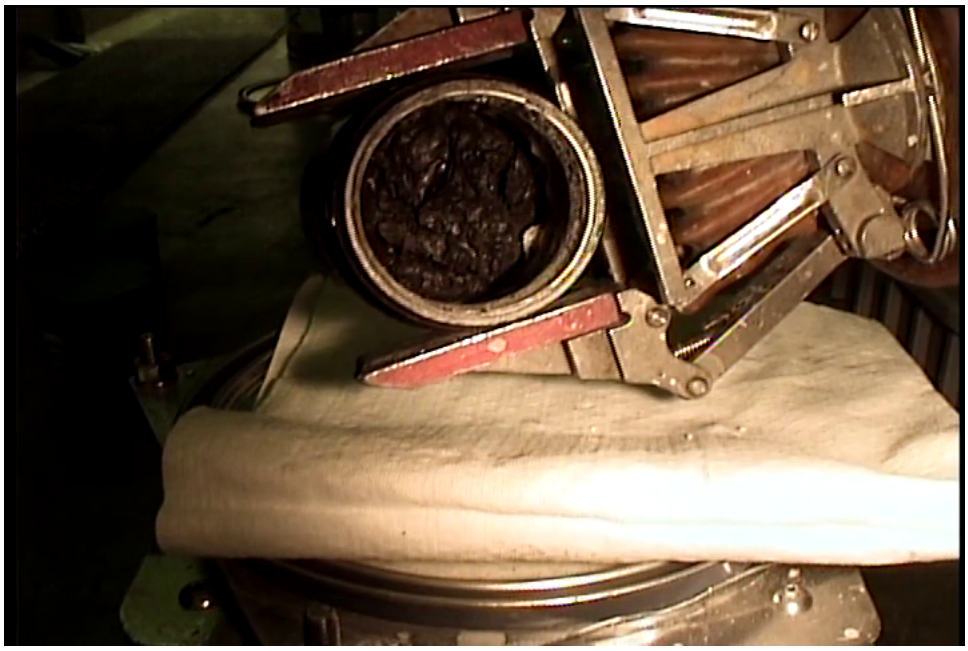


Figure 9. Image of solids within Jar 20326 (AW-105 Segment 8 LH). The solids exhibited a dense paste-like consistency with limited inherent moisture.

4.3 Compositing Activities

As introduced earlier in this section, five composites based on Al, Fe, natrophosphate, U, and Zr sub-chemistries were targeted using all but two of the twenty-four core samples (from AN-101, AN-106, and AW-105) received for the present study. Compositing activities focused on recovering solids from the jars associated with each sub-chemistry (as listed in Table 2) into 1 L high-density polyethylene (HDPE) bottles. The recovered solids were subsequently slurried with simulated supernatant representative of the sub-chemistry's centrifuged liquid composition.

Liquid Simulant Preparation: The liquid-phase chemistries and properties associated with the five sub-chemistries were previously presented in Tables 4 and 6. The detailed recipes used to prepare each of the liquid-phase simulants are outlined in Table 7. The required chemicals for the preparation of the supernatant were sourced as follows:

- Aluminum nitrate nonahydrate [$Al(NO_3)_3 \cdot 9\,H_2O$] from Sigma-Aldrich (>98 %)
- Sodium hydroxide (NaOH, 50 % w/w in water) from Acros Organics (extra pure)
- Sodium phosphate dodecahydrate ($Na_3PO_4 \cdot 12\,H_2O$) from Sigma-Aldrich (ACS Reagent, >98 %)
- Sodium chloride (NaCl) from Alfa Aesar (>99 %)
- Sodium fluoride (NaF) from Sigma-Aldrich (ACS Reagent, >99 %)
- Sodium sulfate (Na_2SO_4) from Fischer Chemicals
- Sodium nitrite ($NaNO_2$, 98.3 %) from JT Baker
- Sodium nitrate ($NaNO_3$, >99 %) from Acros Organics
- Sodium carbonate monohydrate ($Na_2CO_3 \cdot H_2O$) from Sigma-Aldrich (ACS Reagent, >99.5 %)

All simulant preparations utilized deionized (DI) water with a resistivity of 18 MΩ cm or greater. Preparations were conducted in 2 L glass Erlenmeyer flasks by first adding approximately 90 % of the DI water to the flask, with the remaining 10 % reserved for rinsing vessels and weigh boats used during chemical transfers. Individual components, aside from water, were added in the order listed in Table 7. Precision during preparation was maintained at ± 1 % for simulant components weighing >0.1 g and ± 5 % for components weighing <0.1 g.

The 50 % NaOH solution was transferred into a tared beaker before being added to the simulant flask. To ensure complete transfer, the beaker was rinsed with the reserved DI water at least three times. Once all chemicals were transferred, the remaining DI water was added to the flask, and the solution was heated to approximately 65 °C while stirring until complete dissolution of the solids was achieved. Following dissolution, the solution was maintained at elevated temperature with continued stirring for an additional 30 to 60 minutes, after which it was allowed to cool to ambient temperature (20-22 °C) overnight.

Table 8 lists the measured compositions of the five as-made waste supernatants. Table 9 summarizes the physical properties of the as-made liquid simulants, including density, viscosity, and dissolved solids content. The methods used to characterize the chemical and physical properties of the liquid simulants are detailed in Section 5. Generally, deviations between as-made and targeted analyte contents fall within the expected error thresholds for the analytical methods utilized, which is approximately ± 15 %. Physical property measurements demonstrate good agreement with composite-based estimates, with density deviating by no more than 0.5 %, dissolved solids content by no more than 1 %, and viscosity by no more than 20 %.

Table 7. Chemical recipes used to prepare simulated supernatants for the five composite sub-chemistries tested. All recipes assume that NaOH is added as a 50 % (by mass) solution in water. Apart from water, all components are listed in the expected order of addition. As-prepared recipes nominally yield the molar analyte contents listed in Table 4. All mass concentrations are in $g\,L^{-1}$.

Compound	Mass Concentration, $g\,L^{-1}$, for Composite				
	Al	**Fe**	**PO_4**	**U**	**Zr**
$Al(NO_3)_3 \cdot 9\,H_2O$	87.08	104.6	80.56	31.38	2.37
NaOH (50 % w/w)	174.4	172.5	145.2	67.11	22.31
$Na_3PO_4 \cdot 12\,H_2O$	9.17	13.58	7.81	13.83	1.47
NaCl	3.29	6.55	5.58	3.44	0.433
NaF	4.69	2.11	5.21	5.06	7.18
Na_2SO_4	6.13	5.40	6.59	5.20	0.646
$NaNO_2$	76.31	112.9	102.4	79.41	4.11
$NaNO_3$	15.70	67.11	71.23	59.91	31.85
$Na_2CO_3 \cdot H_2O$	67.32	96.74	77.10	93.03	13.59
H_2O	771.7	706.0	753.9	847.9	969.5
Total	1215.8	1287.6	1255.7	1206.3	1053.4

Table 8. Measured composition of the as-prepared simulated supernatant. All liquid analyte concentrations are in M. Supernatant carbonate contents were not measured.

Analyte	Measured Supernatant Concentration, M, for Composite				
	Al	**Fe**	**PO_4**	**U**	**Zr**
$Al(OH)_4$	0.290	0.220	0.0846	0.246	0.007 04
Cl	0.11	0.0883	0.0591	0.0555	0.008 15
F	0.0427	0.112	0.113	0.103	0.168
OH	1.56	1.14	0.493	1.20	0.179
NO_3	1.66	1.46	0.970	0.883	0.389
NO_2	1.74	1.52	1.25	1.18	0.0617
PO_4	0.0244	0.0196	0.0284	0.0221	0.009 12
Na	6.50	5.72	4.48	5.03	1.17
SO_4	0.0380	0.0448	0.0372	0.0425	0.006 12

Table 9. Measured properties for the as-made simulated supernatant liquids. Measurements were performed at 20 °C.

Composite	Density, $kg\,m^{-3}$	Viscosity, mPa s	Dissolved Solids, %
Al	1215	3.57	24.8
Fe	1282	5.09	32.9
PO_4	1253	4.22	29.8
U	1201	2.76	24.0
Zr	1055	1.48	6.60

Composite Preparation: The goal of composite preparation was to generate slurries targeting the Al, Fe, PO_4, U, and Zr sub-chemistries at an initial undissolved solids (UDS) content of 20 % by mass. Serial dilution of these 20 % composites with representative supernatant would then allow physical, chemical, and transport properties to be assessed as a function of UDS content. Composite preparation was performed in three stages:

1. Recovery of solids from their parent jars.
2. Dilution of the recovered composites with simulated supernatant to a targeted UDS of 25 % by mass (Stage 1 dilution).
3. Final adjustment of the composite dissolved solids (DS) and UDS, with the latter adjusted to 20 % by mass (Stage 2 dilution).

This staged approach was selected due to uncertainties in the as-received mass/moisture content of the composites and its flexibility in correcting deviations in DS and UDS from their anticipated targets. Simulated supernatant was used, rather than DI water, to re-slurry the solids to avoid dissolving solids nominally stable in the high-salt waste liquid matrix (such as precipitated salts). An initial (Stage 1) compositing solids content of 25 % was chosen to avoid over-diluting the solids beyond the targeted characterization level of 20 %. More broadly, a higher-end solids content of 20 % was selected because it represents the upper limit of anticipated DFHLW solids loadings.

The first step in compositing involved recovering solids from the jars received from Laboratory 222-S and transferring them into 1 L Nalgene HDPE bottles. Jar selections for each composite sub-chemistry are itemized in Table 2. The specific recovery approach varied based on the dryness and consolidation of the samples (e.g., the hardness of large aggregates like those shown in Figure 6).

Solids recovery was conducted as follows:

1. The source jar was opened, and large clumps of solids were broken into smaller pieces using a spoon or laboratory spatula where feasible.
2. Solids were gently poured or scraped from the parent jar into the composite bottle to the best extent practicable. Excess solids adhering to the spoon/spatula were scraped off against the edge of the composite bottle opening.
3. Residual solids adhering to the walls of the parent jar were rinsed into the composite bottle using the appropriate composite supernatant.

If the sample clumps were too hard to break with the spoon or spatula during Step 1, the solids were transferred into a plastic bag and sealed. The sealed bag was gently crushed using a heavy object (such as a balance check weight) before transferring the powdered material into the corresponding HDPE composite bottle. Any residual solids adhered to the tools or bag used during the crushing and transfer process were rinsed into the composite bottle using the appropriate composite supernatant.

Table 10 lists the mass of solids recovered from the parent jars for each of the five composites. Except for the Zr composite, the actual mass of solids recovered from the jars was approximately 80 % of the expected mass based on inventories provided by Laboratory 222-S. This lower-than-expected recovery was anticipated due to sample moisture loss during extended storage at 222-S, as well as minor losses resulting from holdup on jars and tools during the recovery process. It should be noted that recovery values were determined by measuring the difference in the gross mass of the parent jars before and after solids recovery. Recovered masses were documented after completion of compositing activities and were not used to inform the subsequent dilution process described below. Instead, direct measurements of DS and UDS contents were employed following preliminary (Stage 1) resuspension using simulated supernatant.

After recovery of solids, sufficient simulated supernatant was added to each composite to target a slurry UDS content of 25 % (w/w). Dilutions were based on estimated moisture content of the composited solids and utilized the expected mass of recovered solids listed in Table 10 as a basis for determining the required quantity of supernatant needed to achieve 25 % UDS. The estimated moisture content of the composited solids and the supernatant dilution schedule for each composite are provided in Table 11. All planned dilutions made use of the simulated supernatant specific to each composite, as detailed in Tables 4 and 6.

Efforts to maximize solids recovery from the parent jars included the rinsing of residual solids with simulated supernatant. The mass of supernatant used for rinsing jars and tools was carefully tracked to ensure that the total mass of supernatant used for both rinsing and dilution did not exceed the mass listed in Table 11.

Table 10. Mass of solids recovered for each composite sub-chemistry. The original expected mass of solids, based on 222-S inventory numbers provided prior to sample receipt (and listed in Table 2), is included for reference. The percent realized represents the percent of the expected mass actually recovered (e.g., for the Al composite, 82 % of the expected mass was recovered). Differences between the actual and expected masses were anticipated and likely derive from a combination of minor losses during sampling and sample moisture loss during storage prior to receipt.

Composite	Expected Mass Recovered, g	Actual Mass Recovered, g	Percent Mass Realized, %
Al	251.15	206.07	82
Fe	179.04	134.53	75
PO_4	153.80	122.89	80
U	185.88	138.98	75
Zr	204.22	195.65	96

Table 11. Composite dilution schedule for a target UDS of 25 %. The expected moisture contents are derived from the core segment data in Jordan (2022a,b). A reliable moisture content for the Zr sludge samples was not available at the time composite dilutions were planned; a conservative value of 50 % by mass was assumed to avoid over-dilution. The mass of total (dried) solids is assumed to include soluble salts that were part of the original supernatant. The mass of supernatant to add represents the quantity of simulated supernatant required for each sub-chemistry to dilute the insoluble solid content of the dried solids to 25 %. Simulated composite supernatant properties are listed in Tables 4 and 6.

Composite	Expected Sludge Moisture Content, %	Expected Mass Total Solids, g	Target Mass of Supernatant to Add, g
Al	29.9	176.05	352.78
Fe	35.3	115.82	158.20
PO_4	40.1	92.10	108.03
U	33.5	123.61	229.78
Zr	50.0	102.11	175.61

Following Stage 1 dilution to 25 %, samples of the fully suspended composite and composite supernatant (after allowing the suspended solids to settle for 24 h) were collected. The samples were placed into pre-weighed vials and dried over a 120 h period. Prior to sampling the composite slurry, vigorous mixing was performed by tumbling the composite from side-to-side. To sample the composite supernatant, the composite was allowed to settle for 24 h, and the clarified liquid was drawn from the top of the composite.

The net mass of the samples before and after drying was used to estimate the DS and total solids (TS) contents of the supernatant and slurry, respectively. Here, the TS content represents the mass of both insoluble and soluble solids per gram of slurry, while the DS content corresponds to the mass of soluble solids per gram of supernatant. Both measures of solids content are expressed as weight fractions.

The UDS content of the composite was calculated using the following equation:

$$\text{UDS} = \frac{\text{TS} - \text{DS}}{1 - \text{DS}}, \tag{2}$$

where the UDS represents the mass of insoluble (undissolved) solids per unit mass of composite. Table 12 lists the measured UDS and DS contents for each composite. These contents provided the basis for final adjustments to the composite UDS and DS concentrations, targeting a final UDS of 20 % by mass and a final DS concentration corresponding to the dissolved solids content listed in Table 6.

Table 12. As-measured Stage 1 dilution composite UDS and DS contents. Stage 1 targeted a global UDS content of 25 % and a DS that matches the as-made DS for the simulated supernatant for each composite, as listed in Table 9. The intent of Stage 1 dilution was to avoid gross over-dilution of the composites due to soluble solid dissolution.

Composite	As-Made		Target	
	UDS, %	DS, %	UDS, %	DS, %
Al	23.0	29.5	25.0	24.8
Fe	17.7	38.9	25.0	32.9
PO_4	16.8	34.7	25.0	29.8
U	26.7	29.1	25.0	24.0
Zr	26.6	22.4	25.0	6.60

It was anticipated that the as-prepared Stage 1 composites would exhibit UDS concentrations close to 25 % and DS contents exceeding their as-prepared simulant targets. The UDS expectation was based on assumed parent sample masses and moisture contents discussed previously, while the DS expectation was derived from the assumption that some proportion of soluble solids in the dried as-received parent jar solids would dissolve upon dilution with supernatant.

For measured Stage 1 solids contents, the expectation that DS would exceed the as-made supernatant DS was confirmed in all cases. This indicates that some portion of the initial composite solids dissolved into the supernatant, raising the DS content. In general, the absolute difference between the measured Stage 1 DS and the diluent DS was approximately 5 %, except for the Zr composite, which exhibited an exceptionally high DS of 22.4 % compared to its expected value of 6.55 %.

Measured Stage 1 UDS contents showed mixed results. Some composites (Al, U, and Zr) exhibited UDS contents near the target of 25 %, while others (Fe and PO_4) fell considerably below the target, at 17.7 % and 16.8 %, respectively.

Interpreting discrepancies between target and measured UDS and DS values is challenging due to the unknown moisture content of the initial pre-dilution solids, the lower-than-expected inventory of solids, and the presence of soluble solids in the as-received composite solids. The unexpectedly high DS for the Zr composite suggests that a significant portion of the Zr composite solids dissolved into the supernatant. This suggests that the assumed 50 % moisture content used during planning was overly conservative, or more specifically, that much of the mass of AW-105 solids recovered from the jars (96 % of the expected inventory by mass) were soluble salts rather than moisture. Similar discrepancies likely contributed to deviations observed for the Fe and PO_4 composites, as listed in Table 12.

The Stage 1 solid content measurements provided a basis for “zeroing in” on the target characterization UDS of 20 % and correcting the supernatant DS to match target contents. Stage 2 dilution efforts aimed first to correct supernatant DS, either by evaporation to increase DS or by dilution with DI water to reduce DS. Since all Stage 1 DS measurements were higher than expected, Stage 2 corrections involved exclusively dilution with DI water.

The water dilution level DL_w, defined as the mass of water necessary to dilute the supernatant to a target

DS of DS_{target} per mass of Stage 1 composite, was calculated using the following equation:

$$DL_w = \left(\frac{DS_1}{DS_{target}} - 1 \right) (1 - UDS_1) \quad (3)$$

In this equation, the subscript "1" refers to the Stage 1 dilution contents provided in Table 12. If DL_w is negative (not applicable to the current composites), it represents the amount of solvent that would need to be removed by evaporation to meet the target DS.

After correcting the supernatant DS, Stage 2 adjustments targeted a composite UDS content of 20 %. This adjustment was achieved either by adding supernatant to reduce UDS or by performing settle-decant operations to increase UDS.

The supernatant dilution level DL_a, defined as the mass of supernatant that must be added to adjust the UDS from its Stage 1 content to a target UDS of UDS_{target} per mass of Stage 1 composite (prior to water dilution), was calculated as:

$$DL_a = \left(\frac{UDS_1}{UDS_{target}} \right) - DL_w \quad (4)$$

If DL_a is negative, it indicates that supernatant must be removed to meet the target UDS.

Table 13 tabulates the mass of the as-prepared Stage 1 composite, along with the estimated dilution levels and masses required to adjust the composites to a final UDS of 20 % and their respective simulated supernatant DS contents. It is important to note that, apart from the net mass of the Stage 1 composite, the listed masses represent proposed adjustments to the final composites. While targeted adjustments were followed to the precision allowable in remote radiological environments for the Al, Fe, and U composites, adjustments for the PO_4 and Zr composites deviated from Table 13.

For the Zr composite, the measured DS content of the Stage 1 composite (22.4 %) significantly exceeded the anticipated value (6.60 %). This discrepancy necessitated substantial water dilution, with a calculated DL_w of 1.75 for Zr compared to ∼0.15 for all other composites. In absolute terms, achieving the target DS for the Zr composite would require the addition of approximately 600 g of water to the ∼340 g Stage 1 composite and subsequent removal of roughly 480 g of composite supernatant. This adjustment would necessitate transitioning to a larger composite bottle (1.5-2 L) and handling larger quantities of composite, increasing the risk of solids loss during transfer and producing additional liquid waste. To avoid these difficulties, dilution of the Zr composite with water was forgone. Instead, adjustment of the Zr composite involved the addition of ∼110 g of supernatant with a DS content of 6.60 % to reduce the UDS to 20 %.

Similarly, adjustments to the PO_4 composite deviated due to a lower-than-expected recovered solids inventory (122.86 g) and a measured Stage 1 UDS of 16.8 %. Stage 2 adjustments would have reduced the composite mass from 204.23 g to 171.37 g. Planned sampling for archival and chemical characterization would have further reduced the composite mass to less than 150 g, posing significant challenges to rheology and transport testing, which typically require a minimum of 200 g of test slurry. To avoid issues stemming from limited inventory, supernatant adjustments to increase the PO_4 composite UDS to 20 % were not performed. Although the final UDS of the Stage 2 PO_4 composite was only 14.6 %, forgoing the decant operation retained a final composite mass of ∼234 g. After taking archive and analytical samples, the remaining composite mass of ∼200 g was sufficient to perform full rheological and transport characterization, albeit at lower than expected UDS.

Table 14 summarizes the final adjustments made to the composites, along with the final measured mass, UDS, and DS contents for each composite. It is important to note that the final mass listed in Table 14 reflects the composite mass prior to removing samples for analytical and archival purposes.

Table 13. Stage 2 composite dilutions as originally planned. Here, Stage 2 targeted a global UDS content of 20 % and a DS that matches the as-made DS for the simulated supernatant for each composite, as listed in Table 9. The water and supernatant dilution levels (DL_w and DL_a, respectively), are calculated using Eqs. 3 and 4. Negative dilution levels require removal of water/supernatant. The actual dilutions implemented are outlined in Table 14.

Composite	Stage 1 Composite Mass, g	Water Dilution Level	Supernatant Dilution Level	Water To Add, g	Supernatant To Add, g	Estimated Final Composite Mass, g
Al	546.19	0.1479	0.0009	80.76	0.48	627.43
Fe	286.86	0.1490	−0.2617	42.75	−75.06	254.55
PO_4	204.23	0.1378	−0.2987	28.14	−61.01	171.37
U	349.48	0.1557	0.1781	54.43	62.25	466.16
Zr	335.44	1.7526	−1.4218	587.91	−476.93	446.41

Table 14. Final as-prepared "20 %" UDS composite masses and solid contents. The final preparations involve two key differences from those planned in Table 13: 1) the water dilution for the Zr composite was skipped due to the large dilution required and 2) the PO_4 composite supernatant decant operation was forgone to retain composite mass within the 200 g limit needed for physical property testing (albeit at a lower UDS content).

Composite	Water Added, g	Supernatant Adjustment, g	Final Composite Mass, g	UDS, %	DS, %
Al	80.73	0.55	627.47	20.0	24.8
Fe	42.79	−74.95	254.70	20.0	32.9
PO_4	30.07	– –	234.30	14.6	29.5
U	54.42	62.25	466.15	20.0	24.0
Zr	– –	108.59	444.03	20.1	17.5

Despite the notable deviations in compositing for the Zr and PO_4 composites, the preparation of the five composites largely followed expectations. All composites were adjusted to the targeted 20 % UDS content, with the exception of the PO_4 composite, where a reduced UDS was necessary to ensure sufficient inventory for planned transport tests. Following Stage 2 composite adjustments, approximately 15 g of each composite was archived to allow for additional chemical analysis on the "unhandled" composite in case of loss or anomalous results from the analytical samples. Additionally, three ∼5 mL samples of each composite were taken for chemical analyses. In total, final composite sampling removed between 35-50 g of slurry. The analytical methods utilized during these analyses are described in Section 5.

As the analytical results provide critical insight into the fidelity of the compositing strategy and the as-implemented compositing efforts, these results are discussed in detail below.

4.4 Compositing Results

Table 15 compares the estimated and actual (as measured) composite solid chemistries for the five prepared composites. As in prior sections, estimated compositions derive from Jordan (2022a,b) and Disselkamp (2009), whereas the actual compositions result from chemical analyses performed on the composites prepared herein. Both estimated and actual compositions are presented on a total, dry-solids basis, though some uncertainty remains due to sampling variability, particularly in the remote handling environment. In general, waste solids are dense and settle rapidly, complicating unbiased sampling due to the slow, deliberate aliquot transfer process required under radiological safety protocols.

The measured composites tend to exhibit higher total solid concentrations relative to their estimated counterparts, with sodium concentrations substantially exceeding expectations across all composites. The cause of this discrepancy is unclear but may reflect differences in the state of the solids characterized in

Table 15. Comparison of estimated and measured (actual) composite chemistry for the five prepared SE waste exemplars. All solid-phase analyte concentrations are in mg g^{-1} (dry solids basis).

Analyte	Solids Concentration, mg g^{-1}, for Composite				
	Al	**Fe**	**PO_4**	**U**	**Zr**
			Estimated		
Al	242	85.7	49.4	98.5	5.78
Cr	0.794	2.58	2.13	0.546	1.87
Fe	31.0	107	28.9	51.9	4.83
Na	13.4	56.4	119	67.4	4.65
PO_4	95.9	174	259	149	217
U	25.3	18.2	50.1	111	31.9
Zr	0.206	20.3	0.259	1.45	156
			Measured (Actual)		
Al	418	115	80.6	201	25.2
Cr	0.685	2.89	2.57	0.344	13.1
Fe	48.7	142	48.6	84.6	32.2
Na	142	232	305	214	358
PO_4	27.4	1.87	161	98.9	6.48
U	36.7	23.5	87.9	173	67.2
Zr	0.0634	18.3	0.0155	0.005 36	229

Jordan (2022a,b) and Disselkamp (2009) (core segment solids) versus the current study (a de-slurried 20 % slurry). Both analytical treatments, however, appear consistent in their methodology: chemical characterization was conducted on centrifuged solids (with supernatant decanted) subjected to acid digestion.

Neglecting sodium contributions, the composite chemistries are dominated by their targeted analytes, demonstrating that the composites successfully represent the desired sub-chemistries. For example, the Al composite shows the greatest contribution from Al, the Fe composite from Fe, and so on. The actual chemistries diverge from their estimated counterparts; however, these differences are often obscured by the magnitude of the analyte contributions. To normalize these variations, Table 15 compositions are reframed as weight fractions and presented in Figure 10.

Figure 10 compares expected "Exp." (estimated) and measured "Mea." (actual) compositions for each sub-chemistry as stacked bar plots. This visualization reveals notable disparities in sodium and phosphate content between estimated and measured compositions. Specifically, sodium content is significantly higher across all composites, while phosphate content is consistently lower than expected. Given the association of PO_4 with natrophosphate ($Na_7(PO_4)_2F \cdot 19\,H_2O$), the observed disparities in Na and PO_4 are reasonable. Natrophosphate's molecular formula implies a sodium-to-phosphate ratio of approximately 3.5. Analysis of sodium and PO_4 ratios in the measured composites indicates sodium exceeding this ratio across all samples. The degree of sodium excess varies by composite, ranging from a factor of two in the PO_4 composite to a factor of $\sim$150 in the Fe composite, which contains virtually none of the anticipated PO_4 inventory.

For other analytes of interest—namely Al, Fe, U, and Zr—the relative contributions align closely with expectations. Figure 11 provides a focused comparison of stacked bar compositions excluding sodium, phosphate, and minor analytes (e.g., Bi and Cr). This simplified visualization demonstrates that Al, Fe, PO_4, U, and Zr composites exhibit expected speciation consistent with their targeted sub-chemistries, within analytical error margins. The Zr composite exhibits minor deviations, with larger-than-anticipated Al and Fe contributions.

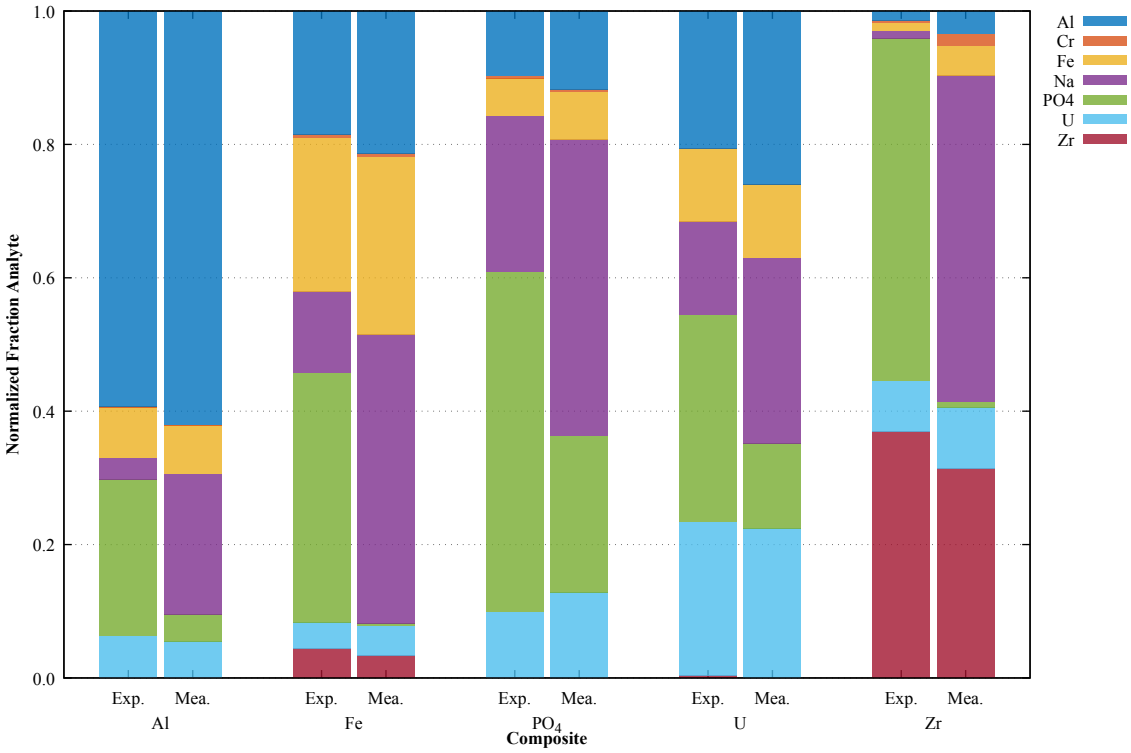


Figure 10. Comparison of estimated and actual (as measured) composite solid chemistries. The stacked bar elements represent the weight fractions of analytes shown. Estimated values are derived from analytical data presented in Jordan (2022a,b) and Disselkamp (2009), whereas measured (actual) values are based on chemical analysis of the as-made composites at 20 % UDS content.

After preparation, the five SE quadrant waste composites (Al, Fe, PO_4, U, and Zr) were subjected to a range of physical characterization and transport testing. Specific physical characterizations included measurements of supernatant density, estimation of bulk composite density, composite rheology (including shear strength, constitutive behavior, and viscosity), and evaluations of composite settling rate and just-suspended mixing speed (NJS). The primary NJS testing was conducted under a separate subtask within the current program and will be reported elsewhere. For completeness, the results from NJS testing will also be discussed and summarized in the present report.

The next chapter describes the materials and methods used to evaluate the physical and transport properties of the composites. Some results, primarily the UDS and DS contents of the composites and the measured properties of the as-prepared supernatants, have already been discussed in this section to provide context for composite preparation. The section that follows will detail the measurement basis for physical and transport property testing. As the next chapter focuses on materials and methods, the analytical methods underlying the chemical characterizations presented in this section will also be discussed.

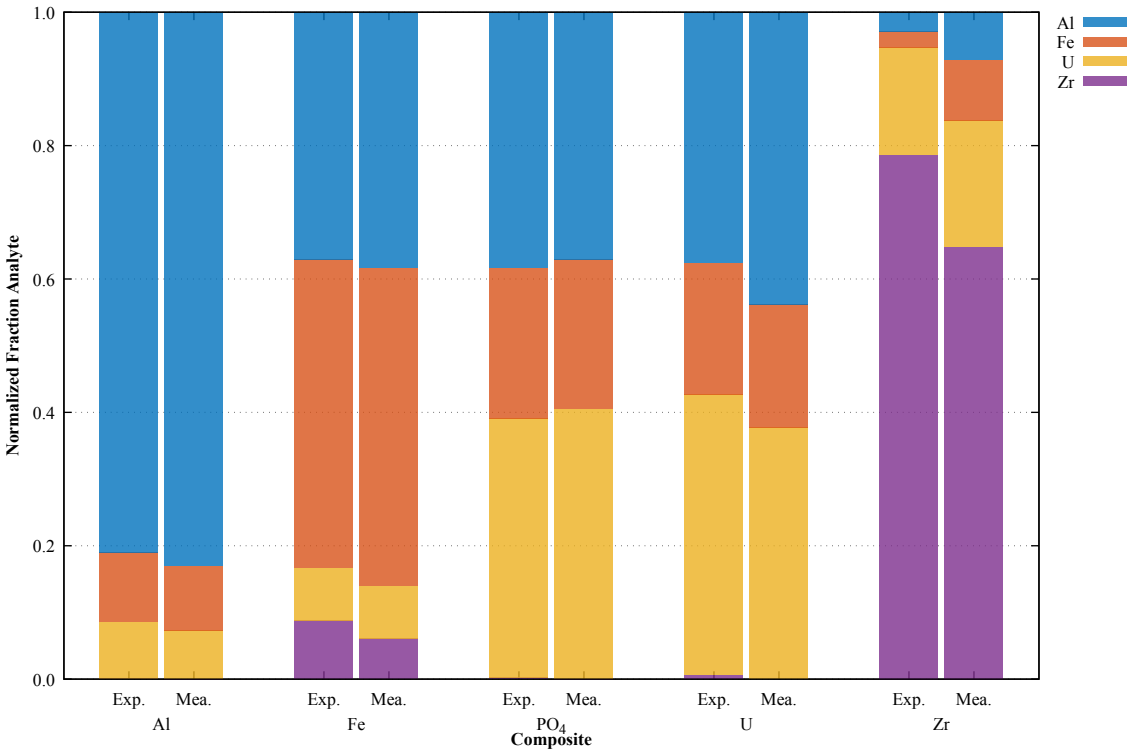


Figure 11. Comparison of estimated and actual composite solid chemistries for primary analytes, excluding PO_4. Here, minor (non-target) analytes and PO_4 have been removed to better illustrate differences among the core analytes of interest: Al, Fe, U, and Zr. As Figure 10 demonstrates reduced PO_4 compared to expectations, exclusion of PO_4 allows for clearer observation of differences between expected and actual contributions of Al, Fe, U, and Zr. The stacked bar elements represent the weight fractions of analytes shown. Estimated values are derived from analytical data presented in Jordan (2022a,b) and Disselkamp (2009), whereas measured (actual) values are based on chemical analysis of the as-made composites at 20 % UDS content.

5.0 Characterization Methods and Basis

The purpose of this study is to measure and interpret the chemistry, physical, and transport properties of Hanford SE quadrant waste slurries. For the present work, chemical properties evaluated include key analyte concentrations, anion contents, and free hydroxide levels within the waste. Physical properties assessed include particle size, settling rate, solids contents, densities, and rheology of the composite slurries and their simulated liquid suspending phases. The singular transport property considered is the NJS, which was measured in a companion report and whose results are reproduced herein. Table 16 itemizes the physical and chemical properties measured along with their scope.

In the subsections that follow, the methods used to characterize each of the chemical, physical, and transport properties outlined above are discussed briefly. In addition to slurry characterization methods, this section also describes procedures used for adjusting composite concentrations.

Table 16. Summary of physical and chemical characterization techniques used to assess transport and transport-relevant properties of the five Hanford SE waste composites.

Analysis	Methods	Samples
Composite Chemistry	Metals by ICP-OES Anions by IC Free OH by Tritation TIC/TOC	All 20 % composites Select fractions (solids, supernatant)
PSD	Microscopic Imaging via SEM/EDS	Dry AN-101, AN-106, and AW-105 solids Select as-received jars
Flow Behavior	Concentric Cylinder Rotational Viscometry	All composites Select solids spanning 5 to 20 % Simulated supernatants.
Shear Strength	Vane Viscometry	All 20 % composites Allowed to settle 165 h
Settling Rate	Volumetric Grade A Flask Direct Visual Observation	All 5 to 20 % composites Allowed to settle 24 h
NJS	Direct Visual Observation of Vessel Bottom Overhead Paddle Mixer Sentinel Particles (Fe composite)	All 20 % composites Allowed to settle 24 h

5.1 Composite Chemistry

The chemistry of the composites was characterized using a combination of inductively coupled plasma-optical emission spectroscopy (ICP-OES), ion chromatography (IC), titration, and total carbon/total organic carbon (TIC/TOC) analysis. For each of the composites prepared, three analytical samples were taken from as-prepared slurries with an approximate solids content of 20 % UDS. Additionally, one analytical sample of the non-radiological simulated supernatant used for composites re-slurrying was submitted for analysis.

Samples were processed by PNNL's Analytical Services Organization (ASO), which conducted ICP-OES and free hydroxide (OH^-) determinations and coordinated IC and TIC analyses through PNNL's Geosciences Laboratory. Table 17 lists the sequence of chemical characterizations applied to each of the four "per-composite" samples submitted to ASO for analysis.

Table 17. Analytical methods requested for composite and simulated supernatant samples.

Sample	Analysis Requested
Per-Composite Sample 1	IC of filtered supernatant: Cl, F, PO_4, NO_3, NO_2, and SO_4
Per-Composite Sample 2	ICP-OES for both supernatant and acid-digested solids: Al, Fe, U, Zr, P, Na, and Cr
Per-Composite Sample 3	Free Hydroxide, Total Inorganic Carbon (TIC), Total Organic Carbon (TOC) for filtered supernatant
Simulated Supernatant	IC of filtered supernatant: Cl, F, PO_4, NO_3, NO_2, and SO_4

5.2 Particle Size Distribution

For the present study, composite slurries were not directly sampled for particle size or particle size density distribution characterization. Instead, limited samples of dried, as-received waste solids were taken upon receipt of the 23 individual core samples utilized in this study. Table 18 lists the jars from which samples were collected for particle size analysis. Approximately 0.5 g or less was taken from each core segment listed for analysis.

The particle size of these samples was characterized using Automated Particle Analysis (APA) applied to Scanning Electron Microscopy (SEM) images coupled with X-Ray Energy Dispersive Spectroscopy (EDS). The integration of APA with SEM-EDS offers the capability to isolate individual particles and their corresponding chemistries. This allows assessments of the size distribution for particles associated with specific mineral phases, such as gibbsite. The APA analysis of the samples listed in Table 18 has been previously reported in Buck et al. (2025).

While the analyses presented in Buck et al. (2025) report size distributions on a number-basis (derived from microscopic image analysis), most historic size measurements for Hanford wastes have been conducted using laser diffraction instruments, as compiled in Wells et al. (2007, 2011). To ensure consistency with these historical measurements, the current report re-presents select particle size distribution (PSD) results from Buck et al. (2025) in a volume distribution format.

Given a number-based size distribution characterized by fractional particle counts $f_i^{(n)}$ in size bin i, the fractional volume distribution $f_i^{(v)}$ in bin i may be computed as:

$$f_i^{(v)} = \frac{f_i^{(n)} d_i^3}{\sum_m f_m^{(n)} d_m^3}, \tag{5}$$

where d_i is the geometric mean diameter of size bin i and is computed as:

$$d_i = (d_{l,i} d_{u,i})^{\frac{1}{2}} \tag{6}$$

with $d_{l,i}$ and $d_{u,i}$ being the lower and upper particle diameters for bin i, respectively.

The SEM APA results span at least two orders of magnitude in particle size, with a lower limit of approximately 1 µm and an upper limit of 100 µm. Given the broad range of observed particle sizes, the conversion of PSD from number-basis to volume-basis format is inherently subject to uncertainty and possible bias.

Table 18. AN-101, AN-106, and AW-105 waste jar samples for particle size analysis.

Jar ID	Sample ID	Description
21407	S21T021230	AN-101, Segment 14 UH
21415	S21T021675	AN-101, Segment 18 LH
21417	S21T021747	AN-101, Segment 19 LH
20913	S20T016919	AN-106, Segment 14
21314	S20T017587	AN-106, Segment 16 LH
21360	S20T017884	AN-106, Segment 19 LH
21361	S20T017885	AN-106, Segment 19 UH
21366	S20T018217	AN-106, Segment 21 UH
21367	S20T018254	AN-106, Segment 22 UH
20326	S06T000217	AW-105, Segment 8 LH
19262	S06T000220	AW-105, Segment 8 UH

Firstly, since volume contributions are proportional to the cube of the particle diameter, the volume contribution of larger particles greatly exceeds that of smaller particles. For example, a single 100 µm particle contributes the same volume as one million 1 µm particles. Thus, while APA analysis reported in Buck et al. (2025) provides a robust sampling of particles in the 1 to 10 µm range, the volume-based distributions presented in this report are often dominated by a few large particles in the 10 to 100 µm range.

Additionally, APA analysis provides a primarily two-dimensional representation of particles. Conversion to a volume distribution using Eq. 5 assumes spherical geometry based on the measured APA particle diameter. This assumption may introduce further bias for particles that are large but flat, overestimating their volume contributions.

The combined effect of these two challenges—the dominance of large particles in volume-based distributions and geometric assumptions inherent in APA—results in volume distributions for particles >10 µm being subject to limited sampling and significant noise (variation).

5.3 Flow Behavior

The flow behavior of the nominally 5 %, 10 %, 15 %, and 20 % (by mass) composites was characterized using concentric cylinder rotational viscometry. Rotational viscometry evaluates the stress response of a material, τ, as a function of an applied shear rate, $\dot{\gamma}$ (also referred to as the rate-of-strain). Stress versus shear rate data can be interpreted using several constitutive equations, which describe the stress response of the material through a limited set of well-known constitutive parameters (such as viscosity, yield stress, and consistency).

The viscometer used in this study was a Haake Rotovisco® RV20 measuring system equipped with an M5 measuring head and an RC20 controller. This “M5” viscometer operated in a controlled rotational rate mode, with slurry temperature maintained using an M5 water jacket thermostated by an external recirculating chiller/heater.

A Haake MV1 concentric cylinder geometry with a 1 mm gap was employed for all characterizations. Additionally, a limited set of rheological measurements for the 20 % Fe and 14.6 % PO_4 composites utilized a smaller Haake MV2 concentric cylinder geometry with a 2 mm gap. This adjustment was necessary to mitigate the effects of large particles within the composite, which periodically caused binding of the rotor during flow curve measurements.

Flow curve data can be interpreted using constitutive equations to describe flow behavior using nominally one to three constitutive parameters. For the present report, the flow behavior is characterized using two constitutive models:

Newtonian Newtonian fluids flow under any applied stress and exhibit constant viscosity across all shear conditions. The constitutive flow curve for Newtonian fluids is expressed as:

$$\tau = \mu\dot{\gamma} \tag{7}$$

where μ is the Newtonian viscosity.

Bingham Plastic Bingham plastics describe yield stress fluids, which require a finite yield stress (τ_o) to be exceeded before flow occurs. Once flow is initiated, the stress response increases linearly with the shear rate. The constitutive equation for Bingham plastics is:

$$\tau = \tau_o + k_o\dot{\gamma} \tag{8}$$

where τ_o is the Bingham yield stress and k_o is the Bingham consistency.

In the present study, all flow curve measurements consisted of three segments:

1. An initial 5 min segment during which the shear rate was ramped linearly from 0 to $1000\,\mathrm{s}^{-1}$.
2. A hold at $1000\,\mathrm{s}^{-1}$ for at least 1 min.
3. A 5 min linear decrease in shear rate from $1000\,\mathrm{s}^{-1}$ to 0.

It should be noted that the upper limit of $1000\,\mathrm{s}^{-1}$ shear rate is specific to the MV1 geometry. For the limited measurements performed with the MV2 geometry, the larger gap precluded achieving the same upper shear rate due to rotational speed limits of the M5 measuring head and the onset of secondary flows, which complicate the quantification of rheology. As such, flow curves performed with the MV2 geometry set the upper shear rate bound to $500\,\mathrm{s}^{-1}$.

In general, samples demonstrated minimal difference between the increasing and decreasing shear rate segments, indicative of limited hysteresis. For each measurement, rheological constitutive parameters for the slurries were determined through linear regression of the flow curve data against Eq. 7 or Eq. 8. The choice of the appropriate constitutive model was guided by assessments of individual flow curves:

- Systems exhibiting a finite yield stress (defined as $\tau_o \geq 0.5$ Pa, governed by the torque measuring limit of the M5-MV1 measuring system) were treated as Bingham Plastics.
- Systems not exhibiting yield stress were treated as Newtonian.

For all fits, data from the final, decreasing shear rate segment of the flow curve were used, as these data correspond to the most highly sheared composite. Evaluating well-sheared material minimizes the effects of time-dependent behaviors, providing the best perspective on composite rheology. Thus, the best-fit Newtonian viscosities and/or Bingham parameters derived from this analysis represent the behavior of "well-mixed" vessels or slurries that have undergone pumping and recirculation.

5.4 Shear Strength

The shear strength of the 20 % by mass composites was measured using the same small Haake M5 measuring system employed to evaluate composite flow behavior (see previous section). All shear strength measurements were conducted after allowing fully-suspended composite solids to settle for 165 h (~7 d).

For context, shear strength represents the stress required to initiate motion in a bed of settled solids. For Hanford waste slurries that have undergone settling, a finite stress must be applied to the settled solids

layer before it begins to "flow." This stress, which transitions the solids from elastic deformation to viscous flow, is referred to as shear strength. The origin of shear strength can be attributed to static and kinetic friction between individual particles/aggregates, the strength of the interstitial fluid supporting the coarse fraction, and sludge cohesion arising from interparticle adhesive forces (e.g., van der Waals forces). The resistance of settled solids to motion is quantified through shear strength testing.

The vane technique measures the stress required to initiate motion by slowly rotating a vane immersed in the settled solids of the test sample while continuously monitoring the resisting torque over time. Although the rotational rate Ω used for measurement does not need to be exact, it must be sufficiently low to prevent the stress response of the material from being dominated by collisional or viscous effects. The present study employed $\Omega = 0.3$ RPM, a rate that has been used extensively in previous studies of Hanford waste sludge (Fiskum et al., 2008; Shimskey et al., 2009a; Lumetta et al., 2009; Fiskum et al., 2009a; Shimskey et al., 2009b; Snow et al., 2009; Edwards et al., 2009; Fiskum et al., 2009b; Burns et al., 2009).

A material's static shear strength is determined from the maximum torque required during the transition from initial to steady-state vane rotation. The shear strength is then calculated based on this maximum torque under the assumption of a uniform stress distribution on the vane tool geometry.

A typical experimental setup for shear strength measurement using a vane tool is depicted in Figure 12. An example torque versus time curve is shown in Figure 13.

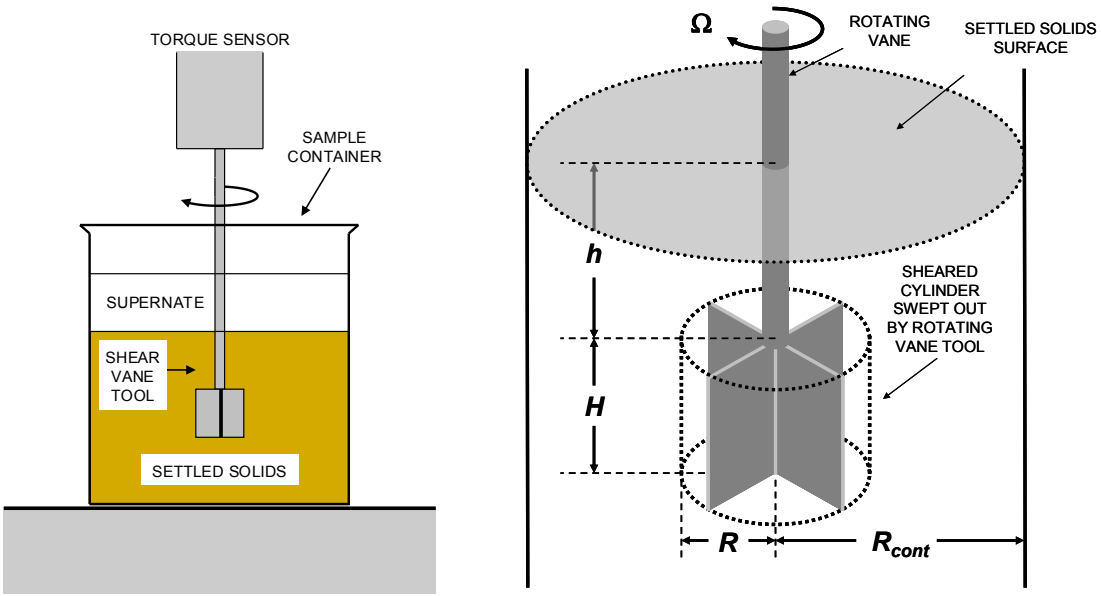


Figure 12. Typical shear strength experimental setup. A sludge/slurry sample in a container of radius R_{cont} is allowed to settle over a defined period of time. A vane tool connected to a viscometer (torque sensor) is submerged into the settled solids portion of the sample to a depth h (measured from the top of the vane blades). The vane blades have a radius R and a height H. The vane is rotated slowly at a constant rotational speed, Ω, and the torque versus time profile is recorded. The maximum torque required to initiate rotation is identified, and the shear strength is calculated based on the vane geometry and distribution of stress.

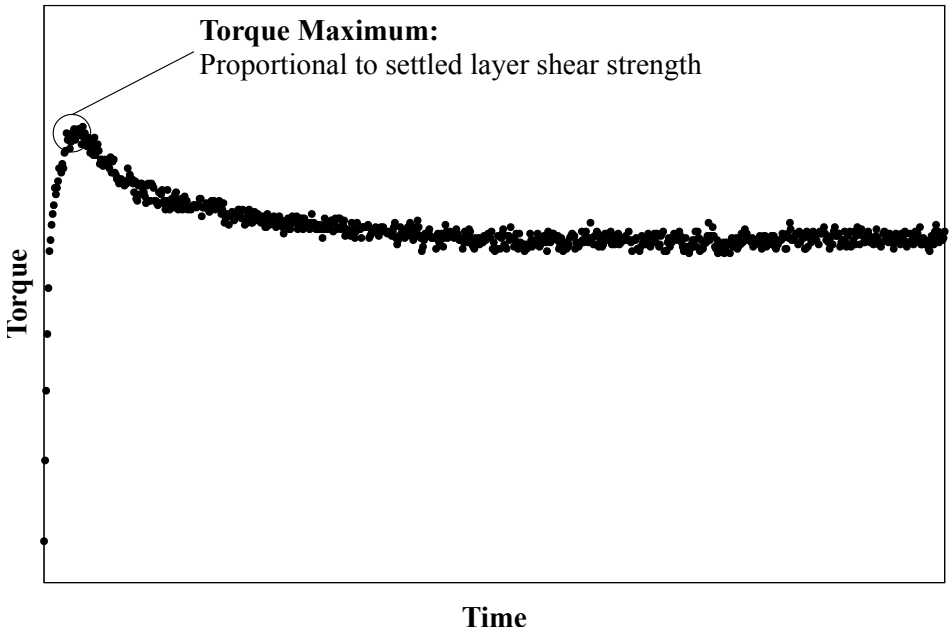


Figure 13. Example shear strength torque versus time curve. The maximum torque corresponds to the point at which motion begins. At this point, the applied stress from the vane rotation becomes sufficient to overcome frictional, cohesive, and other structural forces stabilizing the settled solids.

The maximum torque required for incipient motion depends on the geometry of the vane tool. To account for these geometric effects, shear strength is expressed as a uniform and isotropic stress acting over the cylindrical surface area swept out by the vane during rotation. This uniform stress (referred to as the shear strength of the material) is related to the maximum torque during incipient motion by the equation:

$$\tau_{\mathrm{s}} = \frac{2M_{\mathrm{max}}}{\pi D_v^3 \left(\frac{H_v}{D_v} + \frac{1}{3}\right)}. \tag{9}$$

Here:

- τ_{s} is the shear strength,
- M_{max} is the maximum torque recorded during incipient motion,
- D_v and H_v are the diameter and height of the vane tool used for measurement.

For the present study, a four-paddle vane with a diameter and height of 16 mm was used for all shear strength measurements. Vane dimensions are often referenced using a shorthand notation ($D_v \times H_v$), with the vane tool used in this study referred to simply as the 16×16 mm vane.

The proximity of the vane to the inner surfaces of the sample container, as well as its distance from the free surface of the settled solids, can influence shear strength results. To ensure the test is independent of container geometry, certain geometric constraints must be satisfied. These constraints are summarized in Table 19, which also includes example constraint dimensions for the 16×16 mm vane tool used in the current study.

Table 19. Vane immersion depth and container geometry constraints for shear strength tests using the vane technique.

Constraint	Criterion	For 16×16 mm (D×H) Vane
Vane height (H) to diameter (D)	$H < \frac{7}{2}D$	$H < 28\,\text{mm}$
Container diameter (D_{cont}) to vane diameter (D)	$D_{\text{cont}} > 2D$	$D_{\text{cont}} > 16\,\text{mm}$
Immersion depth (h) to vane height (H)	$h > H$	$h > 16\,\text{mm}$
Separation between bottom of vane and container floor (h_{floor})	$h_{\text{floor}} > \frac{1}{2}H$	$h_{\text{floor}} > 8\,\text{mm}$

5.5 Settling Rate, Settled Solids Volume, and Sludge Density

Settling tests were performed on the nominally 5 %, 10 %, 15 %, and 20 % composites to estimate settling rates and quantify the final settled solids volume percent. These tests provide supplementary data useful for interpreting measured NJS and mobilization strengths. Settling tests were conducted in dedicated 100 mL Grade-A borosilicate volumetric settling flasks, which feature wide-mouth tops and screw-on lids to facilitate sample loading, mixing, and to limit evaporation over the settling period.

For each measurement, the composites were carefully mixed within their parent bottles, after which they were quickly and carefully transferred to the settling flasks to avoid settling-induced bias in solid content. The settling samples were mixed again after transfer and allowed to settle over a 24 h period. During this settling period, the samples were continuously monitored through digital recordings, with periodic visual inspections by staff at the beginning and end of the test period.

The settling flasks have major volume gradings at 5 mL intervals and minor gradings at 1 mL. Evaluation of the settling flask geometry confirmed a nominal internal diameter of 2.6 cm and a highly linear level-to-volume correlation, with a slope of approximately $0.189\,\text{cm}\,\text{mL}^{-1}$.

The extent of settling was quantified as the percentage of flask volume occupied by the settled solids layer. For volumetric flask measurements, determination of settling extent did not require a level-volume correlation, as the flask gradings directly represent absolute volume. The extent of settling was calculated as:

$$v_{24} = \frac{V_{24}}{V_0} \tag{10}$$

where V_n denotes the absolute volume of settled solids at time n (in hours), and v_n represents the percent settled solids volume at time n. The extent of settling can be used to assess two key settling and settling rate metrics. First, for the straight volumetric cylinders employed in present testing, the extent of settling at 24 h equals the ratio of initial volume fraction of the suspension (ϕ_0) to that in the final settled bed at 24 hour (ϕ_{24}). Thus,

$$\frac{\phi_{24}}{\phi_0} = v_{24} \tag{11}$$

Assuming settling is largely complete after 24 h, this ratio approximates the ratio solids content to its ultimate settling extent ϕ/ϕ_{max}, such that

$$v_{24} = \frac{\phi}{\phi_{24}} \simeq \frac{\phi}{\phi_{\text{max}}} \tag{12}$$

The second metric related to v_{24} is the "final" concentration of solids in the settled layer ϕ_f, which is given by:

$$\phi_f = \phi_{24} = \frac{\phi_0}{v_{24}} \tag{13}$$

This expression requires knowledge of the initial volume concentration of solids in suspension ϕ_0.

Settling rates were computed initially through regression of settled volumes V_n against time t_n. In general, the rate of settling exhibits largely linear behavior until the settling volume approaches its final state—this holds true across initial solids content and despite the presence of hindered settling effects. Specifically, most settled solids height versus time curves demonstrate an initial, linear and persistent settling period which transitions abruptly to a slower settling regime. Figure 14 illustrates this behavior for a nominally 5 % Fe composite.

Settling rate evaluation focuses exclusively on the initial linear settling period. Linear regression of settled solid volume V_n versus time t_n yields the volumetric settling rate r_v, expressed in units of $\mathrm{mL\,h^{-1}}$. To convert this into a "linear" settling rate, r_l, the volumetric rate is multiplied by the volume-to-height conversion factor c_f, such that:

$$r_l = c_f r_v \tag{14}$$

The factor c_f corresponds to the level-volume grading of the flask. Direct evaluation of this grading finds:

$$c_f = (0.1891 \pm 0.0004)\,\mathrm{cm\,mL^{-1}}. \tag{15}$$

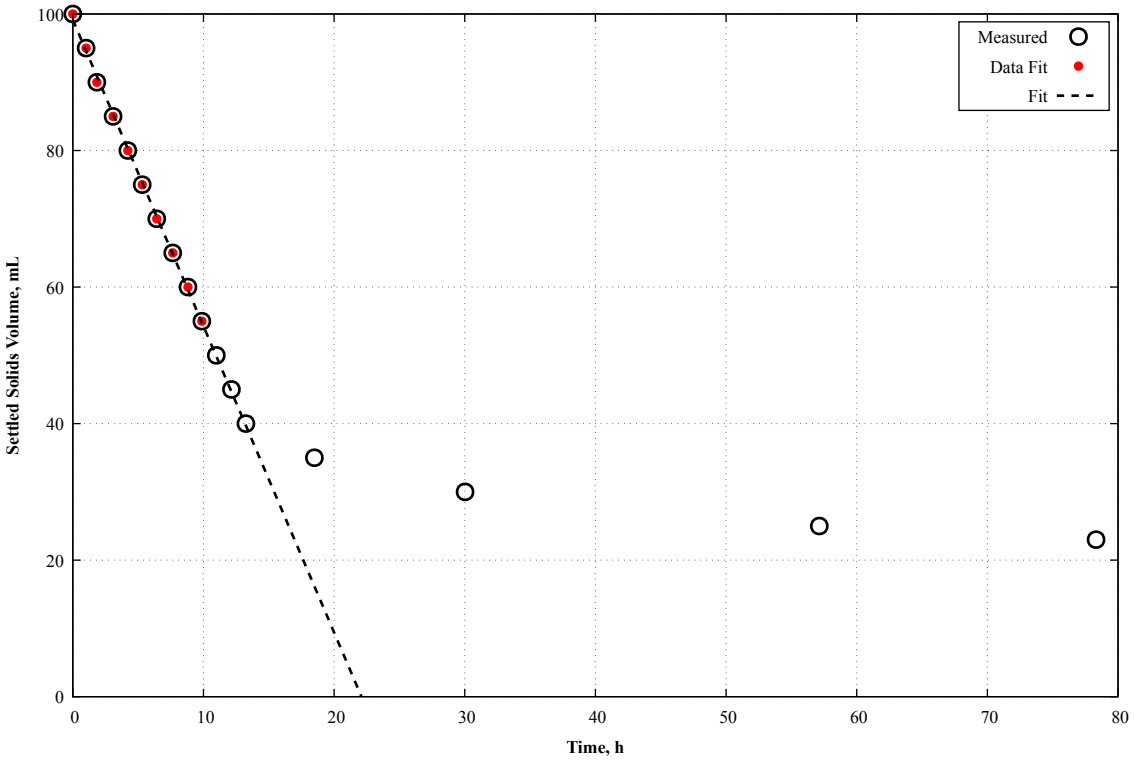


Figure 14. Example settling rate measurement showing the evolution of settled solids volume as a function of time. Measurement is performed in a 100 mL volumetric flask filled with nominally 5 % Fe composite slurry. The initial settling period, lasting up to approximately 14 h and reaching 40 % settled solids volume, exhibits a linear and rapid settling behavior. After this period, settling slows significantly as the settled layer undergoes compaction. The analysis focuses on the rapid, linear settling region to estimate the "initial" settling rate via linear regression. All measured data points are represented as black, unfilled circles. The data fitted in the "linear" region are highlighted in red points. The best-fit linear regression line is represented as a dashed curve.

Settling tests involve placing a known volume of well-mixed composite V_c into a graduated volumetric flask. By recording the net mass of composite, m_c, placed into the 100 mL cylinder, the composite density ρ_c can be calculated as:

$$\rho_c = \frac{m_c}{V_c}. \tag{16}$$

The NJS was measured for each of the nominally 20 % composites. The experimental setup and measurements for the five SE quadrant waste composites were conducted as part of a companion effort to those outlined in the present report. A complete workup and detailed analysis of these NJS tests can be found in Bachman et al. (2025). Here, the NJS is defined as the overhead mixing speed required to fully remobilize composite waste solids that had settled over a 24 h period.

For each NJS test, approximately 150 mL of fully-suspended composite was placed into a small plastic container and left to settle for 24 h. At the end of the settling period, an overhead mixer was inserted into the container and its mixing speed was gradually increased until full, off-bottom mobilization of the settled solids was observed. To facilitate observation during mixing, the vessel was placed on top of a clear acrylic table, allowing the bottom of the container to be continuously monitored using an in-cell camera.

For all composites except the Fe composite, particle motion and off-bottom suspension were readily observed during mixing. However, the initial NJS test for the Fe composite showed no discernible change in the appearance of the container bottom that indicated particle motion. To address this, a second successful Fe composite NJS test was conducted at the conclusion of all physical characterizations reported in this study. For this second test, a zirconium oxide (ZrO_2) tracer/sentinel particle was added to the Fe composite. This addition provided a visually distinct indicator of bottom motion—the off-white ZrO_2 particles contrasted clearly against the dark-red Fe composite background.

In the present report, select NJS values from Bachman et al. (2025) are presented to complement the corresponding physical and settling rate measurements. This association of NJS data with physical and settling behavior aims to provide a "complete" picture of composite transport dynamics.

5.6 Composite Serial Dilution

As outlined in the preceding sections and in Table 16, select physical properties were evaluated at nominal composite UDS concentrations of 5, 10, 15, and 20 % by mass. In the present study, alteration of UDS was achieved through serial dilution of the composites using simulated supernatant.

Initial preparation of the composites targeted a UDS content of 20 %. Adjustment to 15 % UDS was accomplished by calculating the net mass of supernatant required to dilute from 20 % to 15 %, given by:

$$m_{s,1} = \frac{1}{3} m_o \tag{17}$$

where $m_{s,1}$ represents the mass of supernatant needed for the first dilution step, and m_o is the net mass of the original 20 % composite. The factor of 3 is specific to the 20 to 15 % dilution step.

Serial dilutions to 10 and 5 % UDS followed similar calculations. The mass of supernatant for 10 % dilution, $m_{s,2}$, was calculated as:

$$m_{s,2} = \frac{1}{2} m_1, \tag{18}$$

whereas the mass of supernatant for 5 % dilution, $m_{s,3}$, was:

$$m_{s,3} = m_2. \tag{19}$$

Here, m_1 and m_2 represent the net masses of 15 and 10 % composites to be diluted, respectively.

It should be noted that the serial dilution strategy was not modified for the PO_4 composite, despite its initial UDS of 14.6 % being lower than the nominal 20 % target. Consequently, serial dilutions of the PO_4 composite yielded dilution steps that were also lower than the nominal UDS targets.

Table 20 summarizes the serial dilutions realized for the PO_4 composite.

Table 20. UDS contents realized during serial dilution of the PO_4 composite.

Dilution Stage	Nominal UDS, %	Actual PO_4 UDS, %
Initial	20	14.6
First	15	11.0
Second	10	7.3
Final	5.0	3.7

5.7 Composite Transfers and Sampling

Most of the characterization methods outlined above required frequent sampling handling and transfer. Prior to sub-sampling or transfer events involving waste composite solids, efforts were made to assure sample uniformity by vigorously resuspending each composite. For composites whose solids had settled during storage or testing, containers were inverted after mixing to confirm complete resuspension of settled solids. Once mixed, sampling and transfers operations were completed as quickly as practicable to limit settling and re-stratification that could impact the fidelity of the derived samples. However, the need to handle all composites remotely in a shielded environment due to their radioactivity grossly limited the efficacy of in-cell mixing (generally done by tumbling composite bottles head-over-head with a remote manipulator) and extended sampling times due to limited in-cell manipulator speed and dexterity. The presence of fast settling solids in the Al, U, and Zr composites (see Section 6) compounded sampling difficulties. While best efforts were made to assure composite uniformity during sampling and transfer, select physical and transport property results present in the sections that follow are inconstant with expectations (e.g., based on nearest neighbors), with the likely cause being poor (non-representative) sampling of composite solids. These inconsistencies will be noted where they are observed, at least to the extent that the results are discussed in the report.

6.0 Results and Discussion

The present section documents the chemical and physical properties of the five SE quadrant waste composites/exemplars discussed in Sections 3 and 4. To provide the most complete narrative possible, chemical and solid information already presented in Section 4 is reiterated here. Particle size information and NJS test results have been adapted from Buck et al. (2025) and Bachman et al. (2025), respectively. The primary intent of this section is to provide an overview of physical characterization results, and will be followed by a global discussion of the findings in the context of SE waste handling operations in Section 7.

6.1 Solid and Liquid Phase Chemistry

The solid and liquid phase chemistry of the prepared composites has been partially presented in preceding sections of this report. Table 21 lists the solid and liquid phase chemistry of the SE quadrant composites as measured through a combination of ICP-OES, IC, titration, and TIC/TOC analyses. Figure 15 presents the fractional solids phase composition for each composite.

As noted in Section 4, solid-phase compositions generally align with expectations for most analytes except sodium (Na) and phosphate (PO_4). All composites contain significantly more sodium than anticipated based on the analytical data in Jordan (2022a,b) and Disselkamp (2009), coupled with a noticeable deficit of phosphate. While this discrepancy could reflect phosphate loss from the solid phase to the composite supernatant via dissolution during compositing, measurements of the final composite supernatant indicate PO_4 concentrations align with expectations to within typical IC uncertainty (± 20 %) for all composites except the Zr composite, which displayed large deviations for all analytes.

The causes behind sodium and phosphate deviations are not immediately clear but may result from a combination of factors: differences in analytical handling between the present and historic studies, variations in the underlying waste composites used for the current work versus prior efforts, sub-sampling challenges (e.g., analyzing 20 % composite slurry rather than centrifuged sludge samples), and the methods employed to recover and re-slurry solids in the present study.

Despite these discrepancies, compositing efforts successfully achieved the desired goal: creating five SE quadrant waste exemplars enriched in their corresponding target analyte. In summary, the Al composite exhibits substantial contributions from aluminum-bearing solids, the Fe composite from iron-bearing solids, and similarly for PO_4, U, and Zr.

6.2 Particle Size Distribution

Size analysis of select samples from AN-101, AN-106, and AW-105 solids was performed using APA combined with SEM-EDS-based imaging. This analysis, as reported in Buck et al. (2025), provided measurements of size distributions for target waste mineral phases such as calcite, cancrinite, and natrophosphate. For the purposes of the present report, the minerals and size distributions of interest are those associated with the target analytes: Al, Fe, PO_4, U, and Zr.

Table 22 itemizes the association of target analytes with mineral phases (reported in Buck et al. (2025)) that are relevant to this study. As detailed in Section 5, PSD data were converted to their corresponding volume distributions for the select mineral phases listed in Table 22. The volumetric particle size distributions for these associated mineral phases are shown in Figure 16.

All evaluated mineral phases exhibit particle sizes spanning the range observable through optical microscopy, specifically 1 to $\sim$50 µm. Differences in size distributions primarily manifest through variations in the location of the primary particle mode for each mineral phase.

Table 21. Summary of measured (actual) composite solid and liquid phase chemistry. Solid-phase analyte concentrations are in mg g^{-1} (dry solids basis). Liquid-phase analyte concentrations are in M. Note: solid-phase data have been previously reported in Table 15.

Analyte	Concentration for Composite				
	Al	**Fe**	**PO_4**	**U**	**Zr**
			Solids, mg g^{-1}		
Al	418	115	80.6	201	25.2
Cr	0.685	2.89	2.57	0.344	13.1
Fe	48.7	142	48.6	84.6	32.2
Na	142	232	305	214	358
PO_4	27.4	1.87	161	98.9	6.49
U	36.7	23.5	87.9	173	67.3
Zr	0.0634	18.3	0.0155	0.005 36	229
			Supernatant, M		
Al	0.232	0.279	0.215	0.0837	0.006 31
Cl	0.0562	0.112	0.0955	0.0589	0.007 41
F	0.112	0.0504	0.124	0.121	0.171
OH	1.25	1.04	0.956	0.504	0.254
NO_3	0.881	1.63	1.48	0.956	0.394
NO_2	1.11	1.64	1.48	1.15	0.0595
PO_4	0.0241	0.0357	0.0205	0.0364	0.003 86
Na	4.88	6.49	5.76	4.56	1.13
SO_4	0.0431	0.0380	0.0464	0.0366	0.004 55
CO_3	0.543	0.780	0.622	0.750	0.11

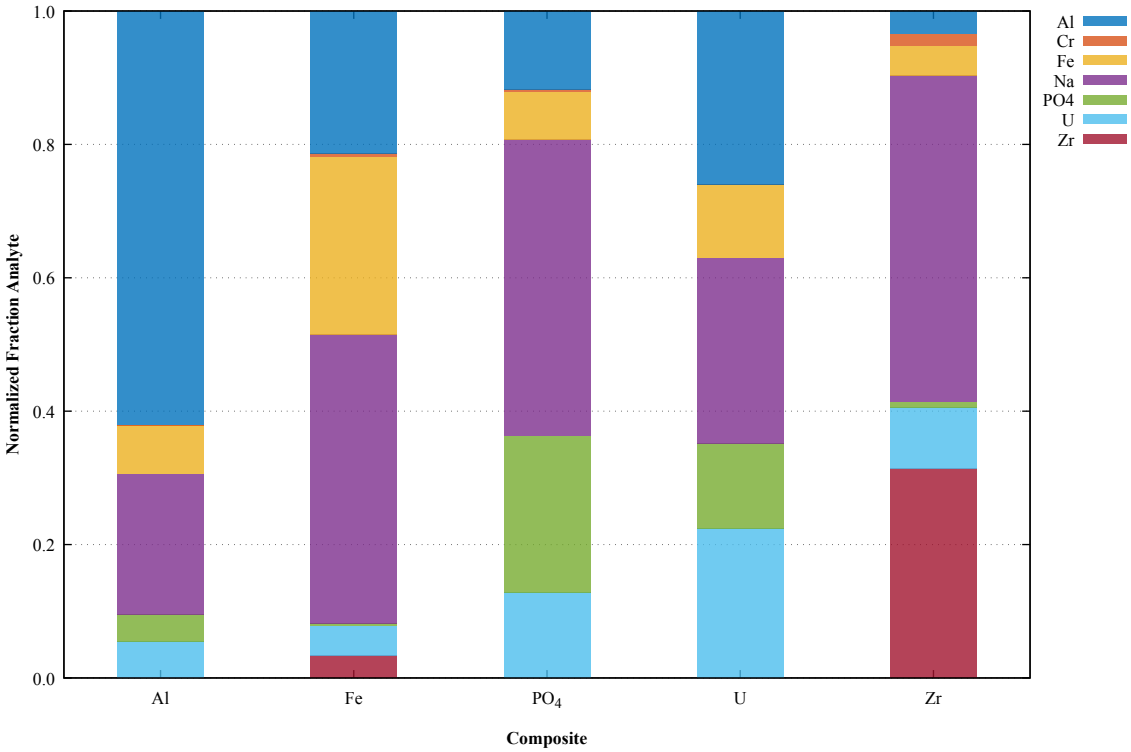


Figure 15. Fractional solid-phase composition for the five composites.

For AN-101, AN-106, and AW-105 solids analyzed:

- Zirconia and natrophosphate solids exhibit the largest fractions of "large" particles, with peak volume populations in the 20 to 30 µm range.
- Gibbsite shows a broad distribution, with a primary population of 30 to 40 µm particles and a secondary mode from 10 to 20 µm.
- Hematite and clarkeite display the highest populations of fines, with a primary mode at 10 µm and significant numbers of particles in the 1 to 20 µm range.

Table 22. Association of target analytes with mineral phases identified in Buck et al. (2025). Mineral phase densities are taken from the WebMineral mineralogy database (`https://webmineral.com`). Zirconia takes mineral data for baddeleyite (ZrO_2).

Analyte	Mineral	Density, kg m^{-3}
Al	Gibbsite [$Al(OH)_3$]	2340
Fe	Hematite [Fe_2O_3]	5300
PO_4	Natrophosphate [$Na_7(PO_4)_2F \cdot 19\,H_2O$]	1710
U	Clarkeite [$Na_{0.7}Pb_{0.1}Ca_{0.1}(UO_2)_{0.9}O_{0.9}(OH)_{1.1} \cdot 0.1\,H_2O$]	6390
Zr	Zirconium Dioxide [ZrO_2]	5750

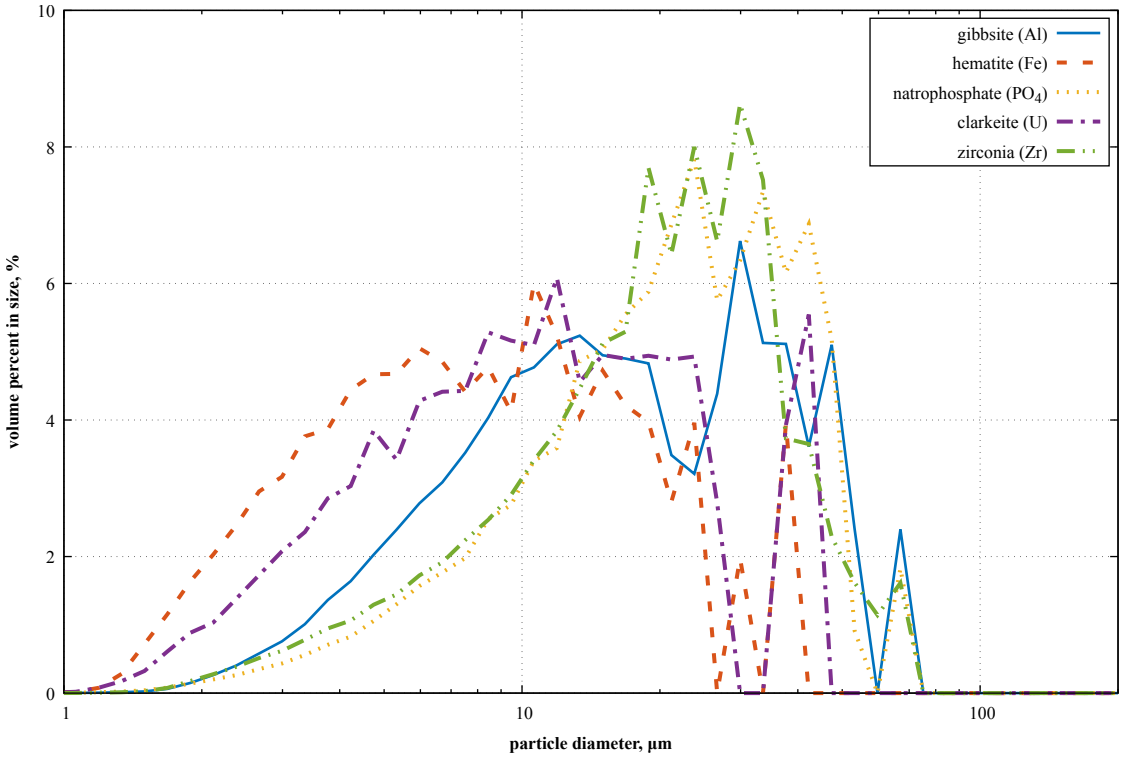


Figure 16. Volume-based size distributions for key analyte-associated mineral phases. Analyte associations are described in Table 22.

The PSDs shown in Figure 16 represent size distributions for specific mineral phases found in the SE quadrant wastes. These PSDs are derived from observations of individual mineral phases across samples taken from AN-101, AN-106, and AW-105 solids received for the present study. It is important to note that these mineral phase PSDs are generalized and do not account for potential variations in particle sizes between the same mineral phases sourced from different tanks. For example, the size distributions for AN-101 gibbsite and AN-106 gibbsite are not considered separately.

With this limitation in mind, the mineral phase PSD data can be combined with the solid-phase data shown in Figure 15 to estimate the PSD of the five composites. This estimation couples the weight fraction of each analyte with its associated mineral phase, chemical formula, and density to calculate the volume contribution occupied by each mineral in the composite solids. The volume contribution for mineral i in a composite is calculated using:

$$y_i = \frac{\left(\frac{\xi_i M_i^{(m)}}{\rho_i^{(m)} M_i^{(a)}}\right) w_i^{(a)}}{\sum_j \left(\frac{\xi_j M_j^{(m)}}{\rho_j^{(m)} M_j^{(a)}}\right) w_j^{(a)}}, \tag{20}$$

where:

- $w_i^{(a)}$ is the weight fraction of analyte i (e.g., Al, Fe),
- $M_i^{(a)}$ is the formula weight of the analyte,
- ξ_i is the stoichiometric quantity of analyte,
- $M_i^{(m)}$ is the formula weight of the mineral phase, and
- $\rho_i^{(m)}$ is the density of the mineral phase.

The y_i values for each composite are then used alongside the mineral phase PSDs presented in Figure 16 to compute per-composite size distributions via:

$$f_k^{(\text{composite})} = \sum_i y_i f_k^{(m,i)} \tag{21}$$

where $f_k^{(\text{composite})}$ is the estimated composite PSD, and $f_k^{(m,i)}$ is the PSD for mineral i.

The resulting size distributions for each composite are shown in Figure 17, which indicates that the PSDs across composites are largely similar. Estimates of the mean particle diameter for each composite find that all fall within (21 ± 2) µm. Care must be taken when evaluating the upper bound fraction of the PSDs, as this region (which contributes significantly to settling) has higher uncertainty due to limited sampling in optical microscopy.

Despite this uncertainty, the overall similarity in composite PSDs suggests that variations in settling rates are likely governed by factors such as particle density or inter-particle interactions. These interactions can influence the formation of space-filling particle structures and agglomerates, and subsequently affect settling rates and rheological behavior.

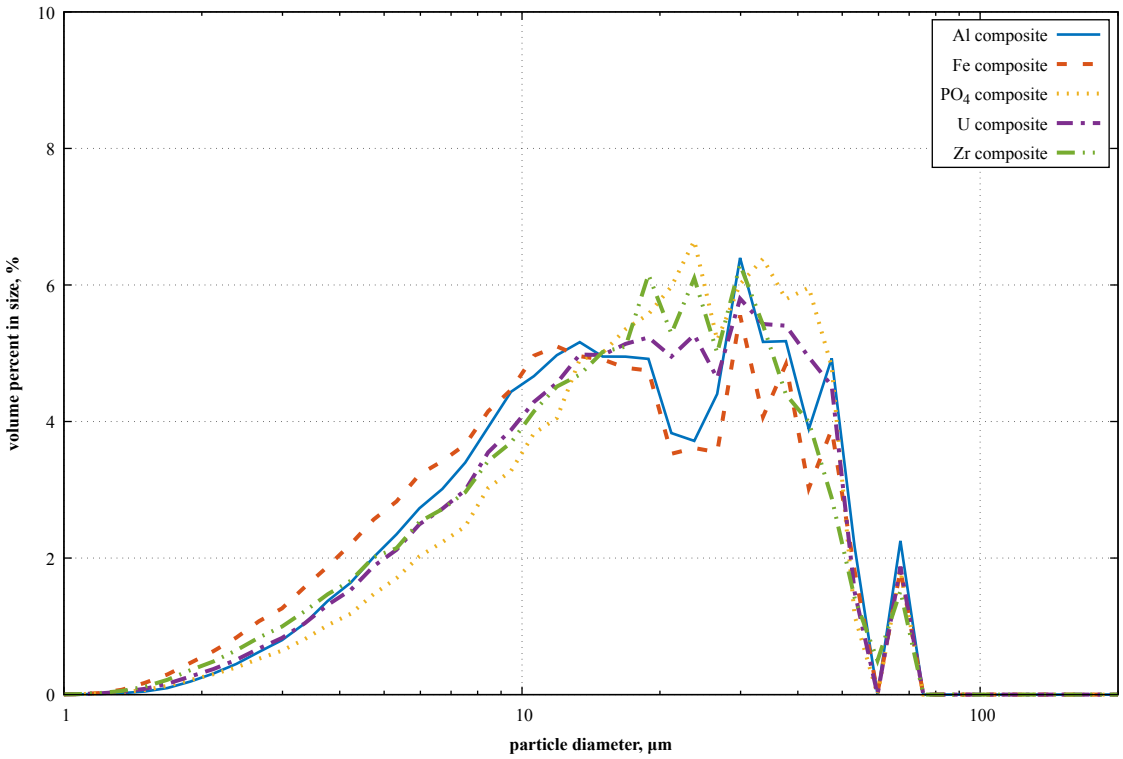


Figure 17. Estimated size distributions for the five SE quadrant waste composites. Size distributions are estimated using a combination of solids-phase chemistry presented in Figure 15 and mineral-phase specific size data presented in Figure 16.

6.3 Solid Phase Density

With respect to solid-phase density, the association of solid-phase analytes with specific mineral phases provided by Table 22 enables estimates of mixed solids density when combined with measured composite chemistry. However, these associations do not explicitly define a Na phase beyond its natural connection to PO_4. Despite this limitation, density estimates based on composition provide a useful baseline for evaluating settling behaviors.

Using the y_i values calculated for PSD analysis, the mixed solid density of each composite's solids (ρ_b) can be estimated by:

$$\rho_b = \sum_i y_i \rho_i^{(m)}, \tag{22}$$

where $\rho_i^{(m)}$ is the density of mineral i, and y_i represents the fractional volume contribution of each mineral phase.

Table 23 lists the calculated solid-phase densities using this formula.

Table 23. Estimate of solid phase bulk density for each composite. Estimates employ the solid phase/composite associations listed in Table 22 in conjunction with the solid phase chemistry presented in Figure 10. Densities are calculated using Eq. 22.

Composite	Solids Density, kg m^{-3}
Al	2400
Fe	3100
PO_4	2130
U	2520
Zr	4480

This analysis finds that composite solid-phase density increases in the following order: PO_4, Al, U, Fe, and Zr. The Al and U composites exhibit similar densities, approximately $2500\,kg\,m^{-3}$. Notably, the Zr composite solids, with an estimated density of approximately $4500\,kg\,m^{-3}$, are significantly more dense than the other four composites.

6.4 Flow Curve and Shear Strength

Table 24 summarizes the flow curve analysis results for the five composites and the simulated supernatant. As indicated by the constitutive parameters, all composites except the Fe and PO_4 composites exhibited Newtonian behavior. Non-Newtonian behavior persisted down to a UDS of 15 % for the Fe composite and 10 % for the PO_4 composite.

Among the two non-Newtonian systems, the PO_4 composite exhibited the largest yield stress of 5.7 Pa at 20 %. Despite having a lower yield stress, the Fe composite demonstrated the largest consistency parameter of 24.9 mPa s, which may be partly attributed to the viscosity of the underlying supernatant (the highest among the five simulated carrier fluids).

The non-Newtonian character of the Fe and PO_4 composites suggests that their solids form volume-filling structures, contributing to the semi-solid-like behavior seen in the constitutive analysis. Such behavior is expected to manifest in dispersions that settle slowly and to a limited extent. As discussed in the subsequent subsection, the settling behavior of the Fe and PO_4 composites aligns with these expectations—both composites settle significantly slower relative to the Al, U, and Zr composites.

Table 24. Summary of constitutive rheological parameters for the five SE quadrant composites at nominal UDS of 5, 10, 15, and 20 % and their corresponding supernatant. Entries marked with "n/m" indicate systems that were not measured due to the similarity of their next higher solids concentration to the supernatant rheology. Not measured entries should be considered near or equivalent to their corresponding supernatant. Entries are marked with "– –" where the parameter is not applicable (such as a yield stress for a Newtonian fluid).

Composite	Behavior	Yield, Pa	Viscosity or Consistency, mPa s
	20 % *composite*		
Al	Newtonian	– –	5.0
Fe	Bingham	2.1	24.9
PO_4	Bingham	5.7	21.2
U	Newtonian	– –	5.1
Zr	Newtonian	– –	7.5
	15 % *composite*		
Al	Newtonian	– –	4.8
Fe	Bingham	1.1	20.8
PO_4	Bingham	2.7	13.4
U	Newtonian	– –	4.9
Zr	Newtonian	– –	5.3
	10 % *composite*		
Al	– –	n/m	n/m
Fe	Newtonian	– –	10.9
PO_4	Bingham	0.6	8.4
U	– –	n/m	n/m
Zr	Newtonian	– –	3.8
	5 % *composite*		
Al	– –	n/m	n/m
Fe	Newtonian	– –	6.8
PO_4	Newtonian	– –	5.5
U	– –	n/m	n/m
Zr	Newtonian	– –	1.9
	Simulated Supernatant		
Al	Newtonian	– –	3.6
Fe	Newtonian	– –	5.1
PO_4	Newtonian	– –	4.2
U	Newtonian	– –	2.8
Zr	Newtonian	– –	1.5

The observed flow curves largely conform to theoretical expectations for Newtonian and Bingham Plastic systems. Figures 18 and 19 provide representative examples for Bingham Plastic and Newtonian slurries at 20 % UDS.

The non-Newtonian behavior observed for the Fe and PO_4 composites is consistent with the Bingham Plastic constitutive equation, exhibiting minor deviations at both low and high ends of the tested shear rate range. For example, in Figure 18, the upper bound of evaluated shear rates is limited to $500\,s^{-1}$ due to the use of the larger gap MVII geometry. However, upper shear rate deviations are not unique to the MVII geometry and were observed in several flow measurements throughout this study. These deviations are most likely attributable to sample overfill and secondary flow onset, rather than material-dependent phenomena such as shear-induced agglomeration.[1]

The lower bound deviations from linearity, characterized by negative curvature in flow curves, are typical of slurries and can be better modeled using the Casson constitutive equation. In practice, the Casson equation incorporates non-linear square root terms, which make it more complex to use for first-order engineering analysis. For the present study, the Bingham Plastic equation was employed, resulting in minor over-estimation of yield stress for fully mixed slurries. This over-estimation renders downstream predictions of pumping requirements (to maintain flow for the tested non-Newtonian composites) conservative.

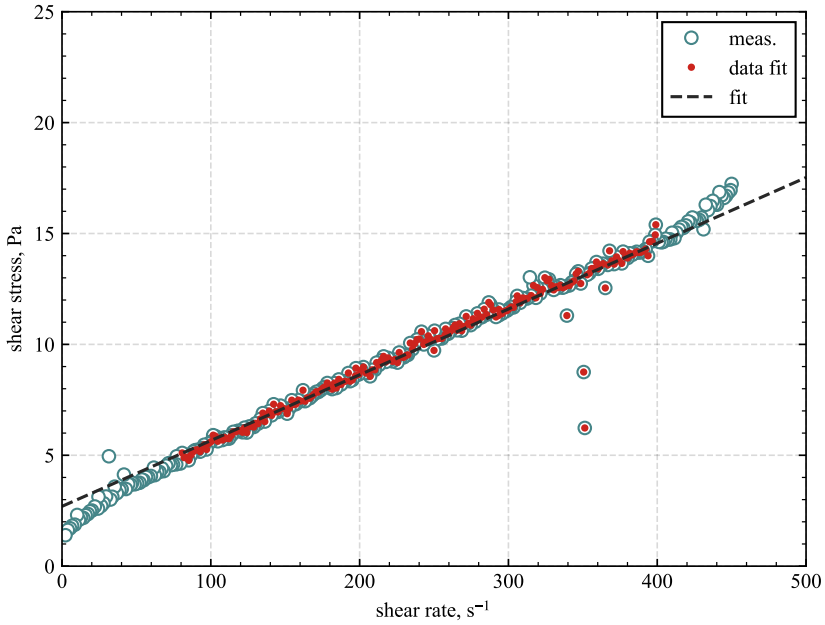


Figure 18. Example flow curve for the 20 % Fe composite showing non-Newtonian behavior. Measurement was performed with a 2 mm gap MVII concentric cylinder geometry. Use of this geometry leads to reduced shear rate range and possible secondary flows above $400\,s^{-1}$ (as suggested by the non-linear increase in stress beyond this shear rate).

[1]Overfill refers to material inadvertently spilling onto the top of the rotor during sample loading or due to minor gap misalignment. At high overhead mixing speeds, centrifugal forces can cause overfill to migrate into the shear gap, increasing slurry contact and shear area, which leads to elevated apparent shear stress. While efforts were made to avoid overfill, minor overfills were tolerated to limit material loss from cleaning and reloading the rotor. As a result, some observed non-linear increases in flow curves at high shear likely derive from overfill migration. Secondary flow onset (Taylor vortices), which occurs in less viscous slurries, also contributes to non-linear increases and is dependent on gap size, with larger gaps having lower shear rate thresholds for onset.

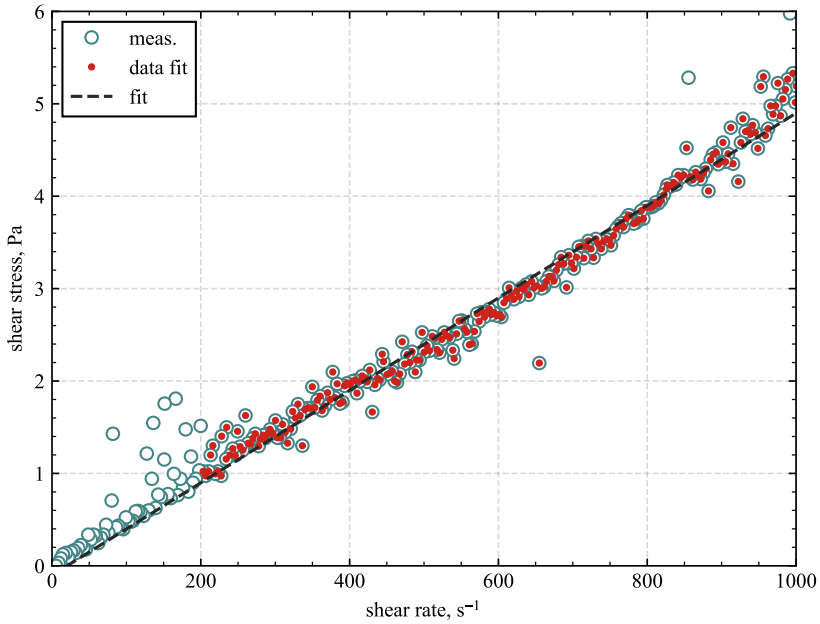


Figure 19. Example flow curve for the 20 % U composite showing Newtonian behavior. Measurement was performed with a 1 mm gap MVI concentric cylinder geometry.

The use of MVII geometry for 20 % testing was motivated by concerns regarding flow curve binding, which was observed during initial tests of the 20 % Fe composite with the 1 mm MVI geometry. A worst-case example of the observed binding behavior is shown in Figure 20. Binding is presumed to result from jamming of large particles within the narrow gap of the MVI geometry. Visual inspection of the 20 % composite confirmed the presence of large particles in the sample.

Interestingly, binding issues decreased over the course of rheometric testing, likely due to repeated handling of the composites. This handling may have "ground-down" larger particles or allowed for longer-term "hydration" of composite solids, promoting de-aggregation.

Flow curves affected by binding were analyzed by filtering outliers in shear stress measurements before applying linear regression. The extracted constitutive parameters from these filtered analyses aligned well with companion tests of the same composite that were not impacted by binding.

Figure 21 illustrates the solids content dependence of the measured yield stress and consistency (or Newtonian viscosity) for the series of rheology measurements performed herein. Log-log axes have been utilized, as this functional dependence is typical for slurry rheology.

With respect to measured yield stress, the data align with expectations that yield stress increases with increasing solids content. However, the limited number of yield stress measurements for the Fe and PO_4 composites (five total) prevents a more detailed characterization of the functional dependence of yield stress on solids content.

Regarding consistency, the expected increase with solids content is clearly observed. The Fe, PO_4, and Zr composite consistencies exhibit behavior consistent with a power-law relationship over the range of solids contents tested. This is typical for slurries far from their maximum packing or gel concentration—conditions where rheology rises precipitously.

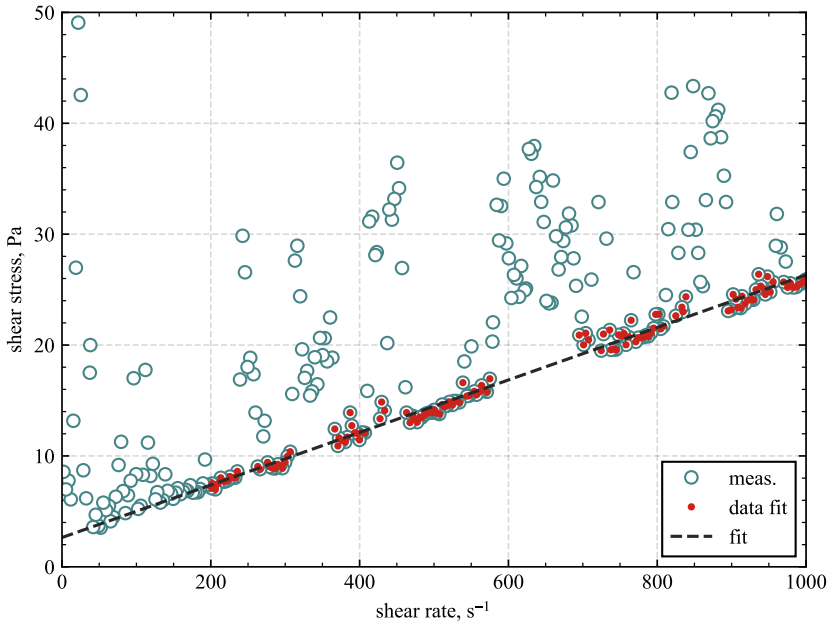


Figure 20. A worst-case example of "binding" behavior observed in 20 % composite testing. The measured flow curve shown here is for the 20 % Fe composite. Binding manifests as periodic jumps in measured shear stress relative to a baseline stress (presumed to correspond to the fluid itself). Measurement was performed with a 1 mm gap MVI geometry. Binding is associated with jamming of large particles within the cup and rotor annular gap.

As expected, all measured consistencies/viscosities exceed the viscosities of their corresponding supernatants. Notable observations include the apparent similarity in consistency between the Fe and PO_4 composites, as both fall on the same power-law "iso-line." The Fe and PO_4 composites exhibit the highest consistency values among the five composites for any given solids concentration.

The Zr composite, with four measurements, displays a similar power-law slope but has a consistently lower overall consistency compared to the Fe and PO_4 composites. This is notable as the Zr composite displays Newtonian behavior, whereas the Fe and PO_4 composites exhibit non-Newtonian behavior (at least above approximately 10 % solids content).

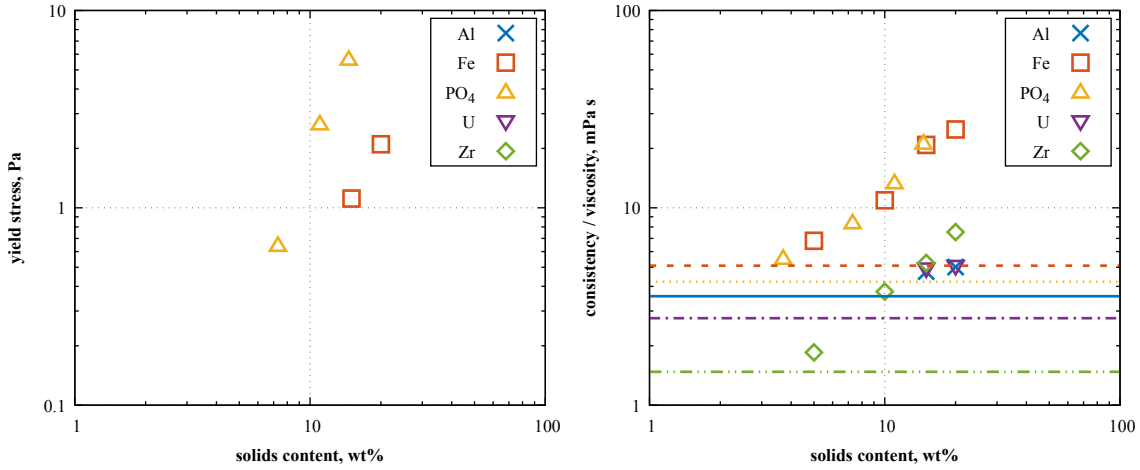


Figure 21. Measured SE quadrant composite rheology as a function of UDS content. The left-hand figure shows the yield stress functionality for non-Newtonian slurries. The right-hand figure shows the consistency (for non-Newtonian) or viscosity (Newtonian) functionality. Measured data are shown in open symbols for each composite chemistry. The solid and dashed lines represent the viscosity of the supernatant associated with each composite, defining the lower viscosity/consistency limit for each case.

Both the Al and U composites were Newtonian and demonstrated viscosities near that of their carrier fluid, even at 15 % solids loading. Given the similarity of "high" solids Al and U rheology to their solids-free suspending phase, further rheological testing at 5 and 10 % UDS contents was forgone to preserve composite inventory. This decision was based on the expectation that the rheology of the "lower" solids content Al and U composites would not appreciably differ from their supernatants.

The flow curve measurements and constitutive parameters describe well-sheared material, representative of behavior expected under flowing conditions. However, they do not provide information on material mobilization strength.

To assess mobilization strength, shear strength of the nominally 20 % composites was measured after approximately 165 h settling period. This settling period was selected as a representative upper bound for WTP mixing vessel outages. Table 25 summarizes the shear strength measurements for the 20 % composites as a function of depth.

The "standard" shear strength measurement, dictated by protocol, corresponds to a 16 mm immersion depth, equivalent to one vane diameter. It should be noted that the immersion depth is measured relative to the top of the vane blades, placing the top of the rotation cylinder swept by the vane 16 mm below the surface. At this standard depth, primary shear strength measurements reported in Table 25 range from 20 to 40 Pa. While approximately an order of magnitude greater than the largest composite yield strength observed in flow curve testing, these strengths are relatively weak compared to some Hanford sludges, which can exceed 1000 Pa [cf. Snow et al. (2009)].

For heterogeneous materials and granular solids, shear strength can vary with vane immersion depth due to lithostatic loads (for granular solids) and material stratification (e.g., preferential settling of dense, tightly packed layers at the bottom of the test container). In the present study, shear strength testing at increased immersion depths revealed evidence of material stratification and/or increased strength, with shear strength monotonically increasing with depth for all composites. However, for all composites except the U composite, this change in strength across the depth range was less than a factor of two.

The U composite exhibited remarkable variation in shear strength measurements at the deepest test depth of 36 mm, increasing from 59 to 1600 Pa over 10 mm. While there is inherent uncertainty in the actual immersion depth—arising from the estimation of vane travel distances via video footage or direct observation through the cell window—it is likely the vane was interacting with solids jammed against or in direct contact with the bottom of the test container. This conjecture is supported by the sum of the vane tool height (16 mm) and immersion depth (36 mm), which approximates the available depth of U solids (51 mm).

Table 25. Shear strength measurements for 20 % composites. The sludge height represents the total height of the settled layer, estimated from a linear measuring tape adhered to the exterior of the container used to measure shear strength. Measurements are performed using a 16×16 mm vane tool at the listed immersion depth. Excepting the 16 mm depth, which is marked on the vane, vane depth measurements are approximate and may be subject to gross error. Vane tests were performed in composite samples that had been transferred to smaller (100 mL) containers. Repeat measurements were only performed for the Al and U composites, due to concerns that high strength inventories had been left behind in the parent composite bottle. Entries are marked with "– –" when no measurement was made.

Composite	Sludge,	Primary Measurement		Repeat Measurement	
	Height, mm	Depth, mm	Strength, Pa	Depth, mm	Strength, Pa
Al	61	16	29	16	85
		31	26	32	101
		42	35	42	126
		50	47	50	109
Fe	57	16	21	– –	– –
		32	28	– –	– –
PO_4	58	16	24	– –	– –
		32	33	– –	– –
		48	45	– –	– –
U	51	16	42	16	41
		26	59	26	507
		36	1600	29	378
Zr	64	16	40	– –	– –
		32	49	– –	– –
		44	50	– –	– –
		54	55	– –	– –

Repeat shear strength measurements for the Al and U composites were performed to address specific concerns raised during primary testing. For the Al composite, shear strengths in the 100 to 1000 Pa range were expected based on prior testing of Al-rich Hanford wastes reported in Snow et al. (2009). The observed primary shear strengths for the Al composite fell significantly below these expectations, leading to concerns that dense Al composite solids may have been inadvertently left behind in the parent composite bottle during sub-sampling for shear strength testing. Rather than attempting to recombine the tested Al-composite solids into the parent bottle and re-sample, residual solids from the Al composite's parent bottle were consolidated into the shear strength sample and remixed. This required a partial decanting of supernatant from the Al-composite shear strength sample to accommodate the additional solids.

Retesting of the U composite was prompted by the observed spike in shear strength of 1600 Pa at the deepest immersion depth during primary testing. While this spike was likely due to the vane tool interacting with the bottom of the test container, residual U solids from the parent jar were consolidated into the shear strength sample, and the composite was retested.

The repeat shear strength measurements for the Al and U composites are summarized on the right-hand side of Table 25. As before, the composites were allowed to settle for approximately 165 h before measurement.

For the Al composite, repeat testing resulted in slightly elevated shear strengths relative to the primary measurements, ranging from 85 to 126 Pa. This suggests the primary sampling was likely affected by bias. However, the change is relatively minor, representing at most a factor-of-3.5 increase rather than an order-of-magnitude shift.

For the U composite, repeat measurements at the standard vane immersion depth of 16 mm were nominally equivalent to corresponding primary measurements. At deeper immersion depths, repeat shear strength measurements for the U composite showed substantive increases, ranging from 400 to 500 Pa. While this is still below the 1600 Pa maximum observed during primary testing, the elevated repeat strengths suggest the presence of granular or cohesive U composite solids that may be challenging to remobilize after settling.

6.5 Settling Volumes, Rates, and Density

Figure 22 provides an example of how composite solids (in this case, the Al composite solids) settle as a function of different UDS contents. Figure 23 compares settling rates among the composites at a fixed UDS content of 10 %. A comprehensive itemization of settling curves for all composites and UDS concentrations tested is provided in Appendix B.

The two specific examples shown here are representative of the broader settling trends observed within the dataset. However, important differences in settling characteristics are evident when comparing settling rates across the variety of composite and concentration combinations tested.

Settling behavior in dense slurries reflects a complex interaction between several factors:

- Solid size, density, and state of agglomeration,
- Concentration effects, such as hindered settling, and
- Secondary flow effects, e.g., the capture of fines in wakes generated by settling of large particles.

Due to these multifaceted interactions, attention should be given when evaluating trends between composites at a given concentration in relation to measured physical properties, such as the average particle size ((21 ± 2) µm) and solid-phase density estimates (refer to Table 23).

With respect to composite chemistry functionality observed in Figure 23, the Fe and PO_4 composites exhibited the slowest settling rates and settled to the lowest extent over the $\sim$24 h observation period. This slow settling behavior aligns with expectations derived from their observed non-Newtonian flow characteristics. Specifically, non-Newtonian behavior in solid-containing dispersions typically results from solids structuring, which—in the case of the given solid contents—forms space-filling structures that are slow to settle. This is precisely what was observed for the Fe and PO_4 composites.

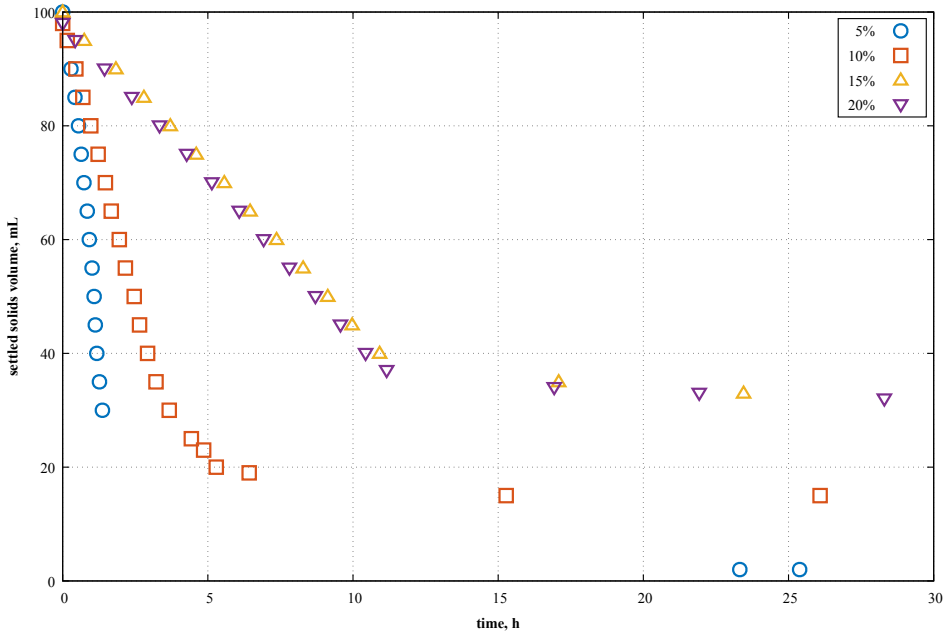


Figure 22. Measured settling curves for Al composites. Note: the similarity in 15 and 20 % UDS content settling curves is indicative of sampling biases (see Section 5.7).

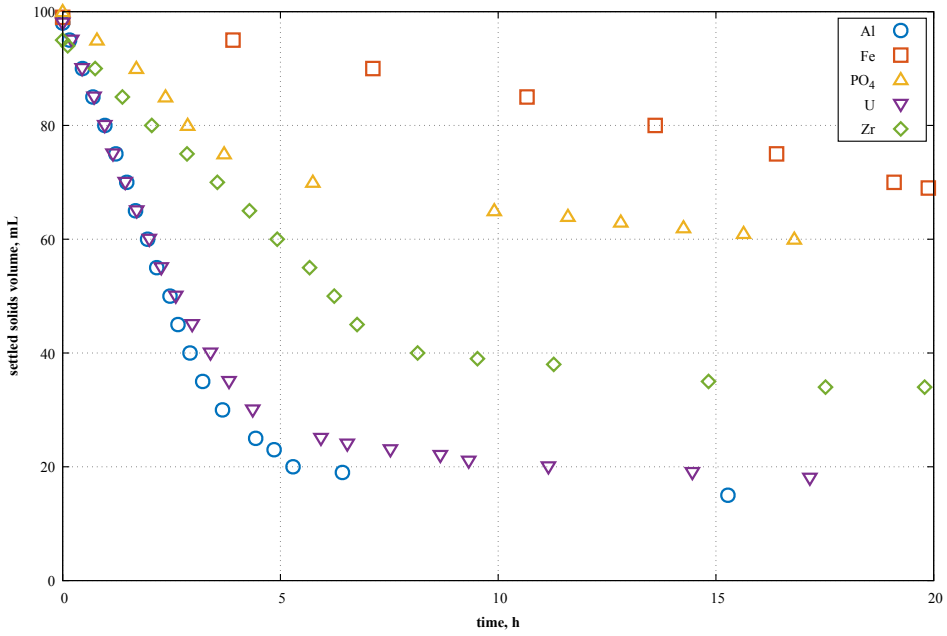


Figure 23. Measured settling curves for all nominally 10 % composites. All slurry UDS contents were approximately 10 %, except the PO_4 slurry, which was 7.3 %.

Both the Al and U composites settled relatively quickly, forming layers that occupied roughly 20 % of their original well-mixed slurry volume. Settling of the Zr composite (10 % UDS) fell between the observed settling behavior of the slow-settling Fe and PO_4 composites and the fast-settling Al and U composites. The Zr composite's settling behavior is somewhat unexpected given its estimated solid density of $\sim 4500\ kg\ m^{-3}$—the highest among all composites—but this intermediate settling behavior is associated with a 24 h settled layer volume of 34 %.

The "intermediate" settling rate observed for the Zr composite is likely a manifestation of increased hindered settling, relative to that of Al and U slurries, indicative of greater particle-particle interactions in the Zr composite. Based on the link observed between Fe and PO_4 rheology and their settling behaviors—both of which were related to particle-particle interactions and structuring—a similar but weaker correlation between Zr rheology and settling behavior might be expected given its intermediate settling behavior. This assertion appears to be supported, albeit weakly, in the Table 24 consistency values, as the Zr composite typically exhibits intermediate rheology despite the relatively dilute carrier phase in which Zr solids are suspended.

With respect to the impact of UDS on composite settling rates, visible in Figure 22, UDS strongly affects settling rates. As expected, higher UDS contents correspond to reduced settling rates—a phenomenon consistent with hindered settling.

For the Al composite example in Figure 22, the 15 and 20 % UDS composites exhibited nearly equivalent settling rates. This similarity is likely a direct result of measurement of sampling bias, as other composites tested at 20 % UDS (e.g., Zr and U) demonstrated lower settling rates at 20 % compared to 15 %. Additional confirmation of sampling bias in either or both the 15 and 20 % UDS Al composites is exhibited by the variation in their settled layer solids contents shown in Figure 26, as these contents should nominally be similar absent external factors (such as vibration or overhead pressure).

Table 26. Slurry density measurements derived from 100 mL volumetric settling flask characterization.

UDS Content,	Slurry Density for Composite, $kg\ m^{-3}$				
%	Al	Fe	PO_4	U	Zr
5.0	1220	1340	1260	1230	1080
10	1280	1470	1390	1260	1190
15	1360	1540	1450	1310	1270
20	1340	1470	1100	1310	1340

Table 27. Linear settling rate estimates for the five SE quadrant wastes as a function of UDS content. Settling rates are estimated by linear regression of the initial period of settling. Entries marked with "n/m" were not measured. All solid contents are nominal.

UDS Content,	Settling Rate for Composite, $cm\ h^{-1}$				
%	Al	Fe	PO_4	U	Zr
5.0	7.87	0.848	2.86	11.1	21.4
10	3.83	0.278	1.29	3.81	1.41
15	1.04	0.127	0.442	1.73	0.973
20	1.04	n/m	n/m	1.16	0.823

Tables 26 to 28 summarize the measured bulk composite density, linear settling rate, and percent settled solids for all composite and UDS conditions tested. Figures 24 and 25 provide graphical representations of the linear settling rate and settled solid volumes, along with their corresponding dependencies on UDS content. These figures form the primary basis for analyzing composite settling behavior.

Table 28. Percent settled solid volumes after approximately 24 h of settling as a function of composite UDS concentration. All UDS contents are nominal. Entries marked with "n/m" were not measured.

UDS Content,	Percent Settled Solids Volume for Composite, %				
%	Al	Fe	PO_4	U	Zr
5.0	30.9	23.2	25.0	8.00	5.05
10	15.3	65.7	59.8	17.3	32.6
15	33.0	89.9	83.7	30.0	53.0
20	33.3	n/m	n/m	38.0	60.1

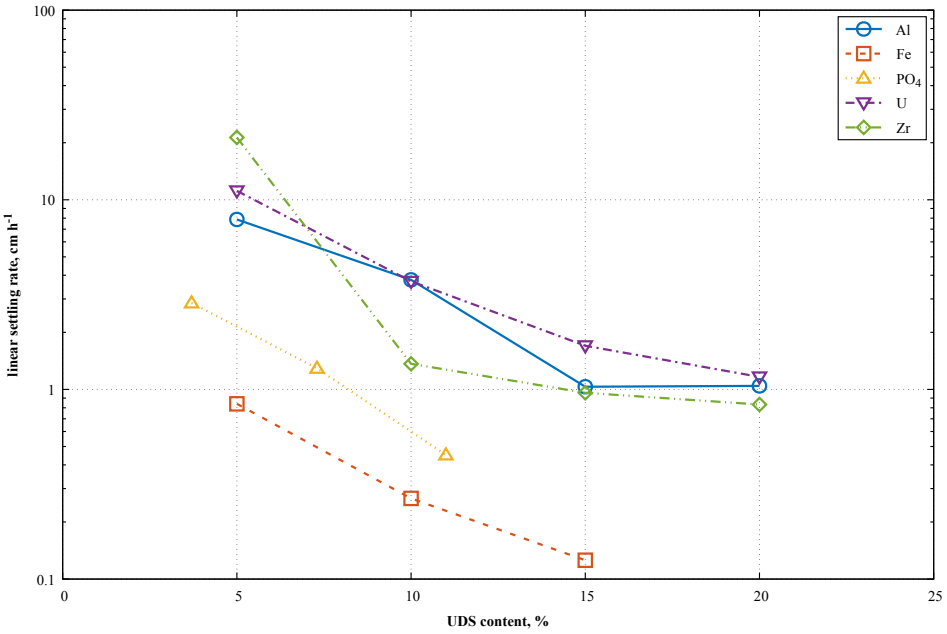


Figure 24. Measured linear settling rates for the five SE quadrant composites as a function of UDS content.

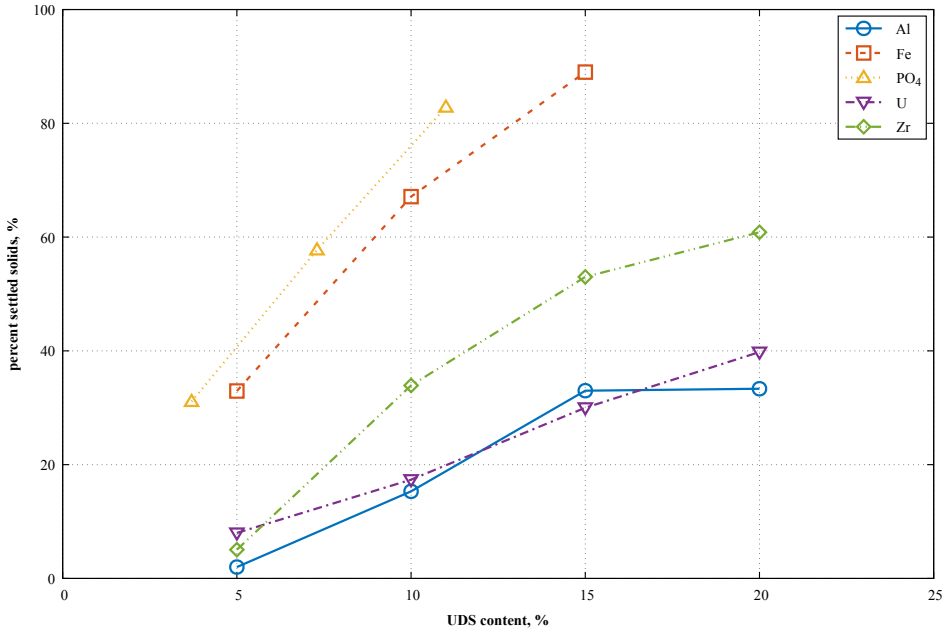


Figure 25. Measured 24 h settled solids volume percents for the five SE quadrant wastes as a function of UDS content. For composites that transition to their slow settling phase before 24 h, the settled solids volume percent is nominally equivalent to the reduced solids volume fraction $\phi/\phi_{\max}$ (see Eq. 12).

With respect to settling rates, individual composites exhibit order-of-magnitude differences that depend on the underlying chemistry. For better comparison of the impact of composite chemistry, the settling rates for the 5 % UDS condition are used as a reference point; this condition minimizes the effects of hindered settling and particle interactions (to the limited extent practicable based on the available data). Under 5 % UDS conditions:

- The Fe composite exhibits the slowest settling rate of approximately $1\,\mathrm{cm\,h^{-1}}$.
- The Zr composite exhibits the fastest settling rate at approximately $20\,\mathrm{cm\,h^{-1}}$.

Settling rates increase in the order of Fe, PO_4, Al, U, and Zr. The fact that both Fe and PO_4 remain the "slowest" settling composites is not surprising. In contrast, the 5 % Zr exhibits the highest settling rate is, at its settling rate at higher UDS contents falls between the settling rate extremes observed. This could reflect sampling error at 5 %, an assertion that is strengthened by the anomalous settled layer UDS content observed in 5 % Zr in Figure 26. However, part of the 5 % Zr composites settling behavior may reflect the real underlying changes in Zr composite chemistry due to dilution with its lower dissolved-solids supernatant, as the observed ordering of settling rates at 5 % are consistent with density based expectations as discussed in the paragraphs that follow.

Regarding the impact of UDS content, settling rates decrease with increasing solid content, as anticipated. This decrease is monotonic for all composites except Al (as discussed previously), which indicates hindered settling at the evaluated UDS concentrations.

The reasonableness of the ordering observed in the 5 % settling rates can be evaluated using terminal settling velocity estimates via Stokes' law:

$$v_t = \frac{g d_c^2}{18 \mu_l} \left(\rho_{c,s} - \rho_l \right), \tag{23}$$

where:

- v_t is the terminal velocity,
- g is gravitational acceleration,
- μ_l is the Newtonian viscosity of the suspending phase,
- $\rho_{c,s}$ and ρ_l are the densities of the composite solid and suspending phase, respectively, and
- d_c is the volume-weighted mean particle diameter, calculated as:

$$d_c = \sum_i f_i^{(\text{composite})} d_i, \tag{24}$$

where $f_i^{(\text{composite})}$ is the fractional volumetric contribution, and d_i is the characteristic diameter of component i.

It should be noted that the intent of this analysis is not to estimate expected absolute settling rates, as these will not be actualized due to hindered settling. Rather, it is to observe where measured settling rates fall relative to their terminal velocity and the composite settling rate ordering it predicts.

Table 29 provides the parameters used for calculating terminal settling velocities and the resulting estimates. Equation 23 assumes a particle Reynolds number of less than 0.1, which is satisfied for all composites in Table 29. As anticipated, calculated terminal velocities are approximately an order of magnitude greater than measured settling velocities.

Ordering composites by increasing terminal velocity, the ranking is PO_4 (slowest), Fe, Al, U, and Zr (fastest). Except for PO_4 and Fe, observed 5 % settling rates follow this order, which is encouraging given uncertainties surrounding composite size/density estimates and the influence of particle interactions (which are significant for PO_4 and Fe due to non-Newtonian rheology for these composites at higher solids loadings).

Table 29. Composite terminal settling velocity and the parameters used to estimate it. Calculations use Eq. 23 and are intended to provide an alternate assessment of how measured composite settling rates should be ordered. They are not intended as a absolute measure of settling rates. Liquid density and viscosity are measured. Solid density and diameter are inferred from PSD measurements (see Section 6.2).

Composite	Liquid Density kg m^{-3}	Liquid Viscosity mPa s	Solid Density kg m^{-3}	Diameter µm	Terminal Velocity cm h^{-1}
Al	1210	3.57	2400	21.2	29.3
Fe	1280	5.09	3100	19.0	25.4
PO_4	1250	4.22	2130	22.6	20.9
U	1200	2.76	2520	21.3	42.6
Zr	1050	1.48	4480	20.4	190

Figure 25 illustrates the variation in settled solids volume as a function of UDS content. Both PO_4 and Fe slurries exhibit the lowest extent of settling across the range of UDS concentrations evaluated. This limited settling aligns with the observed non-Newtonian behavior of these slurries, as discussed previously. The Zr composite shows intermediate settling extents, consistent with its “intermediate” settling rates and Newtonian slurry viscosity profile. In contrast, Al and U composites settle to the highest absolute extent among the evaluated slurries.

With the exception of the Al composite, all slurries exhibit the expected decrease in settled solids volume percentage with decreasing UDS content. This is consistent with the theoretical expectation of a

one-to-one correlation between UDS content and settled solids volume percentage. However, the Al composite deviates from this expectation, with most settled solids volumes falling near 30 %, except for the 10 % UDS content measurement.

A final evaluation of settled solids morphology considers the mass fraction of solids within the settled layer itself. The final (24 h) volumetric settled layer solids content, denoted as ϕ_f, is calculated by:

$$\phi_f = \frac{1}{v_{24}} \left(\frac{\rho_b^o}{\rho_{c,s}} \right) x_o, \tag{25}$$

where:

- v_{24} is the fractional extent of settling at 24 h,
- x_o is the UDS of the well-mixed composite,
- ρ_b^o is the bulk density of the well-mixed composite, and
- $\rho_{c,s}$ is the composite solid phase density.

This expression is equivalent to Eq. 13 but includes the necessary conversion of well-mixed UDS content x_o to its volume based equivalent ϕ_o. The well-mixed bulk density ρ_b^o is estimated using:

$$\rho_b^o = \left(\frac{x_o}{\rho_{c,s}} + \frac{1 - x_o}{\rho_l} \right)^{-1}, \tag{26}$$

where ρ_l is the density of the liquid phase.

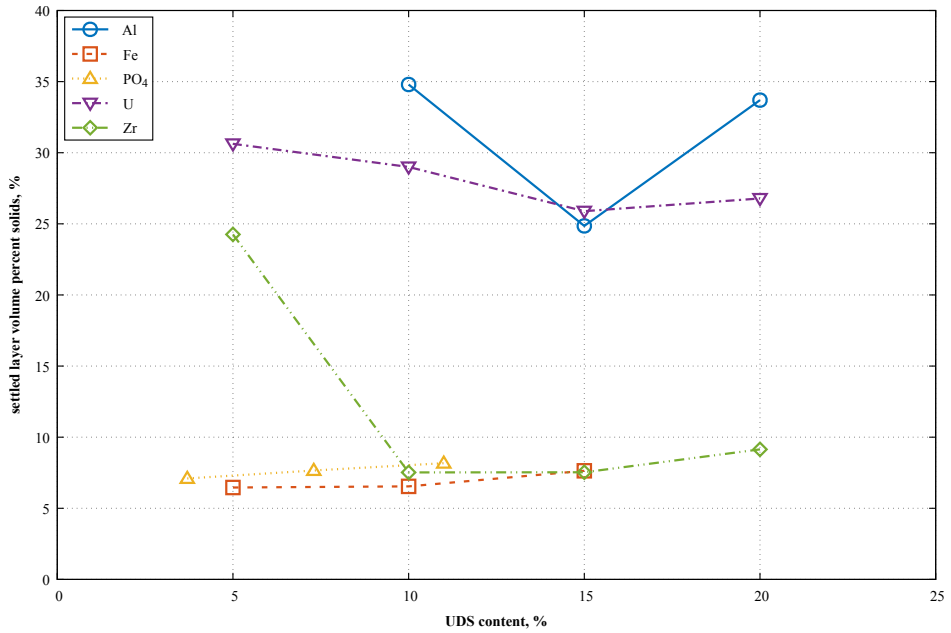


Figure 26. Volume percent of solids within the settled layer for the five SE quadrant waste composites as a function of UDS content. Measurements correspond to layers formed after 24 h of settling. Measurements are expected to be constant and independent of the UDS content of the composite. This behavior is largely observed, with some outlying points observed for the Al and Zr composites (e.g., see Zr at 5 % UDS). Deviations are likely due to the composite sampling bias discussed in Section 5.7.

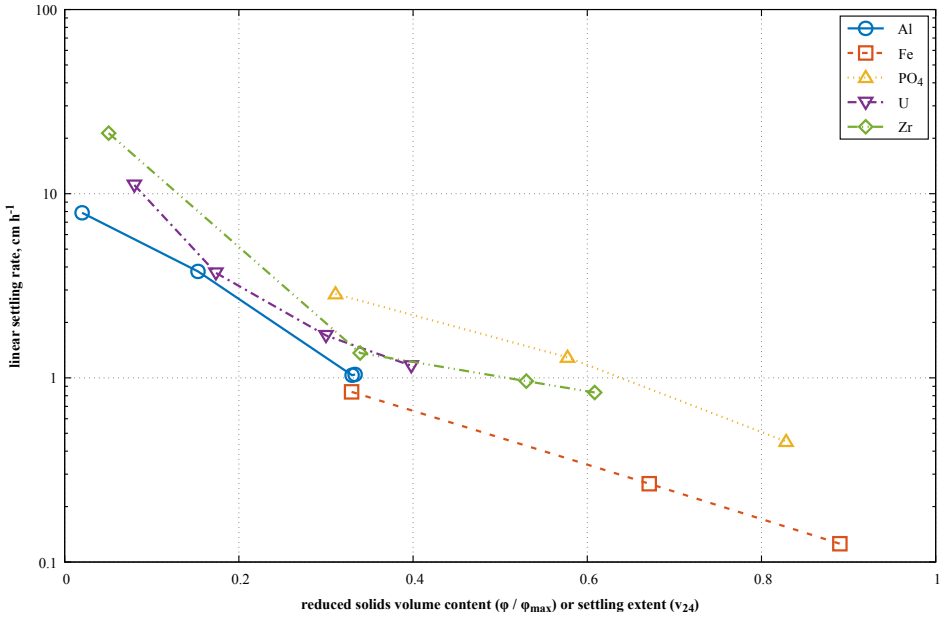


Figure 27. Measured linear settling rates as a function of the reduced volume fraction solids content of the composite (namely $\phi/\phi_{\max}$ – see Eq. 12).

Figure 26 shows the calculated settled layer volume fraction for all composite and UDS conditions evaluated in the present study. For the Fe, PO_4, and U composites, the mass fraction of solids within the settled layer remains constant across the tested UDS conditions. This outcome is largely anticipated, as the suspending phase chemistry remains nominally consistent across all composites. The deviations from this expectation observed in settled layer solid volume contents for the Al and Zr composites likely reflect sampling bias discussed in Section 5.7. While the overall height of the settled layer increases in proportion to the total quantity of solids, the concentration of solids within the layer should remain nominally constant during the compaction phase. This phase occurs after the initial period of rapid settling, as shown by settling curves like those displayed in Figure 22.

For the Al and Zr composites, the solids content within the settled layer also remains relatively constant across UDS concentrations ranging from 10 to 20 %.

Neglecting the "outlying" Al and Zr measurements at 5 % UDS, the settled solids volume fractions naturally group into two distinct "levels." The first group comprises the Al and U composites, which exhibit settled solids volume fractions of approximately 30 %. In plain terms, Al and U composites settle rapidly and form dense, solids-rich layers.

The second group includes the Fe, PO_4, and Zr composites, which exhibit settled solids volume fractions near 7 %. For the Fe and PO_4 composites, settling is slow and results in "fluffy," solids-lean layers. This behavior is consistent with previous discussions regarding the space-filling structures formed by solids in these composite chemistries, which give rise to non-Newtonian behavior.

The settling behavior for Zr, however, does not fit neatly into either of the two classifications described above. The Zr composite appears to settle into a loose layer but does not exhibit the non-Newtonian rheology observed for Fe and PO_4. Instead, its settling rates are more akin to those observed for the Al and U composites. At 5 % UDS, where Zr is the fastest settling composite, its corresponding settled solids volume fraction of 25 % is more closely aligned with Al and U behavior.

It is worth noting that the preparation of the Zr composite deviated from initial plans, with 20 % UDS measurements indicating substantially more dissolved solids than expected. Subsequent dilution using as-prepared Zr supernatant naturally reduced the dissolved solids content of the suspending phase as UDS was adjusted. This variation in dissolved solids chemistry may have contributed to the "bivalent" behavior observed in the Zr composite's settling characteristics.

The final settling figure, Figure 27 shows the linear settling rates as a function of the reduced solid volume content of the slurry. Here, the reduced volume concentration is representative of ϕ/ϕ_{max}, where ϕ_{max} is maximum settled solids volume of the composite of the composite Use of reduced solids contents collapses the settling behaviors largely within an order of magnitude settling rate band. While use of reduced concentrations does not completely eliminate composite-to-composite variation in settling rate, it appears to greatly unify the observed settling behaviors and suggests a potential set of bounding curves for SE quadrant waste settling rates. Development of such curves falls within the scope of planned out-year activities.

6.6 NJS

The NJS (Just-Suspended Speed) for the five SE quadrant composites has been measured and reported in (Bachman et al., 2025). Table 30 summarizes these measurements alongside NJS predictions based on the physical properties listed in Table 29 and the known dimensions of the small-scale NJS cell.

Estimated NJS values were calculated using the Zwietering correlation (Zwietering, 1958), which is given by:

$$\text{NJS} = S\, v^{0.1} \left(g\,(s-1) \right)^{0.45} X^{0.13}\, d_c^{0.2}\, D_i^{-0.85}, \tag{27}$$

where:

- S is the Zwietering parameter, unique to the mixing impeller and tank geometry (including considerations such as impeller clearance from the vessel bottom and the presence of baffles),
- g is the gravitational acceleration,
- $s = (\rho_{c,s}/\rho_l) - 1$ is the relative density,
- v is the kinematic viscosity,
- X is the mass ratio of suspended solids to liquid (multiplied by 100),
- d_c is the volume-weighted mean particle diameter (calculated using Eq. 24), and
- D_i is the overhead mixing impeller diameter.

For the present study, the Zwietering coefficient was estimated as $S = 3.97$ using NJS measurements of spherical 70 µm glass beads (identified as S1-D2 beads) also reported in (Bachman et al., 2025).

Figure 28 provides a parity plot comparing estimated and measured NJS values for each composite. Measured NJS values ranged from 570 to 1210 RPM and demonstrated strong dependence on composite chemistry. Each composite exhibited a largely unique NJS, except for the 850 RPM values observed for both PO_4 and Zr composites. As noted in (Bachman et al., 2025), the Fe composite exhibited the highest measured NJS, at 1210 RPM, making it the most challenging composite to resuspend through overhead mixing due to its higher energy requirements.

As shown in Figure 28, both PO_4 and Fe composites exhibit measured NJS values significantly higher than their predicted values based on the Zwietering correlation. While this discrepancy could suggest poor

quantification of the parameters used in estimating NJS, it is more likely a result of the non-Newtonian flow properties exhibited by these two slurries. Similar deviations above parity have been observed for fine, cohesive gibbsite tank waste simulants in Daniel et al. (2025).

In contrast, the Al, U, and Zr composites—which exhibited Newtonian flow behavior—fall largely along the NJS parity line, within the expected accuracy of the Zwietering correlation (±20 %). This indicates that measured composite NJS behaves in line with expectations based on size and density properties for systems where composites exhibit Newtonian behavior, i.e., no significant solid structuring. Composites that exhibit non-Newtonian behavior when fully mixed, however, show NJS values substantially larger than those predicted by the Zwietering correlation (approximately 80 % larger for this study).

Table 30. Comparison of measured and estimated NJS for the five SE quadrant wastes. Estimates of NJS employ the composite properties listed in Table 29 and Eq. 27.

Composite	NJS, RPM	
	Est.	**Meas.**
Al	526	570
Fe	628	1210
PO_4	444	830
U	542	670
Zr	834	870

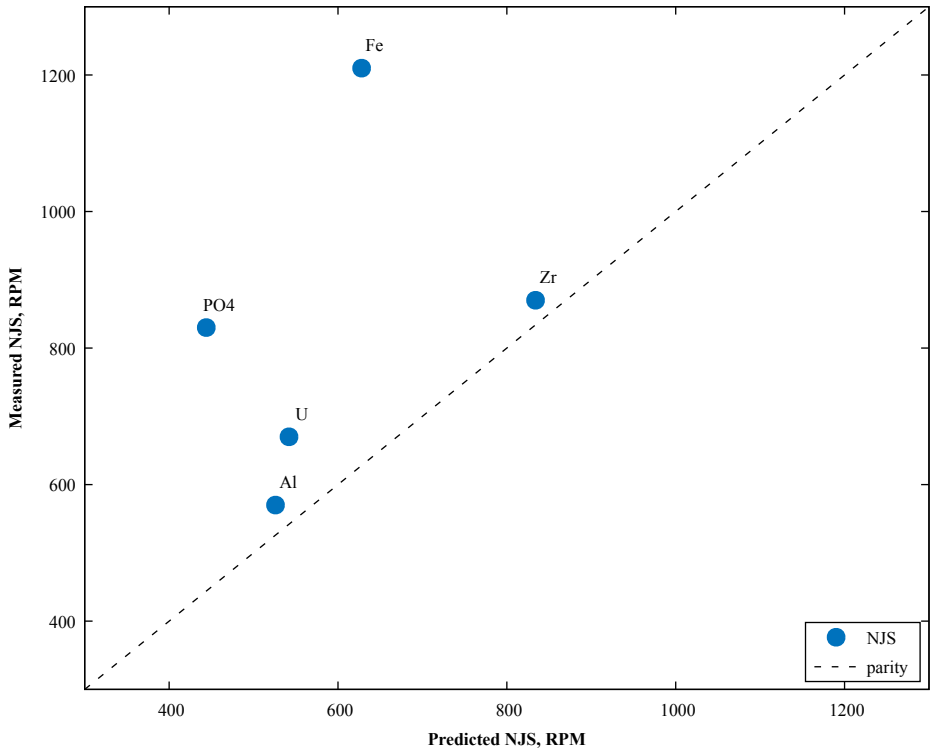


Figure 28. Parity plot comparing measured and predicted NJS values for the SE quadrant composites. Measured values deviate significantly from predictions for non-Newtonian slurries (e.g., PO_4 and Fe composites), while Newtonian slurries fall within the expected parity range.

The primary takeaway from the NJS results and comparison is that composite NJS is a complex function of both physical waste properties and underlying particle-particle interactions. The disparity between predicted and measured NJS for the PO_4 and Fe composites highlights the challenges of anticipating difficult waste chemistries solely based on solid and liquid phase densities and viscosities.

While it could be argued that composite non-Newtonian character might serve as a metric for identifying challenging composites, the cohesive strength observed in the Fe and PO_4 composites is relatively weak, with neither composite showing notable shear strength compared to the other materials. Newtonian composites, such as Al and U, exhibit large shear strengths (reported in Table 25) likely due to granular contact friction. Granular friction may explain the disparity between NJS and shear strength for these materials.

For non-Newtonian composites such as Fe and PO_4, the relatively weak cohesive strength (e.g., 30 Pa) of settled layers may play a larger role in resisting the erosion of solids from the surface of a bed during NJS testing, compared with granular interactions in Newtonian systems. This demonstrates that shear strength alone is not a definitive metric for assessing NJS values, as the mechanisms driving erosion during mixing differ significantly depending on composite properties.

The complexities outlined above reinforce the need for direct measurement of Hanford waste solid NJS using the "miniaturized" NJS capability described in Bachman et al. (2025). Direct measurement avoids relying on correlations that must account for the confluence of resuspension properties such as waste solid particle size, density distribution, and flow behavior.

7.0 Conclusions

The present study aimed to establish a baseline set of as-measured transport properties to support the direct feed treatment of Hanford HLW. To achieve this, year-one activities focused on two primary objectives: 1) identifying, obtaining, and preparing relevant samples of Hanford tank wastes for transport property evaluation, and 2) quantifying the "as-received" rheology and transport properties of those wastes. In the subsections below, the activities and findings that contributed to the fulfillment of these objectives are discussed in detail.

7.1 Waste Selection and Receipt

A review of available Hanford waste samples identified twenty-three centrifuged solid waste core segments originating from Hanford tanks AN-101, AN-106, and AW-105. These waste samples were obtained from tanks in Hanford's southeast quadrant and were selected, in part, due to the prevalence of PUREX cladding wastes within the southeast complex. PUREX cladding wastes have previously been shown to exhibit challenging waste rheology and settling behaviors (Snow et al., 2009). They serve as ideal candidates for this study, as their transport properties provide valuable insights for the design of similarly challenging waste simulants that could be used in bench- and pilot-scale evaluations of waste transport.

The twenty-three waste samples were procured and shipped to PNNL with the assistance of H2C and HLMI. Upon receipt, the samples were individually inspected and imaged (a complete itemization of sample images is provided in A of this report). The as-received samples primarily consisted of dried solids ranging from free-flowing powders to container-spanning dried "pucks" of settled waste solids. A small number of sample jars retained inherent moisture; however, most samples had dried during interim storage at the 222-S laboratory.

7.2 Waste Compositing

Preliminary evaluations of waste sample chemistry utilized existing analytical data reported by Jordan (2022a,b) and Disselkamp (2009), as well as core segment mass estimates provided by the 222-S laboratory. No single core segment contained a sufficient solids inventory to enable meaningful transport characterization. Therefore, a compositing strategy was developed in which twenty-one core segments would be selectively combined to form five waste composites. Chemical data from the core segments were used to strategically group them with the goal of creating composites enriched in five target analyte chemistries: aluminum, iron, natrophosphate, uranium, and zirconium. Compositing was performed using a two-stage approach to account for the presence of dried soluble solids. During the first stage, simulated supernatant was added to slurry the dried solids to a target of 25 % UDS content. Next, a second-stage adjustment was applied to correct both the dissolved and undissolved solids content, accommodating for the loss of solids due to dissolution and achieving the desired balance in dissolved solids content. Stage 2 adjustments targeted an initial composite UDS of 20 % as a baseline for physical property and transport characterizations. Serial dilution of these 20 % composites with additional simulated supernatant facilitated further rheology and transport testing at 15, 10, and 5 % UDS.

Execution of the compositing strategy proceeded largely as planned. First, waste solids were carefully recovered from their parent core segment jars, which were originally used to ship the waste samples. Approximately 80 % of the solids inventory was recovered based on the 222-S mass estimates. Five simulated waste supernatants, with chemistries designed to match those expected for Al, Fe, PO_4, U, and Zr liquids (based on existing centrifuged liquid analytical data), were prepared to re-slurry the composite solids. Upon completing Stage 1 dilution, all combined composite solids demonstrated some degree of

dissolution, as evidenced by an increase in dissolved solids within the supernatant used to re-slurry the solids. Generally, the increases in dissolved solids content were moderate (∼20 %); however, the Zr composite supernatant exhibited dissolved solids nearly four times higher than expected, suggesting significant dissolution of Zr solids. Regarding the undissolved solids, three of the five composites achieved UDS values near the Stage 1 target of 25 %, while the Fe and PO_4 composites fell short at approximately 17 %. Despite the notable dissolution observed in the Zr composite supernatant, its UDS achieved 26.6 %, close to the Stage 1 target. Overall, interpretation of Stage 1 results was complicated by uncertainties in the original moisture content of the as-received solids, lower-than-expected solid recovery, and challenges associated with unbiased sampling in the shielded radiological facility where the composites were prepared.

Stage 2 adjustments successfully modified the Al, Fe, U, and Zr composites to achieve their target UDS content of 20 %. Adjustment of the PO_4 composite was bypassed due to its limited inventory; Stage 2 adjustments would have necessitated significant removal of composite supernatant to increase UDS content, leaving insufficient composite mass below 200 g. Given that NJS testing requires a minimum of 150 mL of composite, further adjustments—coupled with loss due to analytical and rheological characterizations—would have rendered the final inventory of the adjusted PO_4 composite insufficient for testing. As a result, the PO_4 composite was adjusted solely to correct the supernatant dissolved solids content, leading to a final UDS of 14.6 %. Subsequent serial dilutions followed the original plan, resulting in composite concentrations of 11.0, 7.3, and 3.6 % UDS.

A second deviation in Stage 2 adjustments involved the Zr composite dissolved solids content. As previously noted, Stage 1 Zr dilutions yielded a dissolved solids content of 22.4 %, which significantly exceeded the expected 6.60 % based on analytical data provided in Disselkamp (2009). Correcting this disparity would have required substantial dilution of the composite with water, followed by settling and decanting to remove excess liquid. This adjustment was omitted to avoid handling the large ∼1 L volume of diluted composite required to make the change.

Table 31. Summary of measured (actual) composite solid and liquid phase chemistry. This table is a reproduction of Table 21 in Section 6.

Analyte	Concentration for Composite				
	Al	**Fe**	**PO_4**	**U**	**Zr**
			Solids, mg g^{-1}		
Al	418	115	80.6	201	25.2
Cr	0.685	2.89	2.57	0.344	13.1
Fe	48.7	142	48.6	84.6	32.2
Na	142	232	305	214	358
PO_4	27.4	1.87	161	98.9	6.49
U	36.7	23.5	87.9	173	67.3
Zr	0.0634	18.3	0.0155	0.005 36	229
			Supernatant, M		
Al	0.232	0.279	0.215	0.0837	0.006 31
Cl	0.0562	0.112	0.0955	0.0589	0.007 41
F	0.112	0.0504	0.124	0.121	0.171
OH	1.25	1.04	0.956	0.504	0.254
NO_3	0.881	1.63	1.48	0.956	0.394
NO_2	1.11	1.64	1.48	1.15	0.0595
PO_4	0.0241	0.0357	0.0205	0.0364	0.003 86
Na	4.88	6.49	5.76	4.56	1.13
SO_4	0.0431	0.0380	0.0464	0.0366	0.004 55
CO_3	0.543	0.780	0.622	0.750	0.11

Table 31 summarizes the prepared composite chemistries. This table reproduces an earlier version presented in Section 6. The as-prepared composite chemistries were generally consistent with expectations based on data from Jordan (2022a,b) and Disselkamp (2009). Specifically, the Al composite was rich in aluminum-bearing solids, the Fe composite contained abundant iron-bearing solids, and so forth. The primary discrepancy involved the relative quantities of Na and PO_4. Preliminary estimates suggested that the waste core segments would be sodium-lean, with a Na-to-PO_4 molar ratio below that anticipated for natrophosphate ($Na_7(PO_4)_2F \cdot 19\,H_2O$). However, the as-prepared composites were sodium-rich, exhibiting Na-to-PO_4 ratios well above those expected for natrophosphate. Mass fractions of Na in the actual waste samples were considerably higher than anticipated, while mass fractions of PO_4 were correspondingly lower, such that the sum of Na and PO_4 mass fractions generally matched between measured and expected compositions. The Fe composite, in particular, showed no detectable phosphate inventory. While the precise cause of this discrepancy could not be determined, it likely stems from differences in sample handling and analysis methodologies between this study and the sources of the analytical data used for compositional estimates.

7.3 Physical Property and Transport Testing

Physical property and transport testing were conducted on select samples of the originating waste solids, as well as on all or a limited subset of composite concentrations, depending on the property being studied. Composite chemistry, as discussed in the previous subsection, was quantified to ensure that the as-prepared composite chemistries aligned with expectations. Select samples of AN-101, AN-106, and AW-105 solids were analyzed prior to compositing, with microscopic imaging used to assess particle size and mineral phase distribution within the wastes. These analyses, originally reported in Buck et al. (2025), facilitated estimates of the volume-based particle size distribution by correlating waste analytes of interest with specific mineral phases described in Buck et al. (2025). Flow behavior and settling rates/extent of the composites, as a function of UDS content, were characterized using a combination of concentric cylinder viscometer and graduated cylinder settling tests. Settling experiments were monitored over a minimum duration of 24 h. With the exception of measurements for slow Fe and PO_4 settling behaviors at 20 % UDS and supernatant-like viscosities for a select number of low-weight percent composites, settling and flow behaviors were observed across the full range of composite-UDS combinations. Additionally, the shear strength and NJS of settled solid layers were tested to estimate settled layer strength and resuspension tendencies. Shear strength measurements were performed on sludge settled for 165 h, whereas NJS measurements evaluated sludge settled for 24 h. Aside from the characterization of composite chemistry, which was previously discussed, the general findings from these physical property and transport investigations are summarized in the following paragraphs.

Particle Size Distribution and Solids Phase Density: The PSD for the five composites was estimated by utilizing component-based PSDs for the waste samples previously characterized in (Buck et al., 2025). Specifically, Buck et al. (2025) measured the size distributions of select mineral phases present in the AN-101, AN-106, and AW-105 solids utilized in the current study. The phase specification was sufficiently detailed to allow association of select phases with analytes of interest (e.g., Al, Fe, PO_4, etc.) and the derivation of composite PSDs from the measured composite chemistry. The mineral phases associated with each analyte were as follows:

- Al – gibbsite,
- Fe – hematite,
- PO_4 – natrophosphate,
- U – clarkeite, and

- Zr – zirconium dioxide (zirconia).

The resulting composite PSDs revealed minimal differentiation between composites; that is, all composites exhibited nearly identical PSDs. Observable differences were primarily in the fractional contributions of <10 µm particles, though these differences may partially result from noise introduced during the conversion of size distributions from the original number distributions reported in Buck et al. (2025) to the volume distributions required for engineering models used to interpret composite settling rates and NJS. Overall, the volume-weighted mean diameters of the composites were approximately (21 ± 2) µm. The Fe composite exhibited the smallest mean size, while the PO_4 composite also displayed a comparatively small mean size. Thus, the settling behavior of the composites is expected to be predominantly influenced by their composite density. Composite densities were estimated using the same phase association approach used to derive PSDs, whereby a bulk solids density was calculated based on the expected mineral phase density and composite chemistry. The results indicated broader variability in density, with the PO_4 composite exhibiting the lowest density at $2130\,\mathrm{kg\,m^{-3}}$, and the Zr composite—as anticipated—exhibiting the highest density at $4480\,\mathrm{kg\,m^{-3}}$. It is important to note that these densities were derived directly from the as-prepared compositions. They may not necessarily align with expectations based solely on analyte composition, as the final mixed density depends strongly on the assumed mineral form, its density, and the composite-specific analyte chemistry. For instance, while clarkeite possesses the highest mineral phase density at $6390\,\mathrm{kg\,m^{-3}}$, the U composite exhibited an intermediate density of $2520\,\mathrm{kg\,m^{-3}}$.

Composite Rheology and Shear Strength: The flow behaviors of the composites were characterized using concentric cylinder viscometry as a function of their UDS content. The Fe and PO_4 composites demonstrated non-Newtonian, Bingham plastic flow behavior, whereas the Al, U, and Zr composites exhibited Newtonian flow behavior. Non-Newtonian behavior in the Fe composite persisted up to a UDS content of 15 %, while the PO_4 composite maintained non-Newtonian behavior up to 7.3 %. The observed non-Newtonian characteristics of the Fe and PO_4 slurries suggest notable structuring and interactions among dispersed solids, leading to the formation of space-filling structures. Such structures are typically associated with slow-settling slurries, as evidenced by the slow settling rates observed for the Fe and PO_4 composites (discussed in detail in subsequent pages). The maximum yield stress required to maintain flow was measured at 2.1 Pa for the Fe composite and 5.7 Pa for the PO_4 composite. For the Al and U composites, rheological measurements indicated behavior similar to their corresponding carrier fluids, suggesting limited structuring and interactions among solids within these composites. In contrast to the Fe and PO_4 composites, both the Al and U composite solids settled rapidly. Overall, the yield stresses and viscosities observed for the five SE quadrant composites were consistent with expected values for their UDS contents, as reported in (Wells et al., 2011). The variation in composite yield stress and viscosity with UDS content followed a typical power-law trend, demonstrating differentiation between non-Newtonian and Newtonian SE quadrant wastes, which could prove significant in designing physical simulants tailored to SE quadrant waste rheology.

Many of the composites contained appreciable aluminum (Al) content. Previous studies of Al-rich wastes, including those by Snow et al. (2009), reported significant shear strengths ranging from 100 to 1000 Pa. Shear strength, a measure of the force required to initiate flow within a settled bed of solids, is analogous to the yield stress of a non-Newtonian fluid under static conditions. Shear strengths of the five SE quadrant wastes were measured using vane tool geometry, which found limited material strength in at least three of the five composites. Preliminary measurements revealed shear strengths of less than 50 Pa at the standard test depth for all composites. Strength measurements at deeper vane tool immersion depths generally showed higher values, but only a single measurement (for the U composite) exceeded 60 Pa, reaching 1600 Pa at the greatest immersion depth allowed. This elevated shear strength was comparable to the results reported in Snow et al. (2009), although the measurement depth placed the vane tool almost in contact with the vessel floor. Repeat shear strength measurements for the Al and U composites under controlled conditions revealed increased strengths, with $\sim$100 Pa for the Al composite and $\sim$500 Pa for the

U composite. These repeat measurements likely benefited from careful transfer of all available dense solids from the parent composite volume into the shear strength test container. For the U composite, the elevated repeat measurement suggests the presence of dense granular material contributing to settled sludge strengths ranging between 500 and 1000 Pa. Similarly, the total inventory of Al composite solids exhibited increased shear strengths; however, at 100 Pa, these values remain on the low end of previously reported strengths.

Settling Volume, Rates, and Density: Composite settling behavior was generally characterized by two stages: an initial period of rapid settling, followed by a final slow compaction stage. As anticipated, the settling behavior observed was dependent on both composite chemistry and UDS content. Settling rate characterization focused on the initial rapid settling period and reported rates ranging from 0.1 to 30 $cm\,h^{-1}$. The observed settling rates indicated hindered settling, with rates decreasing as the solids content increased. The Fe and PO_4 composites exhibited slower settling and lower levels of compaction compared to the other three composites. This behavior was expected, given the non-Newtonian rheology observed for the Fe and PO_4 composites, suggesting significant underlying particle-particle interactions, which reduced both settling rates and compaction of solids. In contrast, the Al and U composite solids demonstrated relatively fast settling and dense final compaction. The Zr composite solids generally settled at rates comparable to Al and U; however, they settled more slowly at intermediate UDS concentrations and packed more loosely. The differences between Zr settling behavior and that of Al and U may be attributed to changes in carrier fluid properties during dilution, as the Zr composite was found to have substantially higher dissolved solids content than anticipated during preparation. Dilution with the as-prepared Zr supernatant gradually reduced the dissolved solids content toward expected values as the UDS reached 5 %. This convergence was supported by the settling data, with the Zr composite exhibiting the largest observed settling rate at 5 % UDS and reaching a final density similar to that of the Al and U composites.

To evaluate the reasonableness of the observed settling rates, the 5 % UDS settling rates were compared to rates predicted by Stokes' settling law. The 5 % UDS condition was selected as it represents the settling scenario with the least amount of hindrance. The intent of this comparison was to assess the ordering of composite settling rates rather than to compare absolute rates. The comparison revealed that the measured settling rate order at 5 % UDS (Fe, PO_4, Al, U, and Zr) was largely consistent with the order predicted by Stokes' settling law (PO_4, Fe, Al, U, and Zr), with the only discrepancy being the swapping of Fe and PO_4. Regarding the inability of Stokes' model to fully capture Fe and PO_4 settling rates, this discrepancy is reasonable given the model's limitations in systems exhibiting significant particle-particle interactions, such as those observed in the Fe and PO_4 composites.

Settling evaluations also examined the density of solids packing in the settled layers. Consistent with the observed settling rates, the composites fell into two distinct categories: the Fe, PO_4, and Zr composites packed loosely, while the Al and U composites packed densely. Except for variations in Al and Zr behavior at 5 % UDS, the volume fraction of solids in the settled layers remained consistent and did not vary with UDS content.

NJS: Composite NJS (just-suspended mixing speed) was characterized and reported in Bachman et al. (2025). All five SE quadrant composites were allowed to settle for 24 h before being resuspended using an overhead mixer to quantify the mixing rate required to fully clear the settled solids (i.e., the NJS). Contrary to the settling and shear strength behavior, NJS mobilization testing found the Fe composite to be the most challenging to resuspend and the Al composite to be the easiest. To aid in interpreting these results, the NJS predicted by the Zwietering correlation was estimated for each composite using density and particle size information derived in the present study. A parity plot comparing the predicted and measured NJS values showed reasonable, if not strong, agreement for the Al, U, and Zr composites. However, significant positive deviations from parity were observed for both the PO_4 and Fe composites. The disparity in NJS

behavior appears to correlate with each composite's flow characteristics: Newtonian versus non-Newtonian. More specifically, the disparity is tied to non-Newtonian behavior. This is expected, as the Zwietering correlation is designed primarily for granular solids and may not account for the hydrodynamics and yield stresses inherent to non-Newtonian slurries compared to Newtonian fluids. Additionally, the differences extend beyond the limitations of the correlation itself, as the hydrodynamics of non-Newtonian flow are fundamentally distinct from Newtonian systems due to the presence of a yield stress and the associated minimum force required to initiate flow.

Furthermore, the nature of particle-particle interactions in the Fe and PO_4 composites is likely different from those in the Al, U, and Zr composites, given that the former exhibit non-Newtonian behavior when mixed, while the latter remain Newtonian. These differences are expected to significantly influence the response of settled composite layers to mobilization forces. It can be hypothesized that:

- Cohesive composites may exhibit relatively low shear strength due to inter-particle cohesion compared to granular composites, where frictional interactions demand greater forces to slide individual granules against one another.
- However, the cohesive nature of settled layers may more effectively stabilize against lift forces generated by overhead mixing compared to granular systems, where individual particles are gradually eroded away by lift forces.

In simpler terms, granular systems may be easier to mobilize through lift forces that incrementally displace individual particles, whereas cohesive systems require gross material failure for effective mobilization.

7.4 Key Takeaways and Next Steps

The experimental results discussed above outline behaviors that appear to be largely classified based on bulk composite rheology. Table 32 provides a curated summary of the observed properties, encapsulating the overall behaviors of the studied composites. The two non-Newtonian composite chemistries (Fe and PO_4) exhibited slow settling rates and reduced mobilization proclivity compared to their Newtonian counterparts (Al, U, and Zr). This behavior reflects Fe- and PO_4-specific particle chemistries and sizes that promote the formation low density, space-filling structures with packing fractions on the order of 10 % by volume. These structures limit solids compaction, lead to emergent non-Newtonian rheology, appear to stabilize settled beds against gradual erosion by overhead mixing, and limit overall settled bed strength in shear to $\sim$50 Pa or less. The confluence of observed behaviors for the Fe and PO_4 composites are likely to render SE quadrant wastes rich in iron and phosphate susceptible to mixing challenges at receipt UDS contents of 15 % by mass or greater. Additional consideration of waste receipt and mixing strategies may be necessary when processing iron- and/or phosphate-rich wastes within WTP.

Although the broad Newtonian / non-Newtonian classification simplifies the nuanced spectrum of physical and transport results measured, it offers a robust and logical framework for categorizing observed composite transport behaviors. The findings from this study establish a foundational framework for evaluating the transport properties of SE quadrant waste materials. To build upon this work, next steps should focus on investigating the effects of waste blending and the addition of glass-forming chemicals. Regarding waste blending, the results suggest that non-Newtonian behavior could potentially be mitigated by blending, thereby reducing both mobilization and pumping requirements. However, this strategy may present conflicts with design and process requirements that necessitate the retention of slowly settling materials. Ultimately, the overarching goal of transport property measurement and characterization is to develop predictive models that support the "design" and control of waste transport properties during HLW facility operations at the WTP. The findings of this study provide the initial classifications necessary for developing such models. Nevertheless, further work is required to establish first-order models for predicting settling rates based on composition and estimating NJS for non-Newtonian slurries.

Planned year-two activities within the present program aim to generate the necessary data to further refine and define an SE quadrant waste model framework. These efforts are expected to advance the development of models that will facilitate improved waste transport management during facility operations.

Table 32. High-level summary of SE waste exemplar transport properties. Flow behavior is Newtonian (N) or non-Newtonian Bingham Plastic (BP). All UDS solid contents listed are nominal. The 5 % settling rates have been included as representing measurements of settling behavior; however, the 5 % Zr composite rate of 21.4 cm h^{-1} is faster than anticipated based on measurements at increased UDS and may be a result of sampling bias.

Parameter	**Composite**				
	Al	Fe	PO_4	U	Zr
Flow Behavior (@20 % UDS)	N	BP	BP	N	N
Yield Stress, Pa	– –	2.1	5.7	– –	– –
Consistency/Viscosity, mPa s	5.0	24.9	21.2	5.1	7.5
Standard Shear Strength, Pa	85	21	24	42	40
Maximum Shear Strength, Pa	126	28	45	1600	55
Settling Behavior	Fast	Slow	Slow	Fast	Mixed
Settling Rate (@5 % UDS), cm h^{-1}	7.87	0.848	2.86	11.1	21.4
Settling Extent (@5 % UDS), %	30.9	23.2	25.0	8.00	5.05
Settled Layer Content (ϕ_{max}), % volume	31	6.9	7.6	28	12
Measured NJS (@20 % UDS), RPM	570	1210	830	670	870

8.0 References

24590-HLW-MVC-HFP-00001. 2021. *Process Information for HFP Vessels (HFP-VSL-00001, HFP-VSL-00002, HFP-VSL-00005, and HFP-VSL-00006)*. 24590-HLW-MVC-HFP-00001, Rev. 3, Bechtel National, Inc., Richland, Washington.

Bachman A, A Westesen, R Daniel, C Burns, E Buck, , and R Peterson.. 2025. *FY25 Task 5: Small-Scale Mixing*. PNNL-38358, Pacific Northwest National Laboratory, Richland, Washington.

Barney GS. 1976. *Vapor-Liquid-Solid Phase Equilibria of Radioactive Sodium Salt Wastes at Hanford*. ARH-ST-133, Atlantic Richfield Hanford Company, Richland, Washington.

Bredt P, B Arey, E Buck, E Jenson, B McNamara, A Poloski, and R Swoboda. 2003. *Rheological and Physical Properties of AP-101 LAW Pretreated Waste and Melter Feed*. PNWD-3279 (WTP-RPT-064, Rev. 0), Battelle—Pacific Northwest Division, Richland, Washington.

Bredt P and R Swoboda. 2000. *Rheological Studies on Pretreated Feed and Melter Feed from AW-101 and AN-107*. PNWD-3034 (BNFL-RPT-034, Rev. 0), Battelle—Pacific Northwest Division, Richland, Washington.

Buck EC, AA Bachman, J Eshun, and RA Peterson. 2025. *Automated Particle Analysis of Hanford Tank Wastes 241-AN-106, 241- AN-101, and 241-AW-105*. PNNL-37622, Pacific Northwest National Laboratory, Richland, WA.

Burns CA, RC Daniel, CW Enderlin, M Luna, and AJ Schmidt. 2009. *Shear Strength Measurement Benchmarking Tests for K Basin Sludge Simulants*. PNNL-18479, Rev. 0, Pacific Northwest National Laboratory, Richland, Washington.

Daniel RC, CA Burns, MSR Chowdhury, P Huynh, and RA Peterson. 2025. *Blending as an In-Tank Waste Processing Strategy*. PNNL-37669 (ITSW-RPT-003, Rev. 0), Pacific Northwest National Laboratory, Richland, Washington.

Daniel RC, RA Peterson, BE Westman, and CA Burns. 2022. "Impact of dilution-induced precipitates on the filtration of Hanford liquid tank wastes." *Separation Science and Technology* 54(16):2635–2651.

Disselkamp RS. 2009. *2009 Auto-TCR for Tank 241-AW-105*. RPP-RPT-42913, Rev. 0, Washington River Protection Solutions, Richland, Washington.

Edwards M, J Billing, D Blanchard, E Buck, A Casella, A Casella, J Crum, R Daniel, K Draper, S Fiskum, L Jagoda, E Jenson, A Kozelisky, P MacFarlan, R Peterson, R Shimskey, L Snow, and R Swoboda. 2009. *Characterization, Leaching, and Filtration Testing for Tributyl Phosphate (TBP, Group 7) Actual Waste Sample Composites*. PNNL-18119 (WTP-RPT-169, Rev. 0), Pacific Northwest National Laboratory, Richland, Washington.

Fiskum S, E Buck, R Daniel, K Draper, M Edwards, T Hubler, L Jagoda, E Jenson, A Kozelisky, G Lumetta, P MacFarlan, B McNamara, R Peterson, S Sinkov, L Snow, and R Swoboda. 2008. *Characterization and Leach Testing for REDOX Sludge and S-Saltcake Actual Waste Sample Composites*. PNNL-17368 (WTP-RPT-157, Rev. 0), Pacific Northwest National Laboratory, Richland, Washington.

Fiskum SK, JM Billing, EC Buck, RC Daniel, KE Draper, MK Edwards, ED Jenson, AE Kozelisky, PJ MacFarlan, RA Peterson, RW Shimskey, and LA Snow. 2009a. *Laboratory Demonstration of the Pretreatment Process with Caustic and Oxidative Leaching Using Actual Hanford Tank Waste*. PNNL-18007, Rev. 0, Pacific Northwest National Laboratory, Richland, Washington.

Fiskum SK, JM Billing, JV Crum, RC Daniel, MK Edwards, RW Shimskey, RA Peterson, PJ MacFarlan, EC Buck, KE Draper, and AE Kozelisky. 2009b. *Characterization, Leaching, and Filtrations Testing of Ferrocyanide Tank sludge (Group 8) Actual Waste Composite*. PNNL-18120, Rev. 0, Pacific Northwest National Laboratory, Richland, Washington.

Jordan EL. 2022a. *Final Analytical Report for Tank 241-AN-101 Core 2021-05 Tank Sampling and Analysis*. RPP-RPT-63675, Rev. 0.0, Washington River Protection Solutions, Richland, Washington.

Jordan EL. 2022b. *Final Analytical Report for Tank 241-AN-106 Core 2020-10 Sampling and Analysis Plan*. RPP-RPT-63779, Rev. 0.0, Washington River Protection Solutions, Richland, Washington.

Laliberté M. 2007a. "Model for calculating the viscosity of aqueous solutions." *Journal of Chemical and Engineering Data* 52(2):321–335.

Laliberté M. 2007b. "Model for calculating the viscosity of aqueous solutions (vol 52, pg 321, 2007)." *Journal of Chemical and Engineering Data* 52(4):1507–1508.

Laliberté M. 2009. "A Model for Calculating the Heat Capacity of Aqueous Solutions, with Updated Density and Viscosity Data." *Journal of Chemical and Engineering Data* 54(6):1725–1760.

Laliberté M and WE Cooper. 2004. "Model for calculating the density of aqueous electrolyte solutions." *Journal of Chemical and Engineering Data* 49(5):1141–1151.

Lumetta G, E Buck, R Daniel, K Draper, M Edwards, S Fiskum, R Hallen, L Jagoda, E Jenson, A Kozelisky, P MacFarlan, R Peterson, R Shimskey, S Sinkov, and L Snow. 2009. *Characterization, Leaching, and Filtration Testing for Bismuth Phosphate Sludge (Group 1) and Bismuth Phosphate Saltcake (Group 2) Actual Waste Sample Composites*. PNNL-17992 (WTP-RPT-166, Rev. 0), Pacific Northwest National Laboratory, Richland, Washington.

Mahoney L, M Fountain, and C Burns. 2020. *Dissolution of Fluoride Salts in Hanford Tank Waste*. PNNL-30042, Rev. 0 (RPT-OSIF-010, Rev. 0), Pacific Northwest National Laboratory, Richland, Washington.

Matlack K, W Gong, T Bardakci, N D'Angelo, M Brandys, W Kot, and I Pegg. 2005. *Integrated DM1200 Melter Testing Using AZ-102 and C-106/AY-102 HLW Simulants: HLW Simulant Verification*. VSL-05R5800-1, Catholic University of America, Washington, D.C.

NQA-1-2012. 2012. *Quality Assurance Requirements for Nuclear Facility Applications*. American Society of Mechanical Engineers, New York, NY, nqa-1-2012 edition.

Oroskar A and R Turian. 1980. "The Critical Velocity in Pipeline Flow of Slurries." *AIChE Journal* 26(4):550–558.

Peterson R, S Fiskum, S Suffield, R Daniel, P Gauglitz, and B Wells. 2017. *Simulant Basis for the Standard High Solids Vessel Design*. PNNL-24476, Rev. 1 (WTP-RPT-241, Rev. 1), Pacific Northwest National Laboratory, Richland, Washington.

Poloski A, S Arm, O Bredt, T Calloway, Y Onishi, R Peterson, G Smith, and H Smith. 2006. *Final Report: Technical Basis for HLW Vitrification Stream Physical and Rheological Property Bounding Conditions*. PNWD-3675 (WTP-RPT-112, Rev. 0), Battelle—Pacific Northwest Division; Savannah River National Laboratory, Richland, Washington.

Reynolds JG and R Carter. 2007. "A density model for aqueous sodium hydroxide-sodium aluminate solutions." *Hydrometallurgy* 89:233–241.

Reynolds JG and R Carter. 2008a. "The Laliberte-Cooper density model: self-consistency and a new method of parameterization." *Fluid Phase Equilibria* 266:14–20.

Reynolds JG and R Carter. 2008b. "Reconciliation of solute concentration data with water contents and densities of multi-component electrolyte solutions." *Journal of Solution Chemistry* 37:1113–1125.

Reynolds JG, BM Mauss, and RC Daniel. 2018. "The relative viscosity of NaNO3 and NaNO2 aqueous solutions." *Journal of Molecular Liquids* 265:110–114.

Reynolds JG, BM Mauss, and RC Daniel. 2019. "The importance of ion interactions on electrolyte solution viscosities determined by comparing concentrated sodium carbonate and nitrate solutions." *Journal of Molecular Liquids* 228:111022.

Russell R, D Rinehart, H Smith, and R Peterson. 2009. *Development and Characterization of Gibbsite Component Simulant*. PNNL-18013 (WTP-RPT-176, Rev. 0), Pacific Northwest National Laboratory, Richland, WA.

Russell RL, PP Schonewill, and CA Burns. 2017. *Simulant Development for LAWPS Testing*. PNNL-26165, Rev. 0 (RPT-LPIST-001, Rev. 0), Pacific Northwest National Laboratory, Richland, Washington.

Schonewill P, L El Khoury, C Burns, and R Daniel. 2024. *Simulant Development of Potential 200 West Area Waste Feeds*. PNNL-36628, Rev. 0 (SWARM-RPT-001, Rev. 0), Pacific Northwest National Laboratory, Richland, Washington.

Shimskey R, J Billing, E Buck, A Casella, J Crum, R Daniel, K Draper, M Edwards, R Hallen, A Kozelisky, P MacFarlan, R Peterson, and R Swoboda. 2009a. *Filtration and Leach Testing for PUREX Cladding Sludge and REDOX Cladding Sludge Actual Waste Sample Composites*. PNNL-18048 (WTP-RPT-181, Rev. 0), Pacific Northwest National Laboratory, Richland, Washington.

Shimskey R, J Billing, E Buck, R Daniel, K Draper, M Edwards, J Geeting, R Hallen, E Jenson, A Kozelisky, P MacFarlan, R Peterson, L Snow, and R Swoboda. 2009b. *Filtration and Leach Testing for REDOX Sludge and S-Saltcake Actual Waste Sample Composites*. PNNL-17965 (WTP-RPT-172, Rev. 0), Pacific Northwest National Laboratory, Richland, Washington.

Snow L, E Buck, A Casella, J Crum, R Daniel, K Draper, M Edwards, S Fiskum, L Jagoda, E Jenson, A Kozelisky, P MacFarlan, R Peterson, and R Swoboda. 2009. *Characterization and Leach Testing for PUREX Cladding Waste Sludge (Group 3) and REDOX Cladding Waste Sludge (Group 4) Actual Waste Sample Composites*. PNNL-18054 (WTP-RPT-167, Rev. 0), Pacific Northwest National Laboratory, Richland, Washington.

Wells BE, MA Knight, EC Buck, RC Daniel, SK Cooley, LA Mahoney, PA Meyer, AP Poloski, JM Tingey, WS Callaway, GA Cooke, ME Johnson, MG Thien, DJ Washenfelder, JJ Davis, MN Hall, GL Smith, SL Thomson, and Y Onishi. 2007. *Estimate of Hanford Waste Insoluble Solid Particle Size and Density Distribution*. PNWD-3824, Rev. 0., Pacific Northwest National Laboratory, Richland, Washington.

Wells BE, DE Kurath, LA Mahoney, Y Onishi, JL Huckaby, SK Cooley, CA Burns, EC Buck, JM Tingey, RC Daniel, and KK Anderson. 2011. *Hanford Waste Physical and Rheological Properties: Data and Gaps*. PNNL-20646, Rev. 0, Pacific Northwest National Laboratory, Richland, Washington.

Westesen AM, AM Robb, NL Cappella, C Alvarez, and RA Peterson. 2023. *Phosphate and Fluoride Processing Options for Hanford Sludge*. PNNL-34456, Pacific Northwest National Laboratory, Richland, Washington.

Westesen AM, SE Asmussen, AA Bachman, T Trang-Le, L Sweet, EC Buck, and RA Peterson. 2025. *FY24 Task 5: Leachate Disposition*. PNNL-37627 Rev. 0 (ITSW-RPT-005 Rev. 0), Pacific Northwest National Laboratory, Richland, Washington.

Zwietering TN. 1958. "Suspending of solid particles in liquid by agitators." *Chemical Engineering Science* 8:244–253.

Appendix A – Waste Sample Jar Inspection

To support characterization of slurry transport properties for Hanford SE quadrant wastes, twenty-four waste core segment samples originating from Tanks AN-101, AN-106, and AW-105 were received by PNNL in the summer of 2024. As part of the sample receipt process, the samples—delivered in 30 to 60 mL Qorpak jars—were visually examined, and images were captured using a digital video recorder.

To fully assess the sample and sample jar integrity, both the exterior and the sample solids were evaluated. Evaluation of the sample solids involved the removal of each jar's lid and inspection of the jar interior. In general, three jar views were captured:

- The side of the jar (with a focus on observing the solids while avoiding jar labels),
- The bottom of the jar, and
- The interior view of the jar solids.

This appendix provides a high-level summary of the images collected during the sample receipt inspection, along with sample mass and other metadata. For each sample, the associated tank core segment, initial mass, and final mass are recorded. Tanks are referenced by their full Hanford ID (e.g., 241-AN-101 for Tank AN-101). The initial mass refers to the gross sample mass, which includes sludge, container with lid, label, and tape, as recorded during initial inspection. The final mass represents the gross container mass after a small sample (1 gram or less) was removed from selected jars.

A.1 Tank AN-101, Core Segment 340-12 LH

Tank: 241-AN-101
Core: 340
Segment: 12 LH
Jar: 21402
Lab ID: S21T021171
Initial Mass: 151.58 g
Final Mass: 151.58 g
Reference: RPP-RPT-63675 Rev.00



Figure A.1. Side view of Jar 21402 (Tank AN-101, Core Segment 340-12 LH)

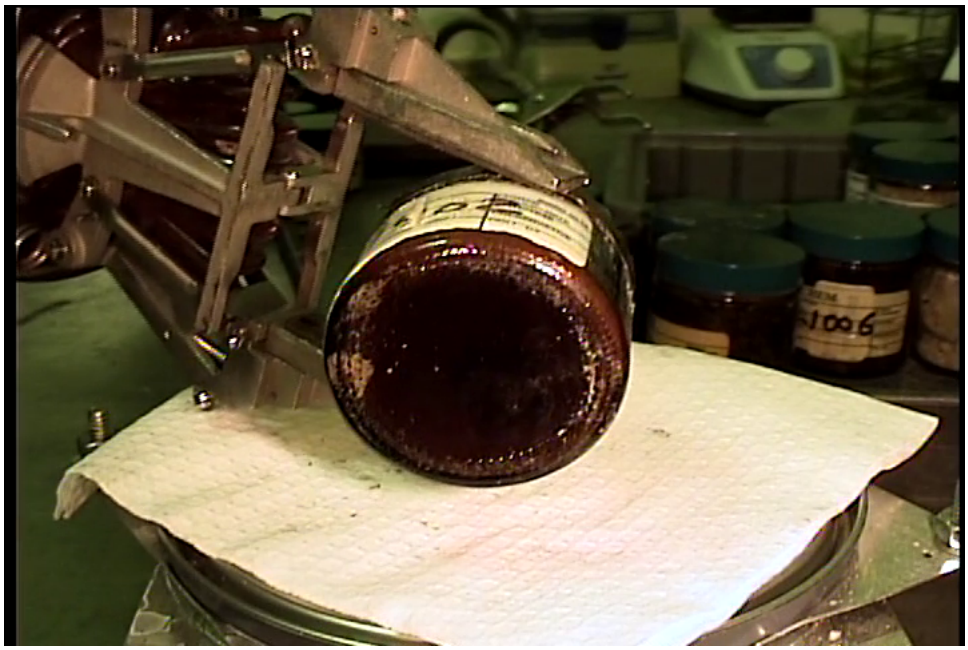


Figure A.2. Bottom view of Jar 21402 (Tank AN-101, Core Segment 340-12 LH)

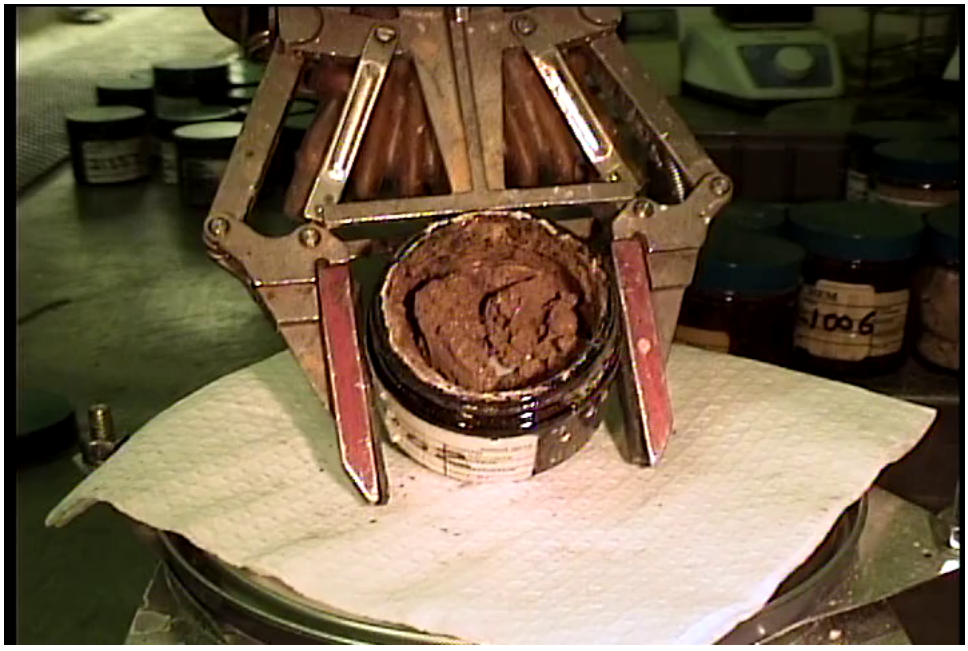


Figure A.3. Solids view of Jar 21402 (Tank AN-101, Core Segment 340-12 LH)

A.2 Tank AN-101, Core Segment 340-12 UH

Tank: 241-AN-101
Core: 340
Segment: 12 UH
Jar: 21403
Lab ID: S21T021172
Initial Mass: 101.05 g
Final Mass: 101.05 g
Reference: RPP-RPT-63675 Rev.00



Figure A.4. Side view of Jar 21403 (Tank AN-101, Core Segment 340-12 UH)

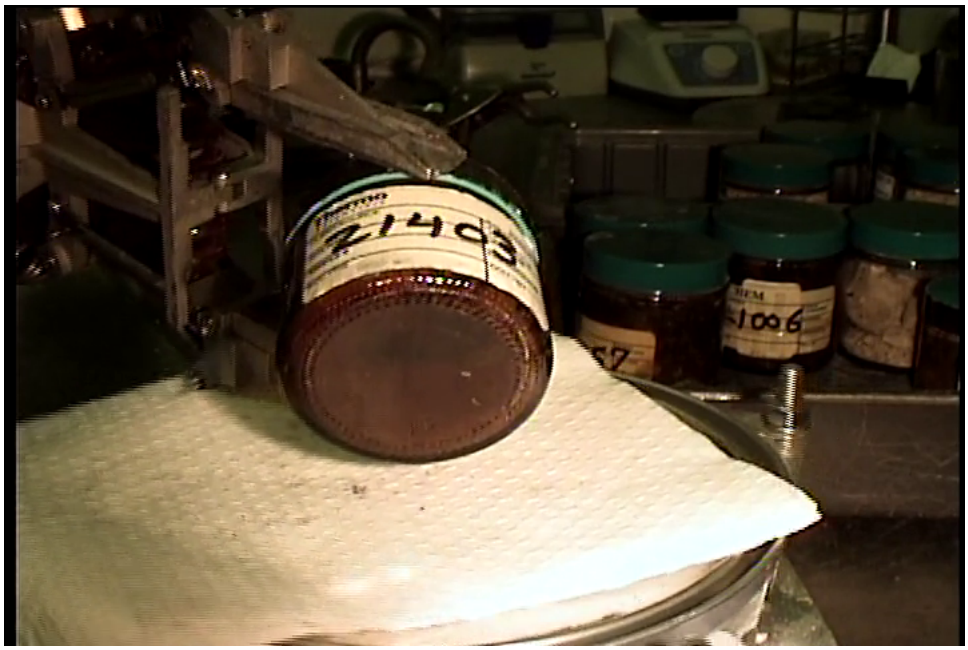


Figure A.5. Bottom view of Jar 21403 (Tank AN-101, Core Segment 340-12 UH)

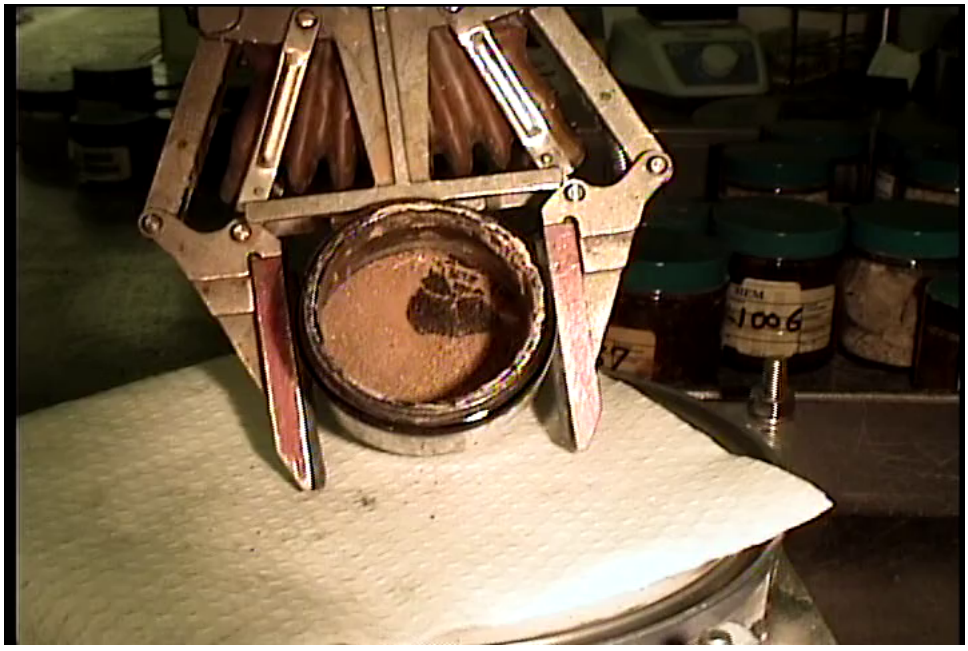


Figure A.6. Solids view of Jar 21403 (Tank AN-101, Core Segment 340-12 UH)

A.3 Tank AN-101, Core Segment 340-13 LH

Tank: 241-AN-101
Core: 340
Segment: 13 LH
Jar: 21378
Lab ID: S21R000250
Initial Mass: 143.76 g
Final Mass: 143.76 g
Reference: RPP-RPT-63675 Rev.00

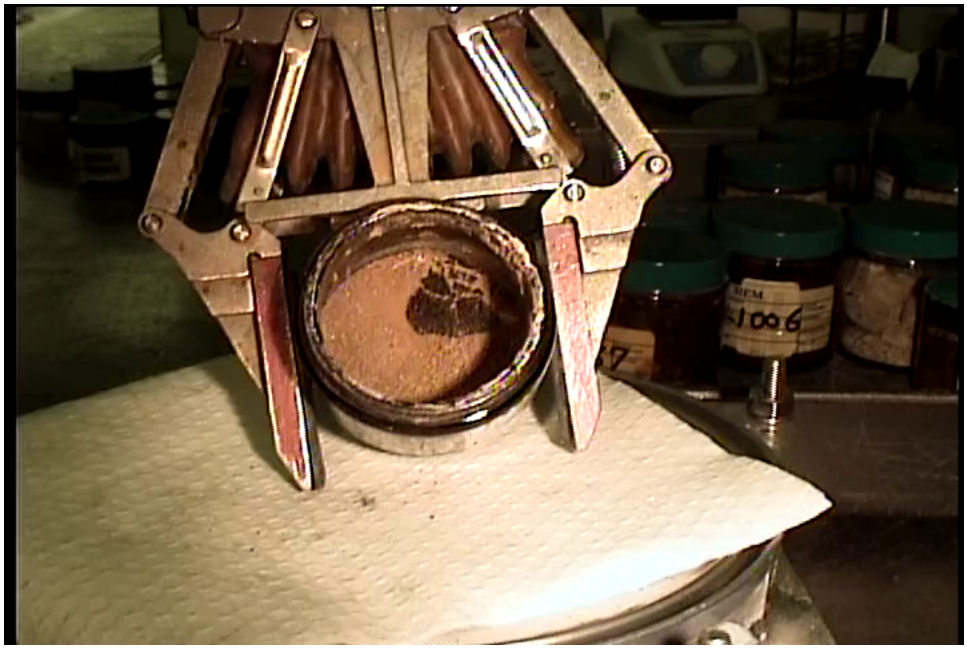


Figure A.7. Side view of Jar 21378 (Tank AN-101, Core Segment 340-13 LH)

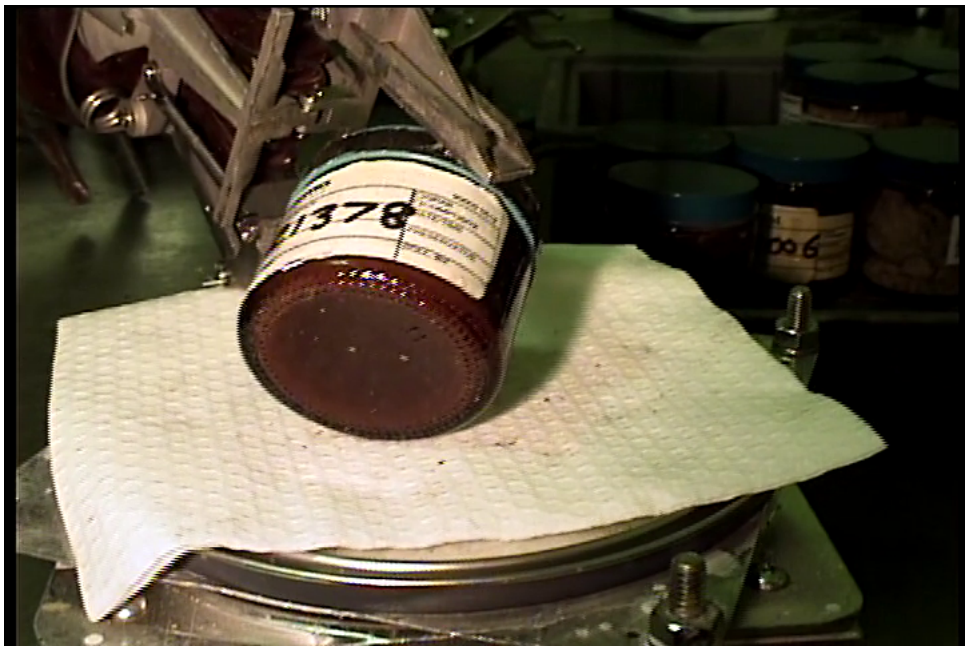


Figure A.8. Bottom view of Jar 21378 (Tank AN-101, Core Segment 340-13 LH)

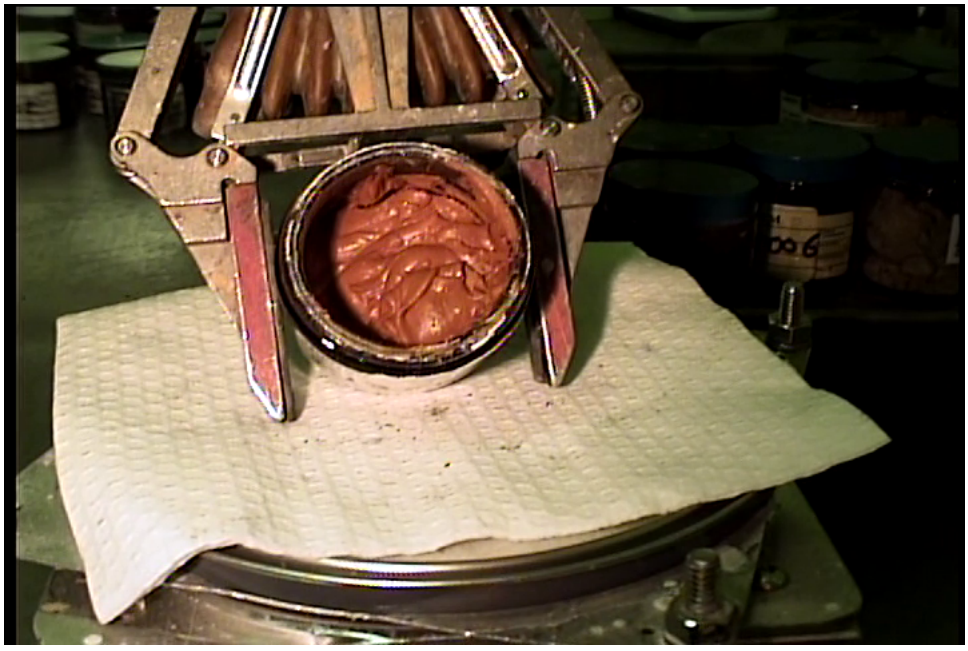


Figure A.9. Solids view of Jar 21378 (Tank AN-101, Core Segment 340-13 LH)

A.4 Tank AN-101, Core Segment 340-13 UH

Tank: 241-AN-101
Core: 340
Segment: 13 UH
Jar: 21404
Lab ID: S21T021201
Initial Mass: 147.04 g
Final Mass: 147.04 g
Reference: RPP-RPT-63675 Rev.00

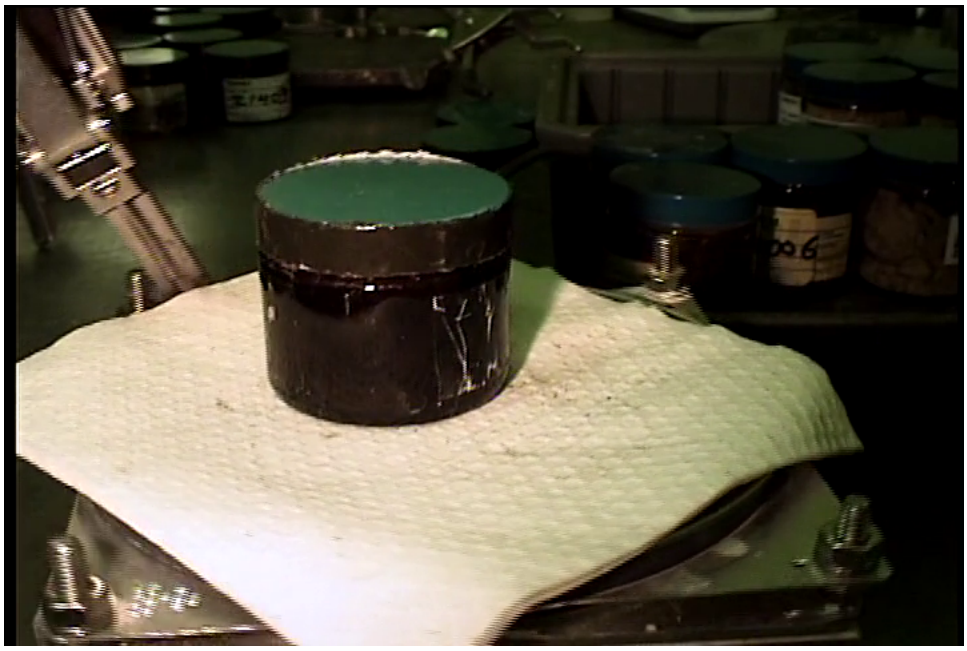


Figure A.10. Side view of Jar 21404 (Tank AN-101, Core Segment 340-13 UH)

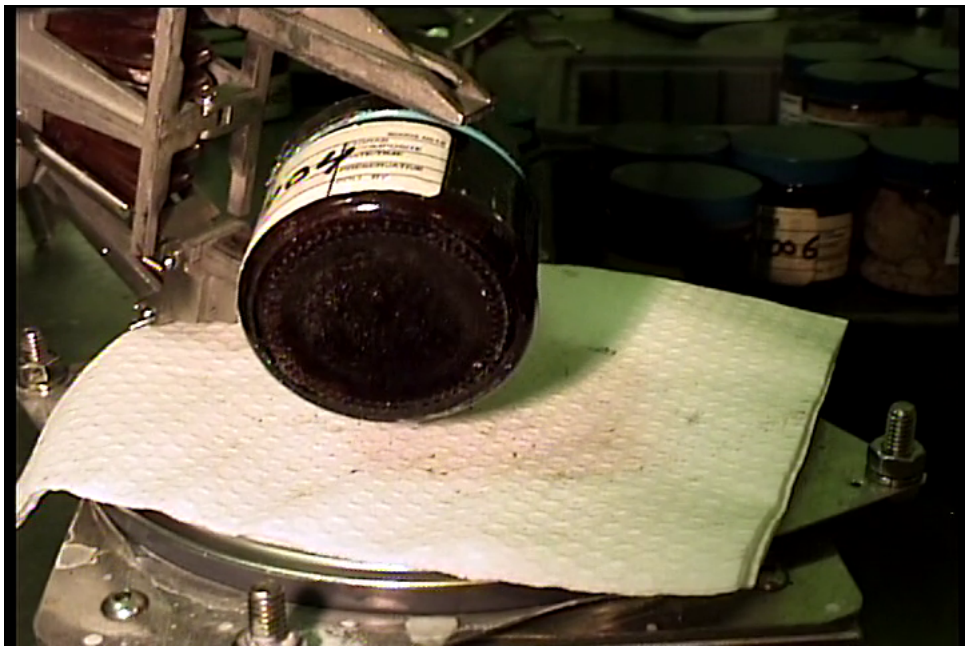


Figure A.11. Bottom view of Jar 21404 (Tank AN-101, Core Segment 340-13 UH)

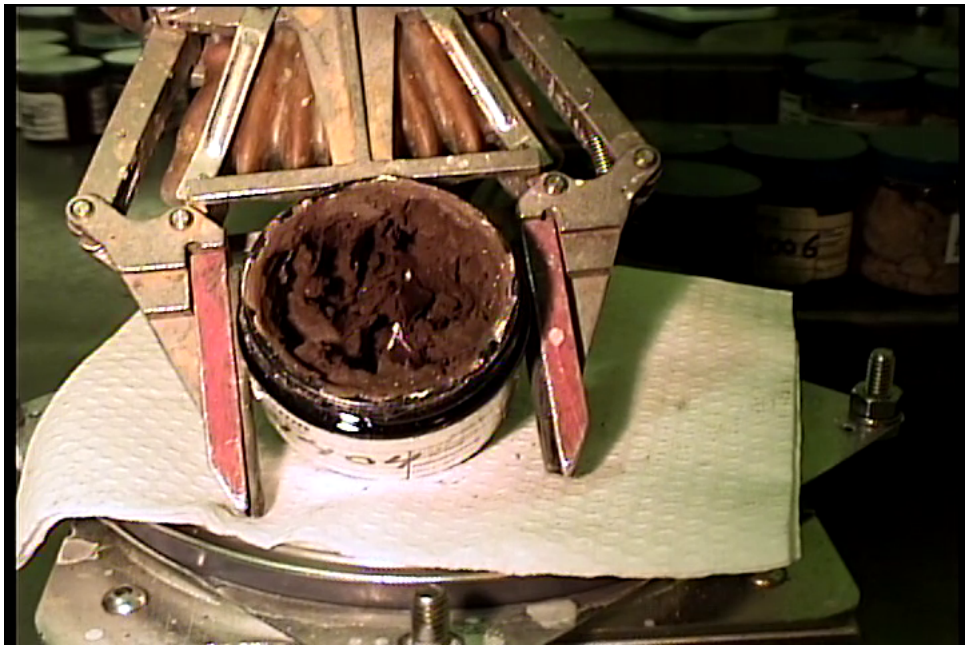


Figure A.12. Solids view of Jar 21404 (Tank AN-101, Core Segment 340-13 UH)

A.5 Tank AN-101, Core Segment 340-14 UH

Tank: 241-AN-101
Core: 340
Segment: 14 UH
Jar: 21407
Lab ID: S21T021230
Initial Mass: 106.68 g
Final Mass: 106.12 g
Reference: RPP-RPT-63675 Rev.00

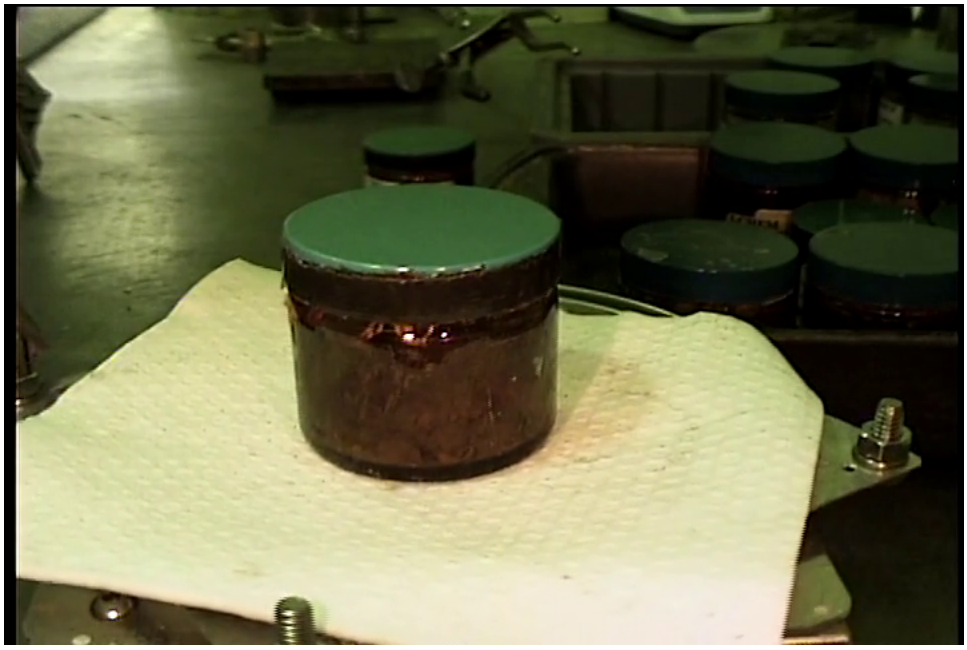


Figure A.13. Side view of Jar 21407 (Tank AN-101, Core Segment 340-14 UH)

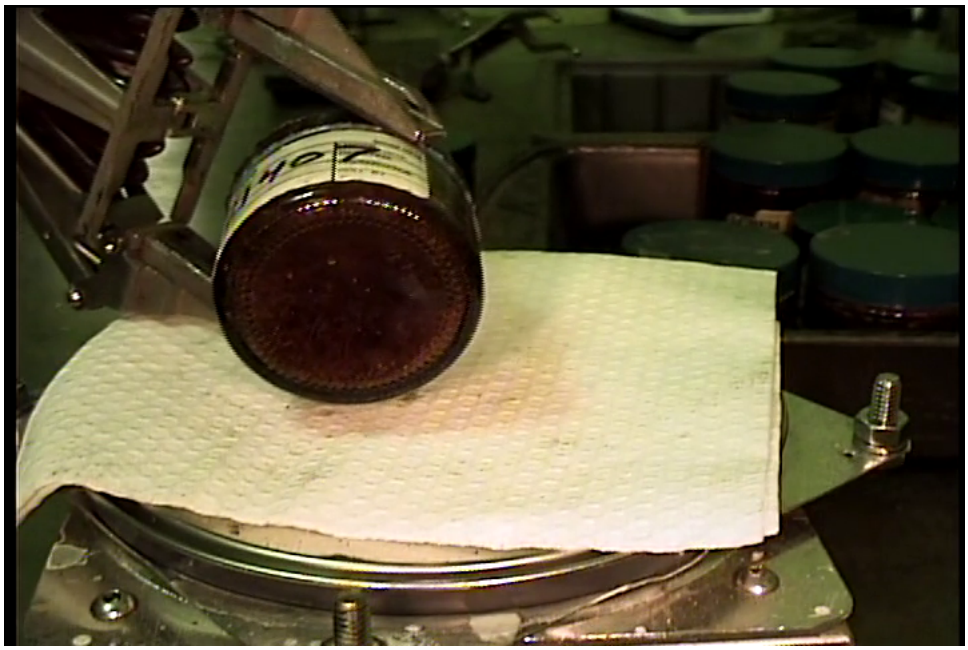


Figure A.14. Bottom view of Jar 21407 (Tank AN-101, Core Segment 340-14 UH)

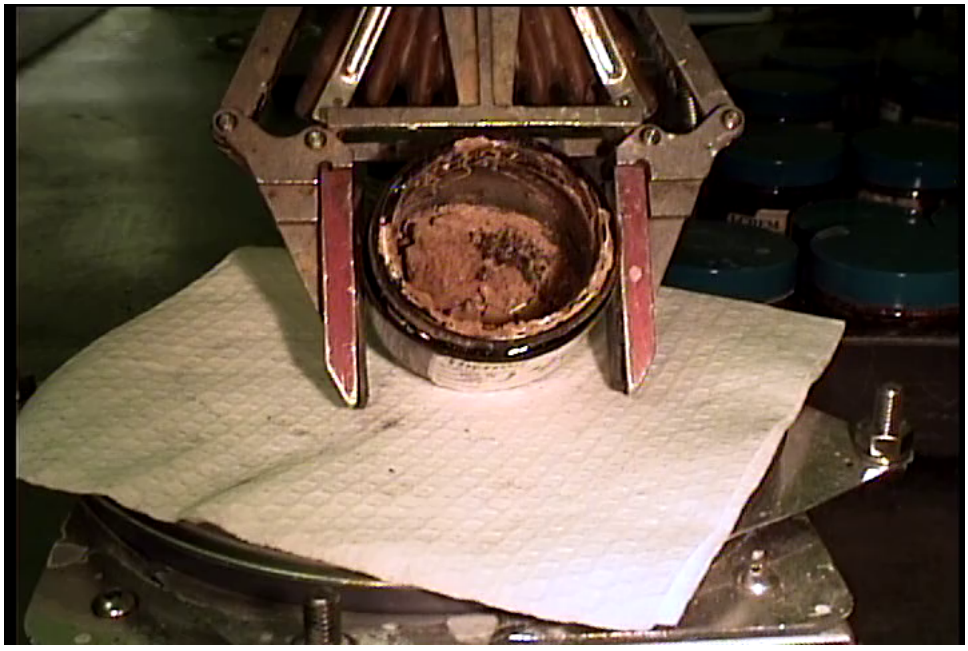


Figure A.15. Solids view of Jar 21407 (Tank AN-101, Core Segment 340-14 UH)

A.6 Tank AN-101, Core Segment 340-18 LH

Tank: 241-AN-101
Core: 340
Segment: 18 LH
Jar: 21415
Lab ID: S21T021675
Initial Mass: 133.67 g
Final Mass: 133.06 g
Reference: RPP-RPT-63675 Rev.00

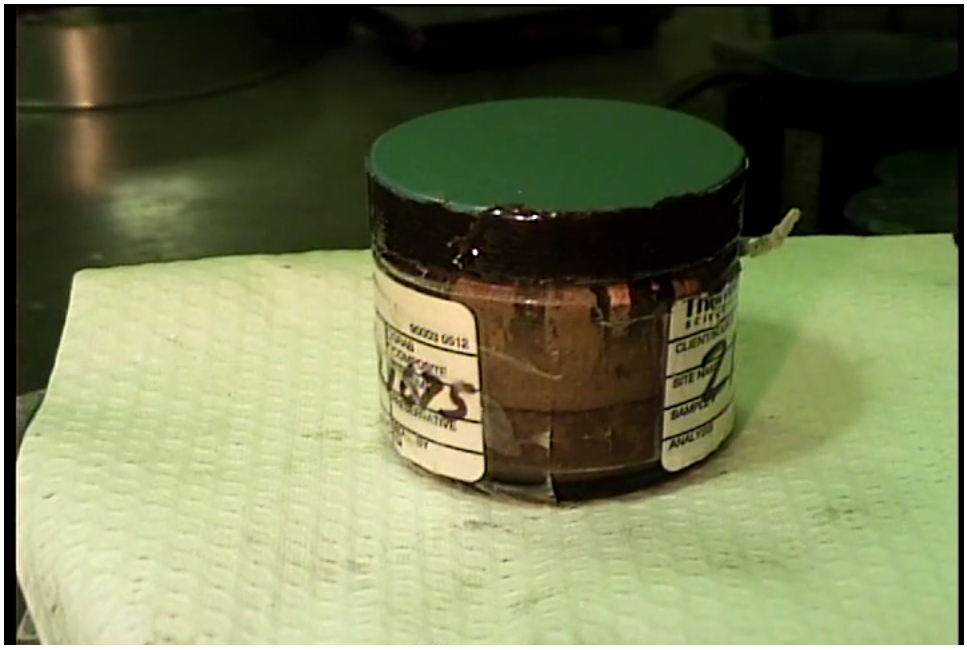


Figure A.16. Side view of Jar 21415 (Tank AN-101, Core Segment 340-18 LH)



Figure A.17. Bottom view of Jar 21415 (Tank AN-101, Core Segment 340-18 LH)



Figure A.18. Solids view of Jar 21415 (Tank AN-101, Core Segment 340-18 LH)

A.7 Tank AN-101, Core Segment 340-18 UH

Tank: 241-AN-101
Core: 340
Segment: 18 UH
Jar: 21416
Lab ID: S21T021676
Initial Mass: 178.82 g
Final Mass: 178.82 g
Reference: RPP-RPT-63675 Rev.00



Figure A.19. Side view of Jar 21416 (Tank AN-101, Core Segment 340-18 UH)

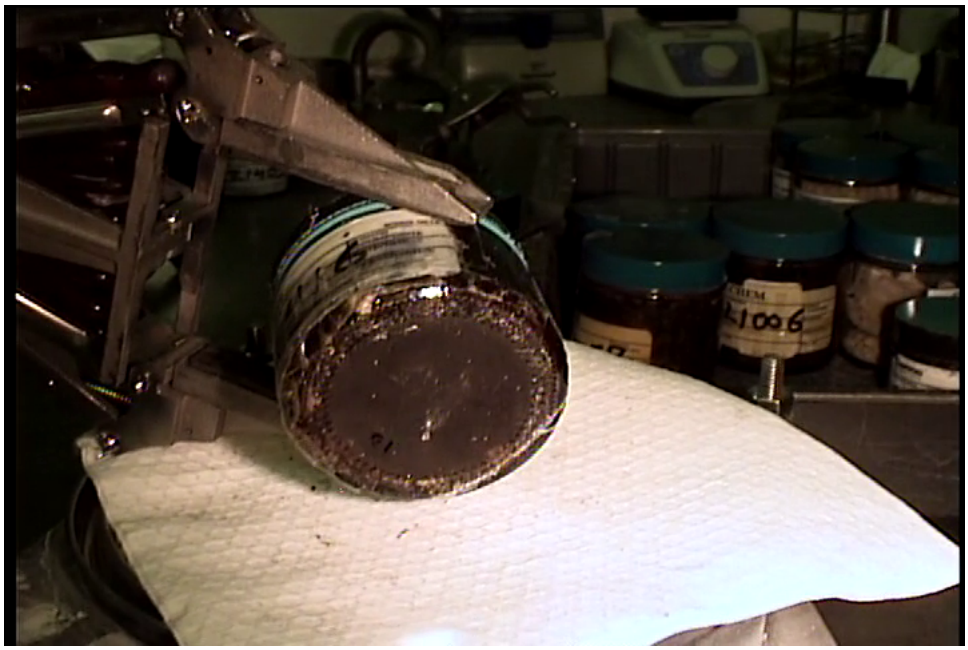


Figure A.20. Bottom view of Jar 21416 (Tank AN-101, Core Segment 340-18 UH)



Figure A.21. Solids view of Jar 21416 (Tank AN-101, Core Segment 340-18 UH)

A.8 Tank AN-101, Core Segment 340-19 LH

Tank: 241-AN-101
Core: 340
Segment: 19 LH
Jar: 21417
Lab ID: S21T021747
Initial Mass: 140.82 g
Final Mass: 139.85 g
Reference: RPP-RPT-63675 Rev.00

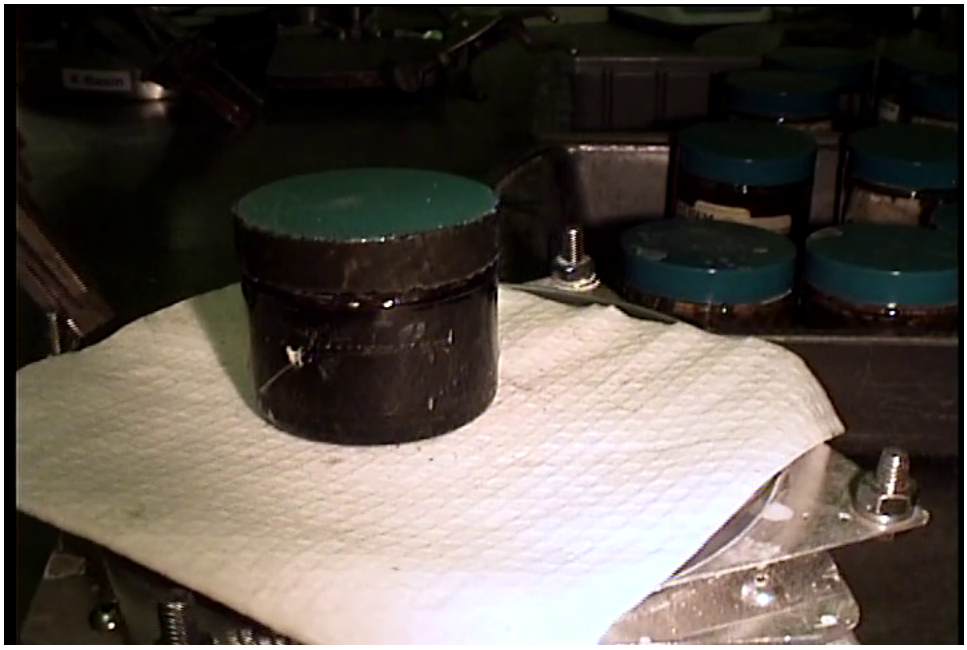


Figure A.22. Side view of Jar 21417 (Tank AN-101, Core Segment 340-19 LH)

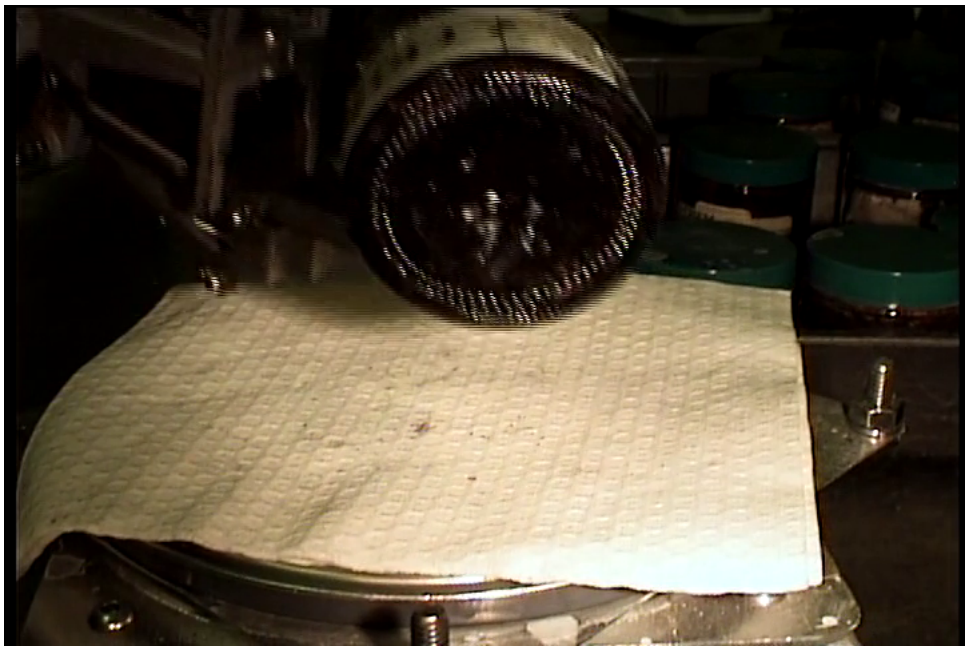


Figure A.23. Bottom view of Jar 21417 (Tank AN-101, Core Segment 340-19 LH)



Figure A.24. Solids view of Jar 21417 (Tank AN-101, Core Segment 340-19 LH)

A.9 Tank AN-106, Core Segment 339-14

Tank: 241-AN-106
Core: 339
Segment: 14
Jar: 20913
Lab ID: S20T016919
Initial Mass: 210.35 g
Final Mass: 210.02 g
Reference: RPP-RPT-63779 Rev.00



Figure A.25. Side view of Jar 20913 (Tank AN-106, Core Segment 339-14)

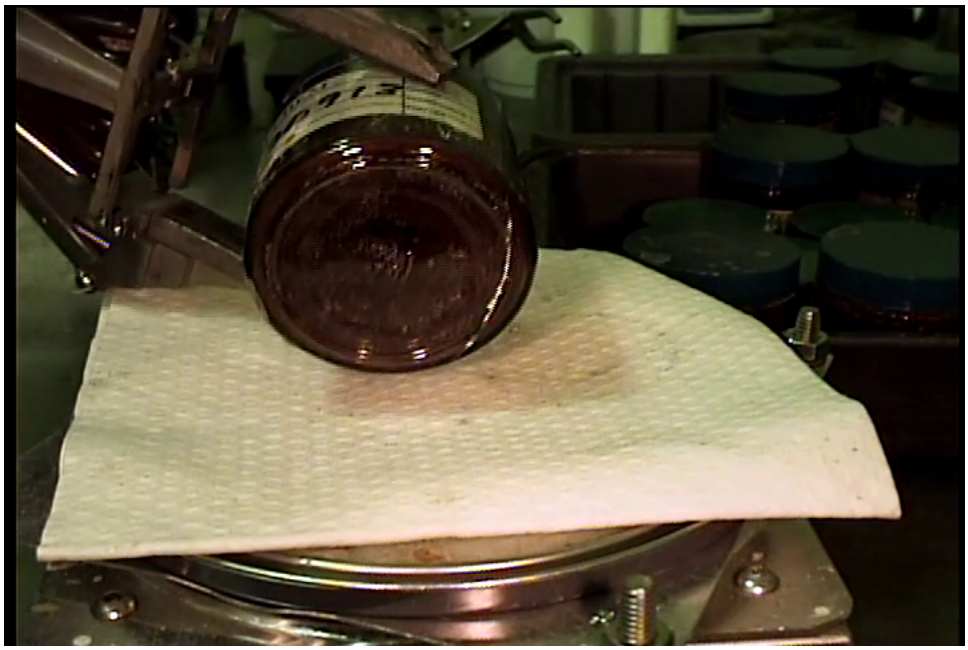


Figure A.26. Bottom view of Jar 20913 (Tank AN-106, Core Segment 339-14)

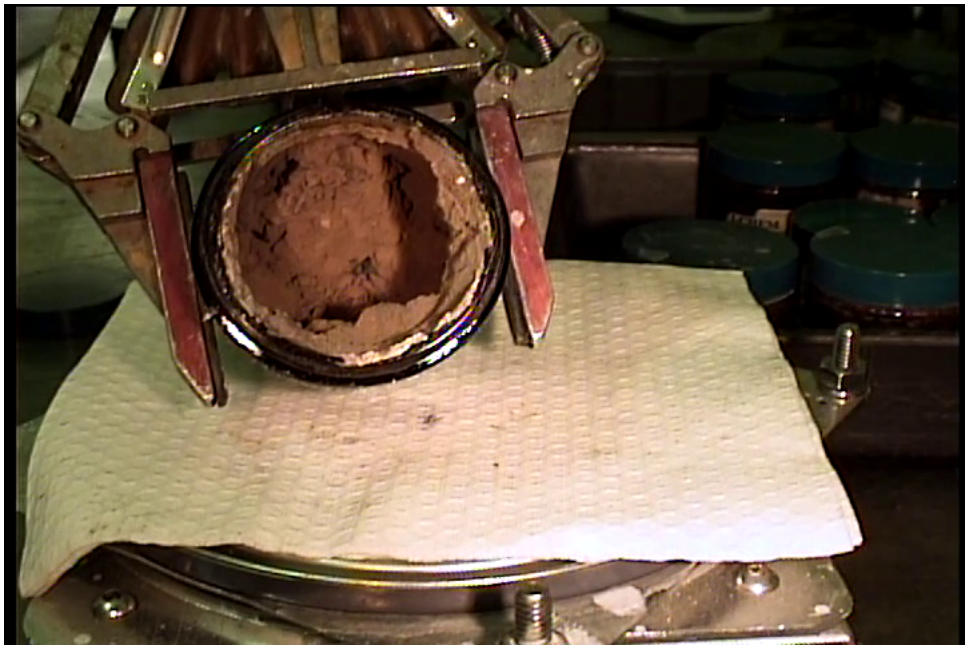


Figure A.27. Solids view of Jar 20913 (Tank AN-106, Core Segment 339-14)

A.10 Tank AN-106, Core Segment 339-15 LH

Tank: 241-AN-106
Core: 339
Segment: 15 LH
Jar: 21006
Lab ID: S20T017241
Initial Mass: 159.35 g
Final Mass: 159.35 g
Reference: RPP-RPT-63779 Rev.00



Figure A.28. Side view of Jar 21006 (Tank AN-106, Core Segment 339-15 LH)

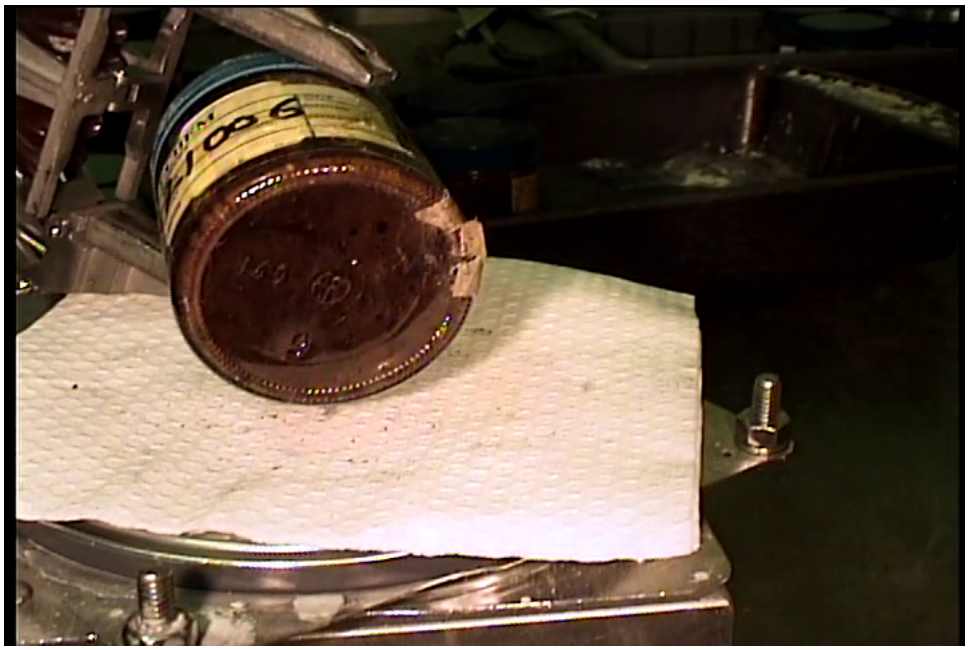


Figure A.29. Bottom view of Jar 21006 (Tank AN-106, Core Segment 339-15 LH)

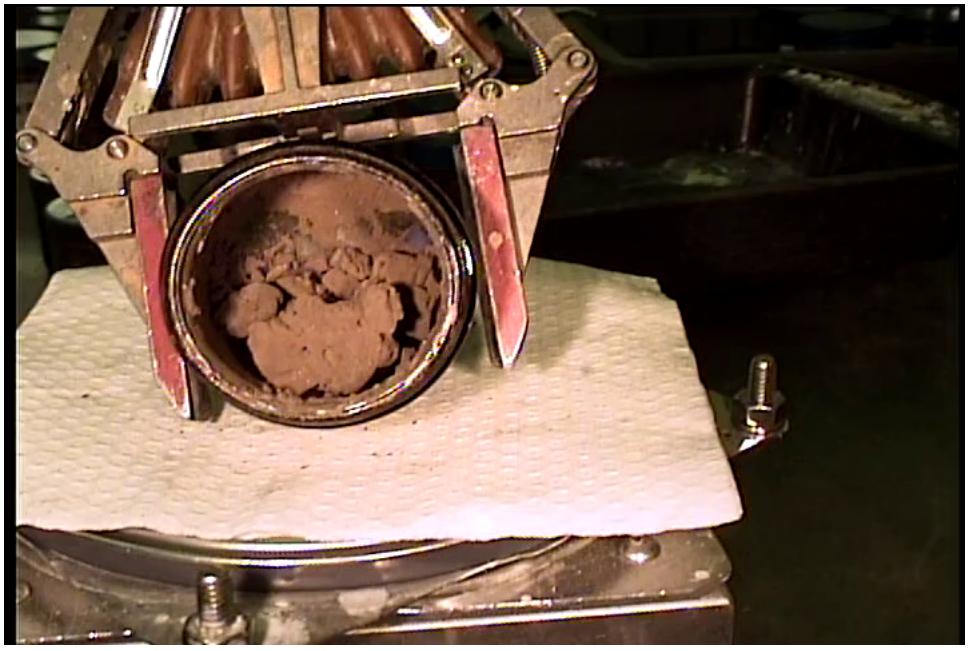


Figure A.30. Solids view of Jar 21006 (Tank AN-106, Core Segment 339-15 LH)

A.11 Tank AN-106, Core Segment 339-15 UH

Tank: 241-AN-106
Core: 339
Segment: 15 UH
Jar: 20918
Lab ID: S20T017242
Initial Mass: 174.26 g
Final Mass: 174.26 g
Reference: RPP-RPT-63779 Rev.00

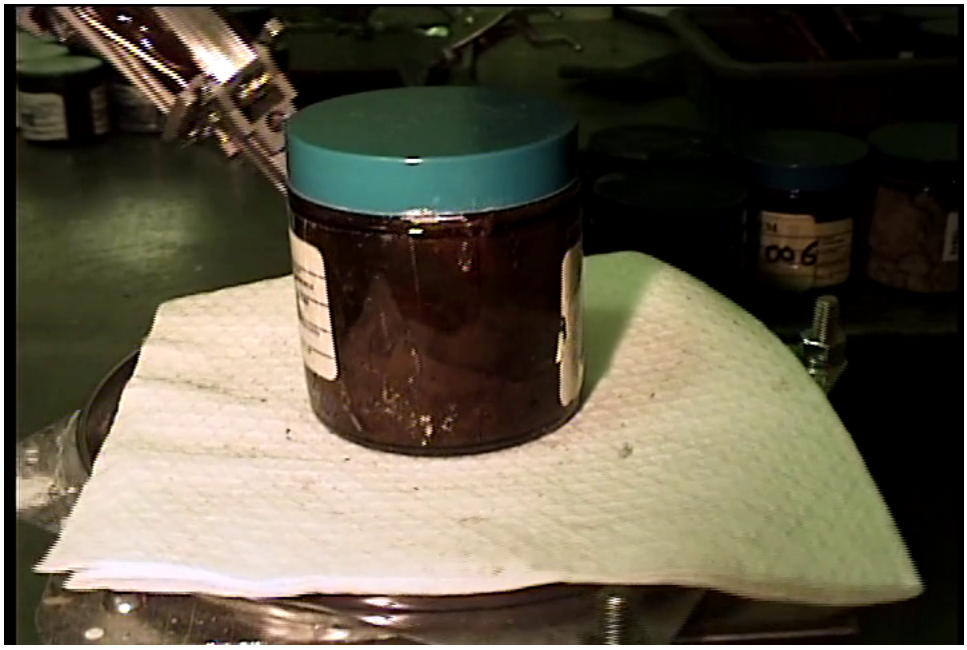


Figure A.31. Side view of Jar 20918 (Tank AN-106, Core Segment 339-15 UH)

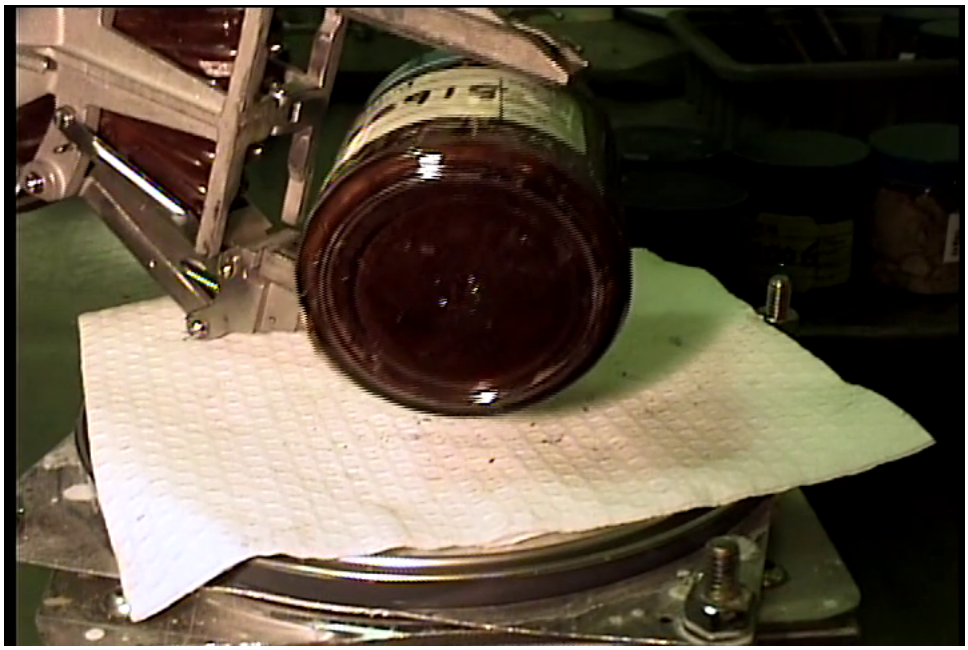


Figure A.32. Bottom view of Jar 20918 (Tank AN-106, Core Segment 339-15 UH)



Figure A.33. Solids view of Jar 20918 (Tank AN-106, Core Segment 339-15 UH)

A.12 Tank AN-106, Core Segment 339-16 LH

Tank: 241-AN-106
Core: 339
Segment: 16 LH
Jar: 21314
Lab ID: S20T017587
Initial Mass: 135.28 g
Final Mass: 134.52 g
Reference: RPP-RPT-63779 Rev.00



Figure A.34. Side view of Jar 21314 (Tank AN-106, Core Segment 339-16 LH)

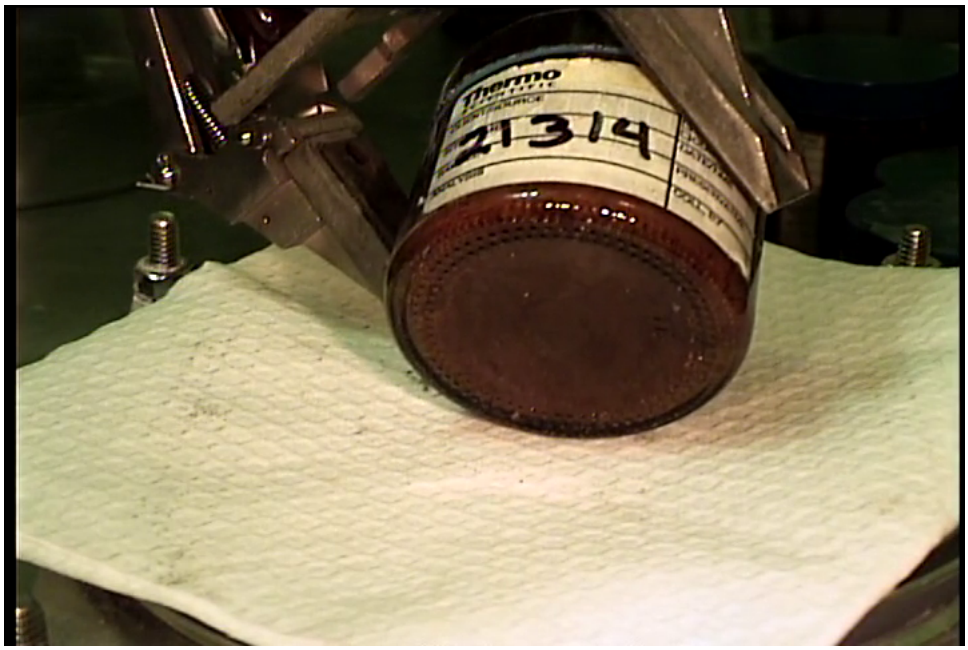


Figure A.35. Bottom view of Jar 21314 (Tank AN-106, Core Segment 339-16 LH)

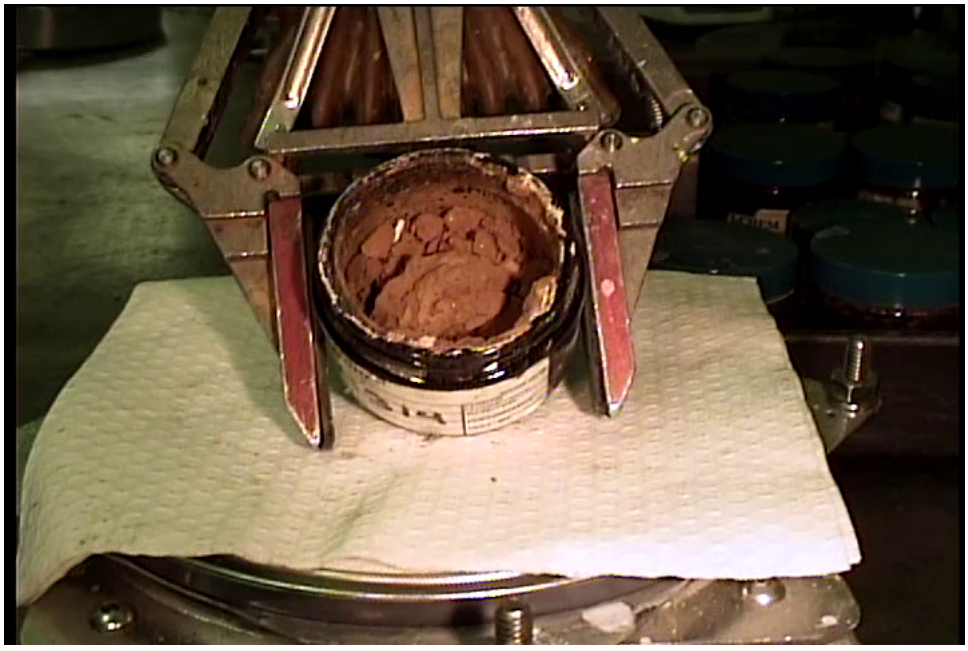


Figure A.36. Solids view of Jar 21314 (Tank AN-106, Core Segment 339-16 LH)

A.13 Tank AN-106, Core Segment 339-16 UH

Tank: 241-AN-106
Core: 339
Segment: 16 UH
Jar: 21315
Lab ID: S20T017588
Initial Mass: 129.15 g
Final Mass: 129.15 g
Reference: RPP-RPT-63779 Rev.00

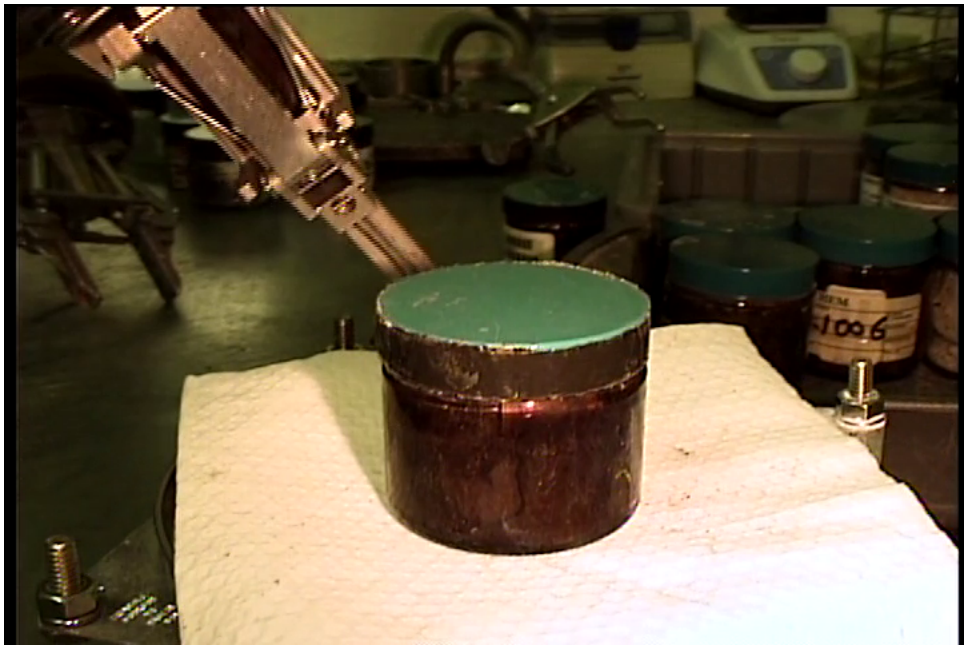


Figure A.37. Side view of Jar 21315 (Tank AN-106, Core Segment 339-16 UH)

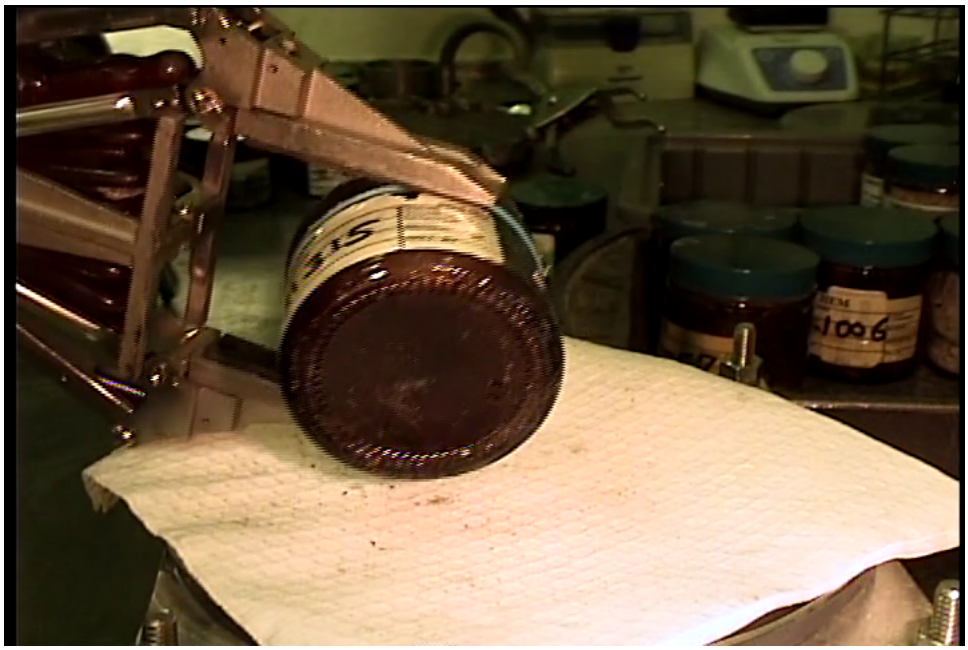


Figure A.38. Bottom view of Jar 21315 (Tank AN-106, Core Segment 339-16 UH)

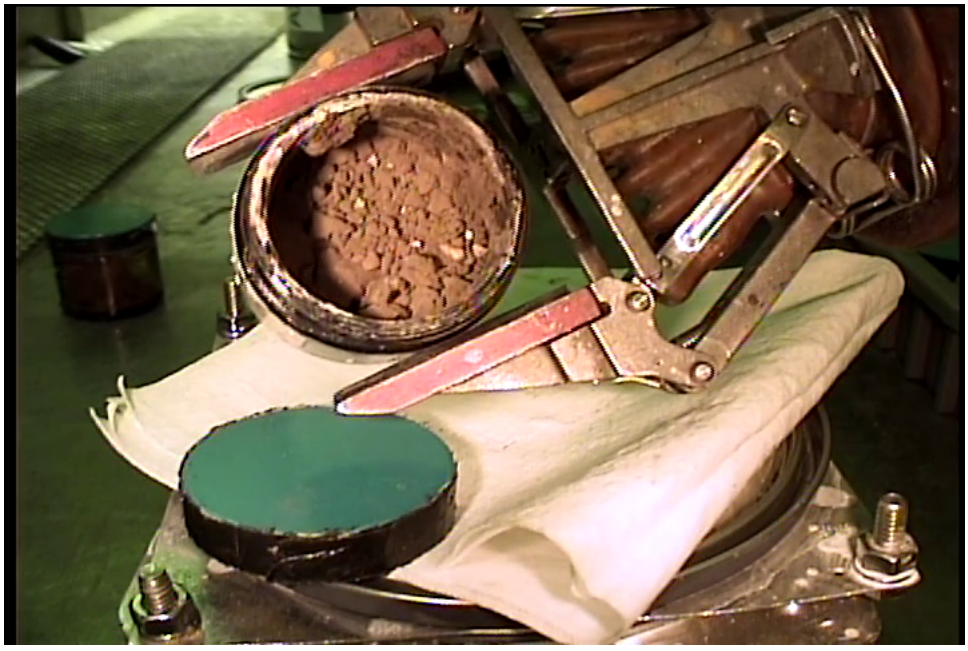


Figure A.39. Solids view of Jar 21315 (Tank AN-106, Core Segment 339-16 UH)

A.14 Tank AN-106, Core Segment 339-18 UH

Tank: 241-AN-106
Core: 339
Segment: 18 UH
Jar: 21357
Lab ID: S20T017662
Initial Mass: 123.73 g
Final Mass: 123.73 g
Reference: RPP-RPT-63779 Rev.00

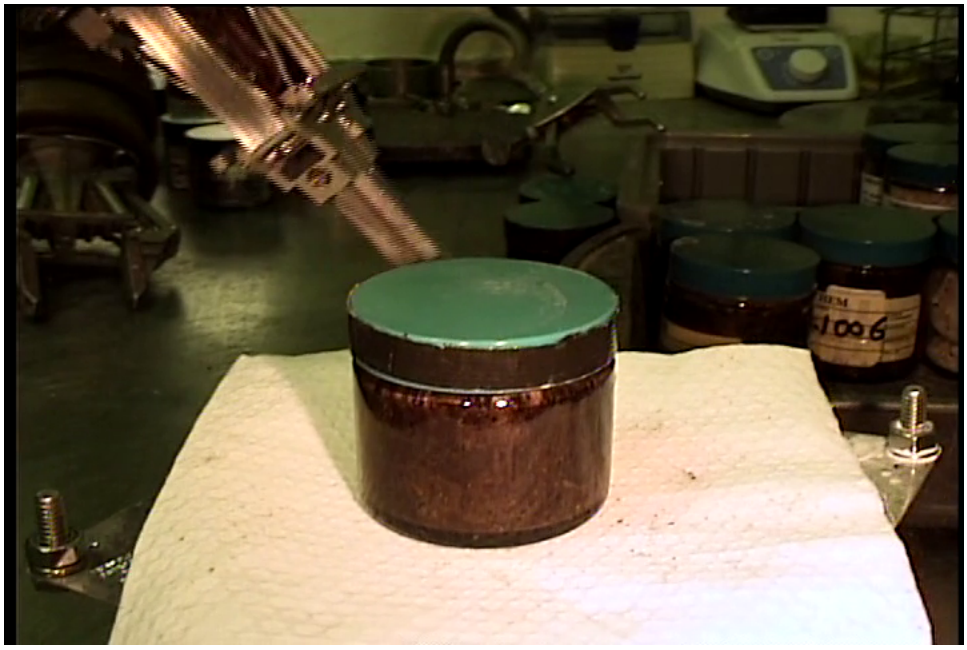


Figure A.40. Side view of Jar 21357 (Tank AN-106, Core Segment 339-18 UH)

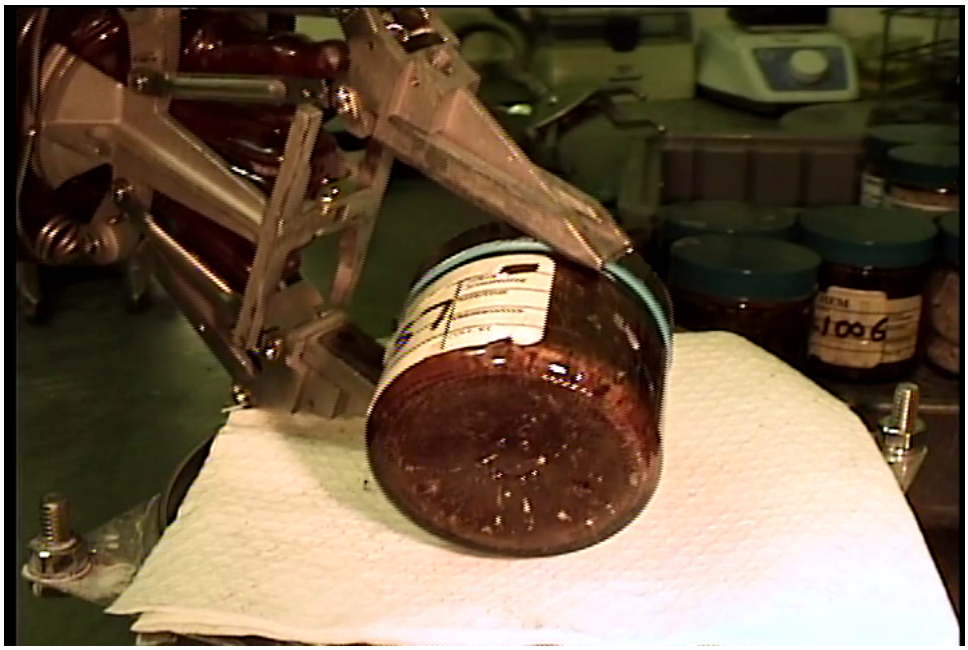


Figure A.41. Bottom view of Jar 21357 (Tank AN-106, Core Segment 339-18 UH)

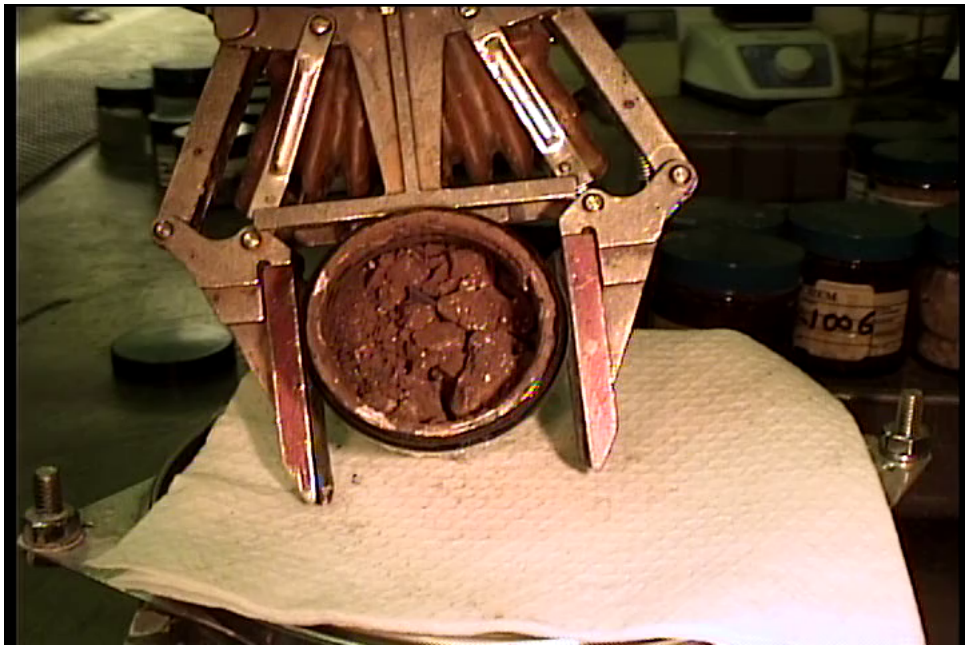


Figure A.42. Solids view of Jar 21357 (Tank AN-106, Core Segment 339-18 UH)

A.15 Tank AN-106, Core Segment 339-19 LH

Tank: 241-AN-106
Core: 339
Segment: 19 LH
Jar: 21360
Lab ID: S20T017884
Initial Mass: 102.74 g
Final Mass: 102.19 g
Reference: RPP-RPT-63779 Rev.00

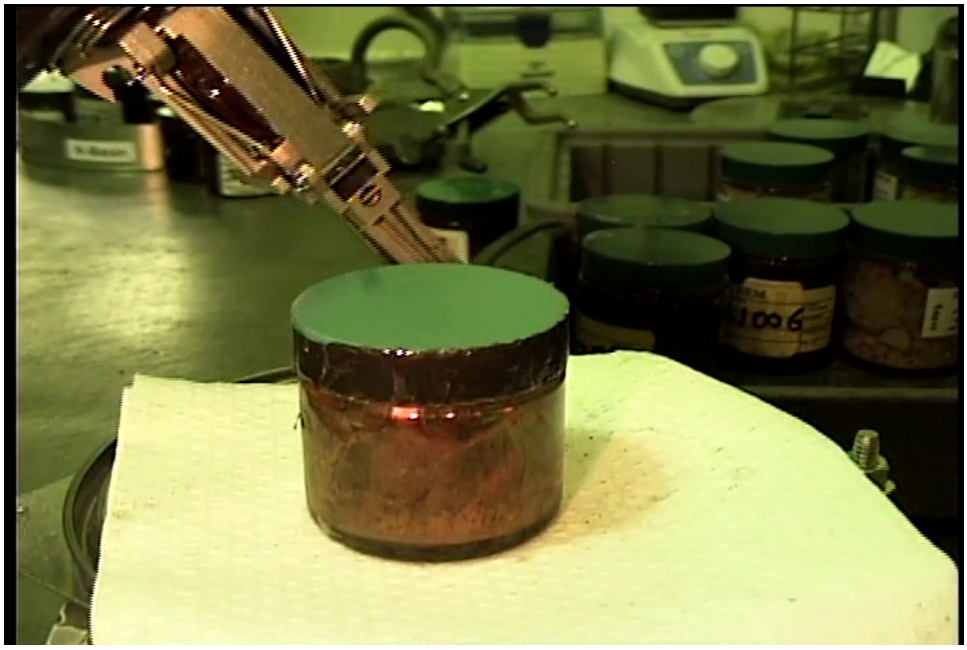


Figure A.43. Side view of Jar 21360 (Tank AN-106, Core Segment 339-19 LH)

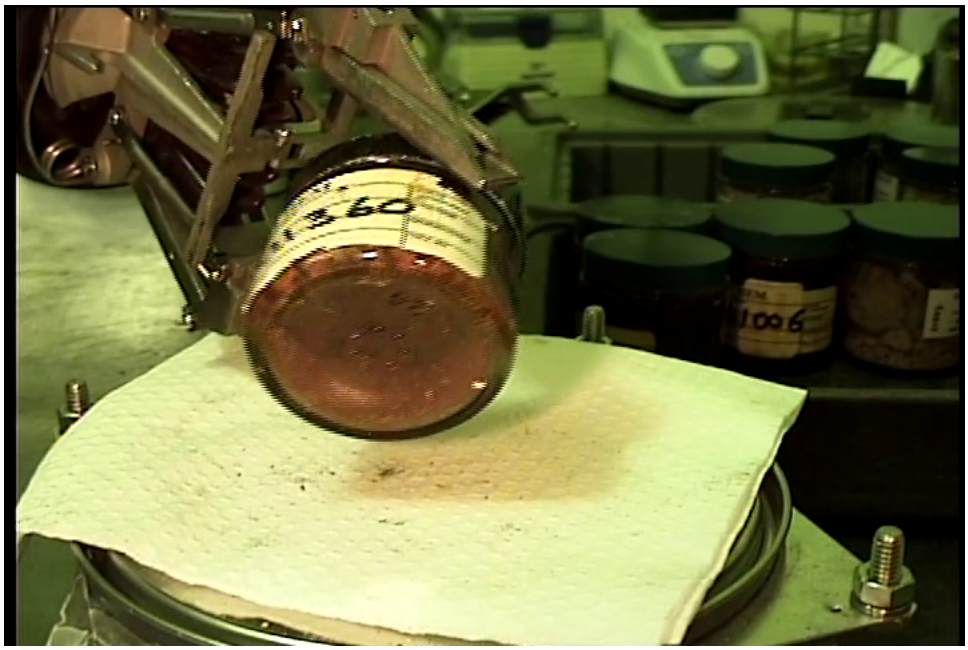


Figure A.44. Bottom view of Jar 21360 (Tank AN-106, Core Segment 339-19 LH)

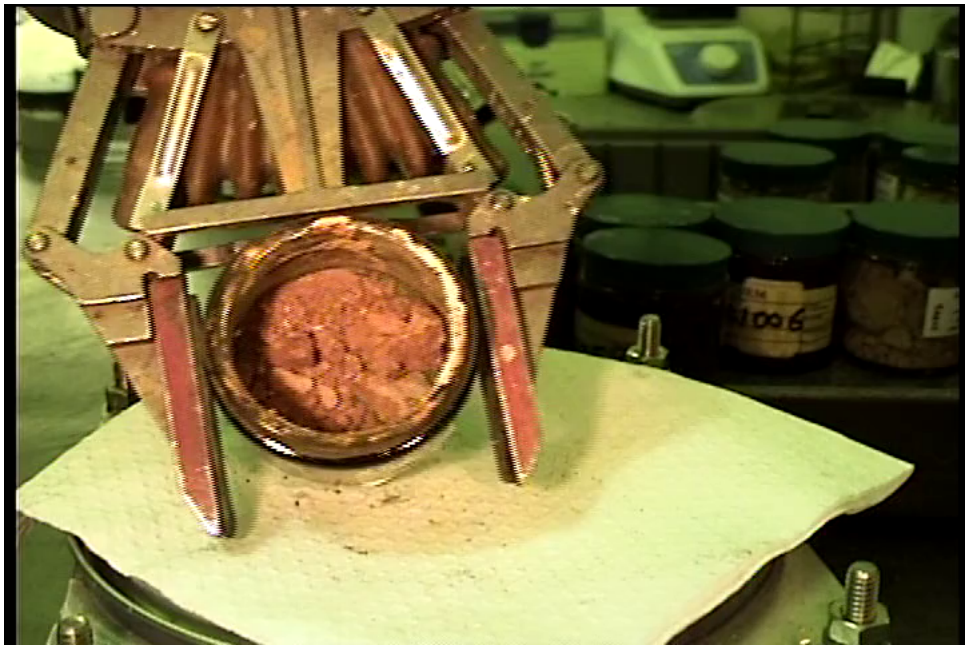


Figure A.45. Solids view of Jar 21360 (Tank AN-106, Core Segment 339-19 LH)

A.16 Tank AN-106, Core Segment 339-19 UH

Tank: 241-AN-106
Core: 339
Segment: 19 UH
Jar: 21361
Lab ID: S20T017885
Initial Mass: 112.37 g
Final Mass: 112.05 g
Reference: RPP-RPT-63779 Rev.00

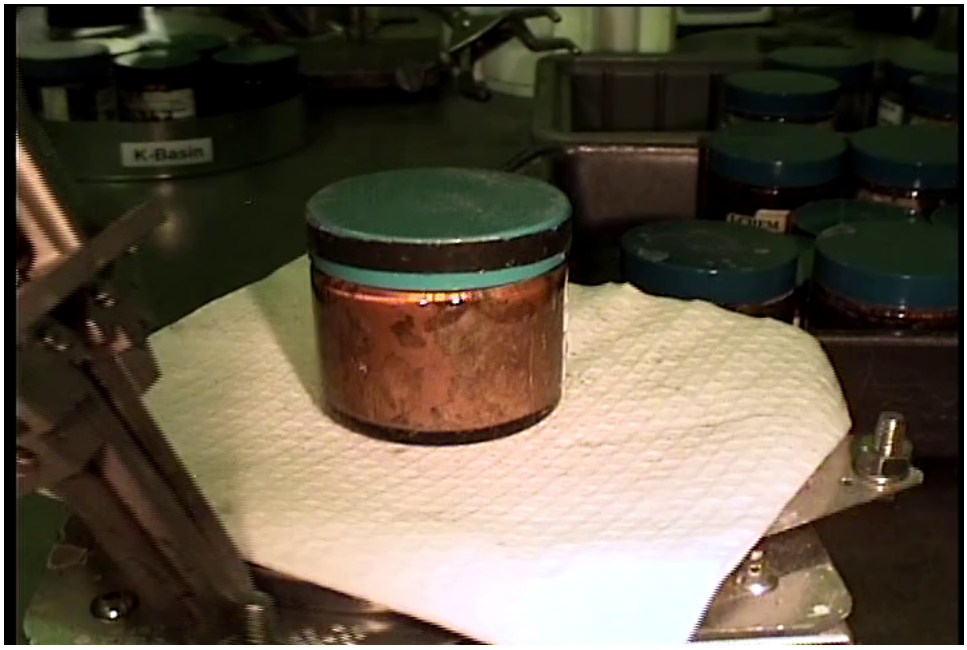


Figure A.46. Side view of Jar 21361 (Tank AN-106, Core Segment 339-19 UH)

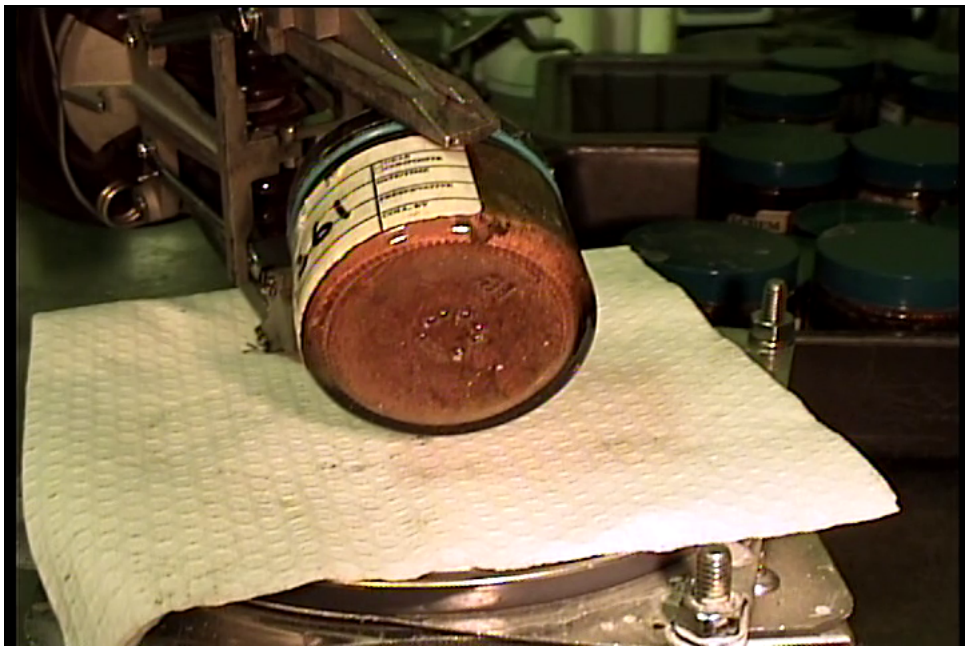


Figure A.47. Bottom view of Jar 21361 (Tank AN-106, Core Segment 339-19 UH)

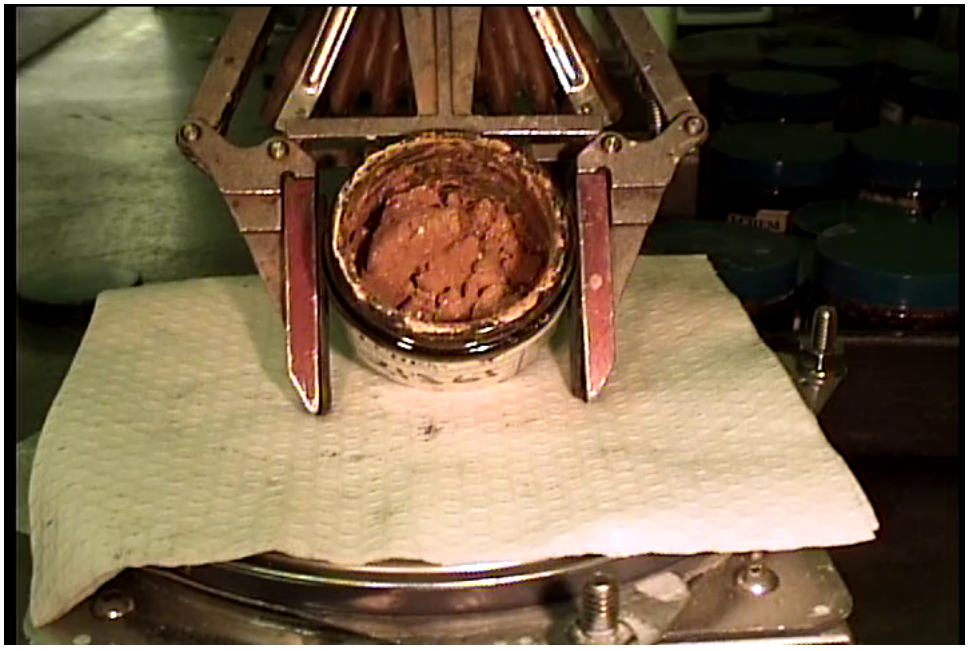


Figure A.48. Solids view of Jar 21361 (Tank AN-106, Core Segment 339-19 UH)

A.17 Tank AN-106, Core Segment 339-20 UH

Tank: 241-AN-106
Core: 339
Segment: 20 UH
Jar: 21362
Lab ID: S20T018179
Initial Mass: 107.23 g
Final Mass: 107.23 g
Reference: RPP-RPT-63779 Rev.00

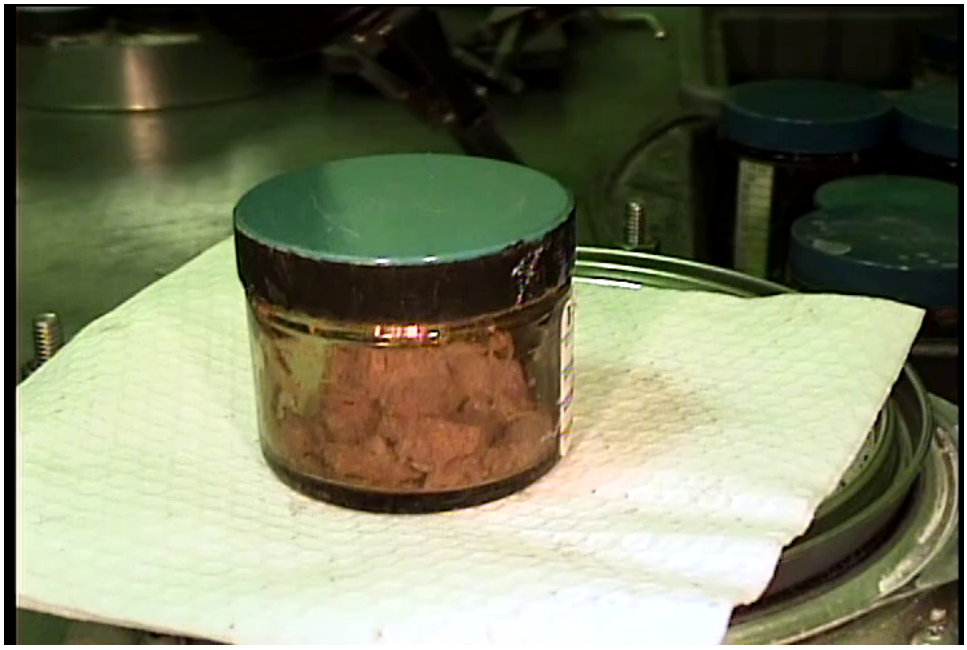


Figure A.49. Side view of Jar 21362 (Tank AN-106, Core Segment 339-20 UH)

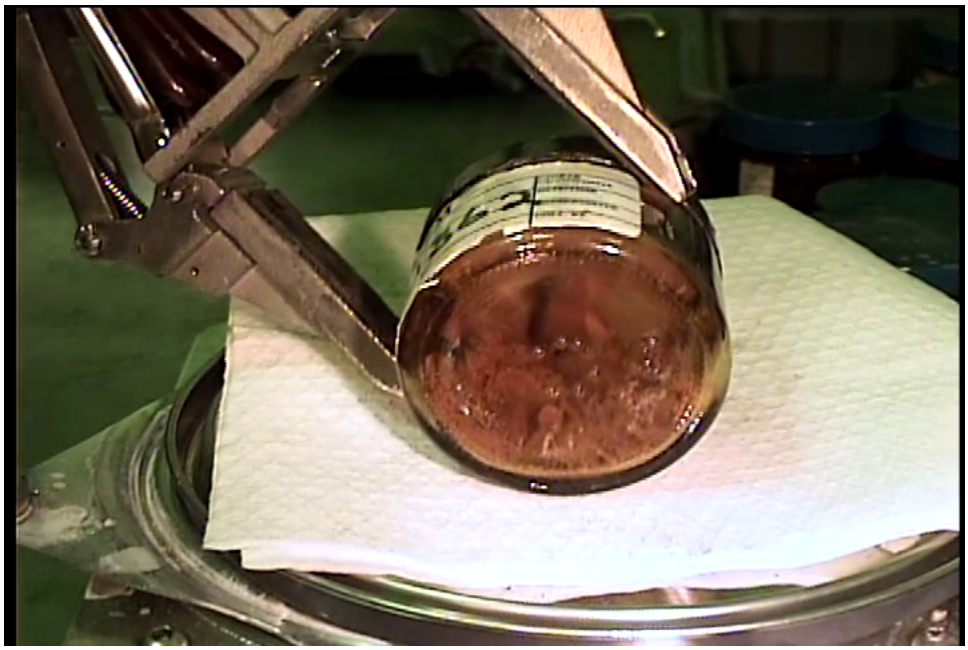


Figure A.50. Bottom view of Jar 21362 (Tank AN-106, Core Segment 339-20 UH)



Figure A.51. Solids view of Jar 21362 (Tank AN-106, Core Segment 339-20 UH)

A.18 Tank AN-106, Core Segment 339-21 UH

Tank: 241-AN-106
Core: 339
Segment: 21 UH
Jar: 21366
Lab ID: S20T018217
Initial Mass: 108.14 g
Final Mass: 107.82 g
Reference: RPP-RPT-63779 Rev.00



Figure A.52. Side view of Jar 21366 (Tank AN-106, Core Segment 339-21 UH)

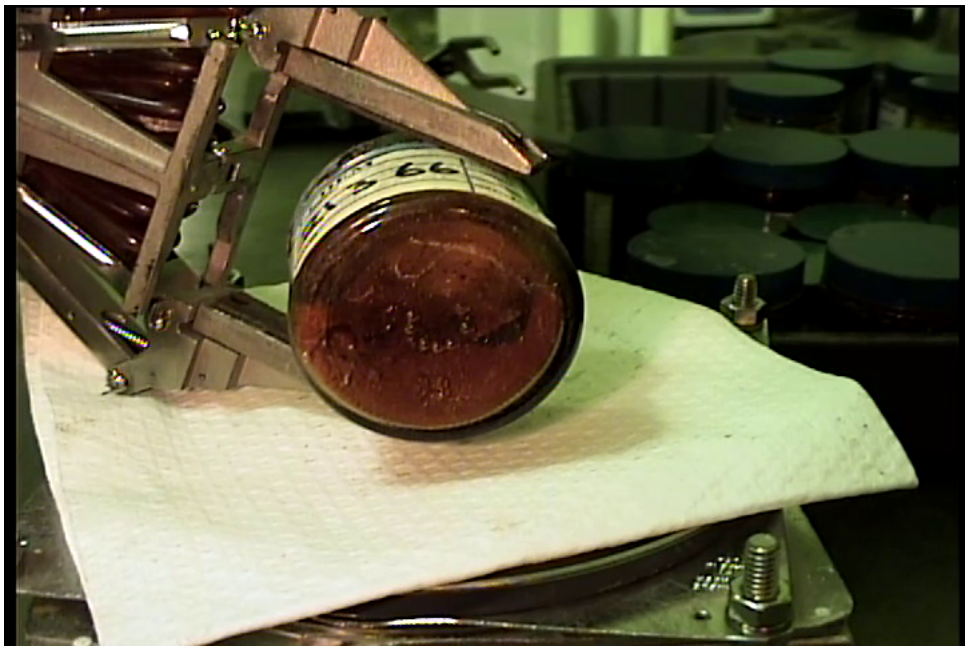


Figure A.53. Bottom view of Jar 21366 (Tank AN-106, Core Segment 339-21 UH)

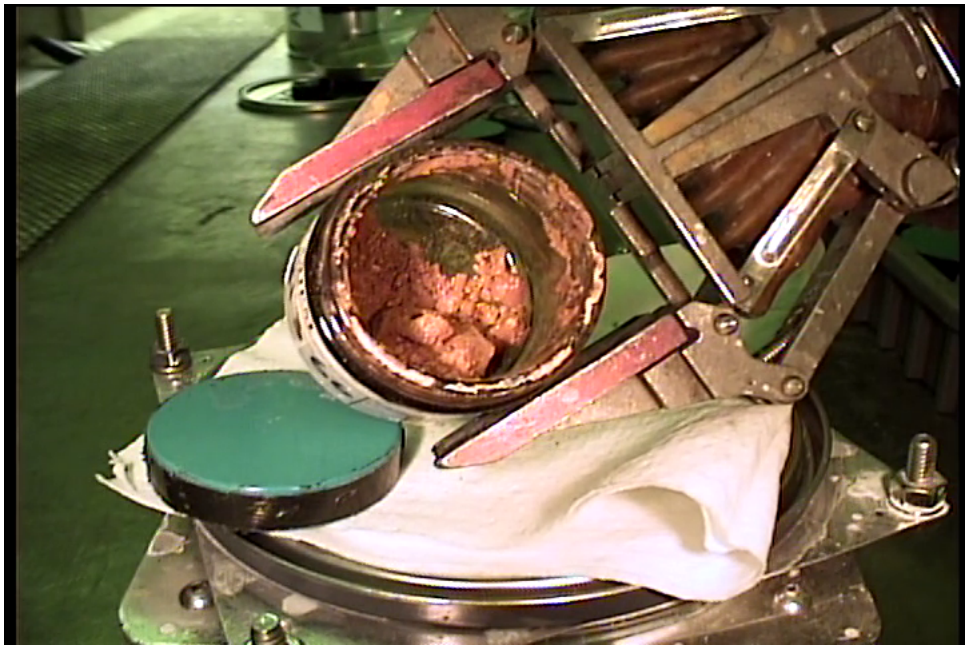


Figure A.54. Solids view of Jar 21366 (Tank AN-106, Core Segment 339-21 UH)

A.19 Tank AN-106, Core Segment 339-22 UH

Tank: 241-AN-106
Core: 339
Segment: 22 UH
Jar: 21367
Lab ID: S20T018254
Initial Mass: 120.83 g
Final Mass: 120.42 g
Reference: RPP-RPT-63779 Rev.00

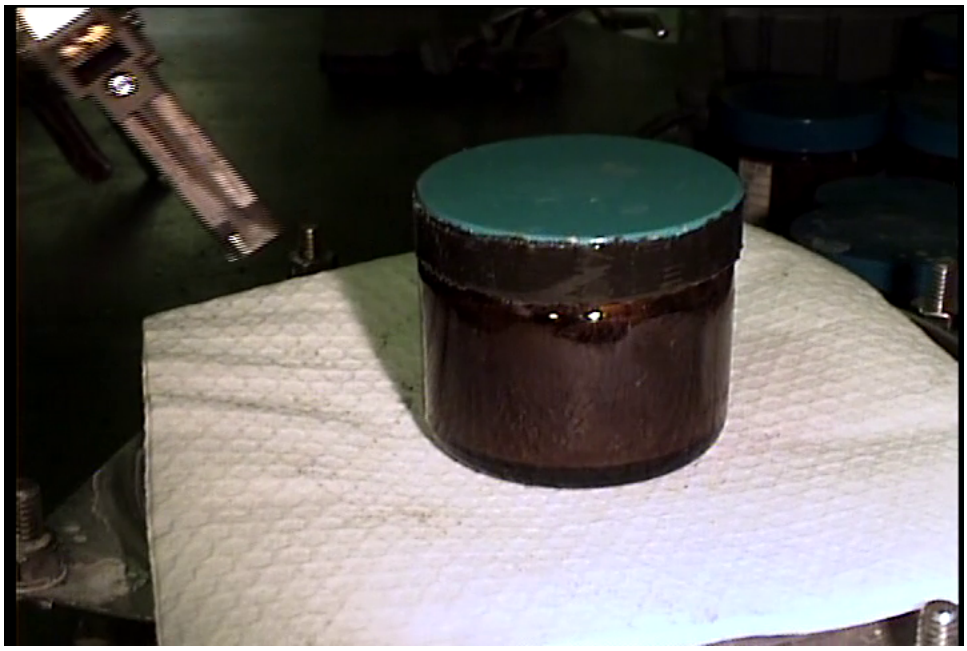


Figure A.55. Side view of Jar 21367 (Tank AN-106, Core Segment 339-22 UH)

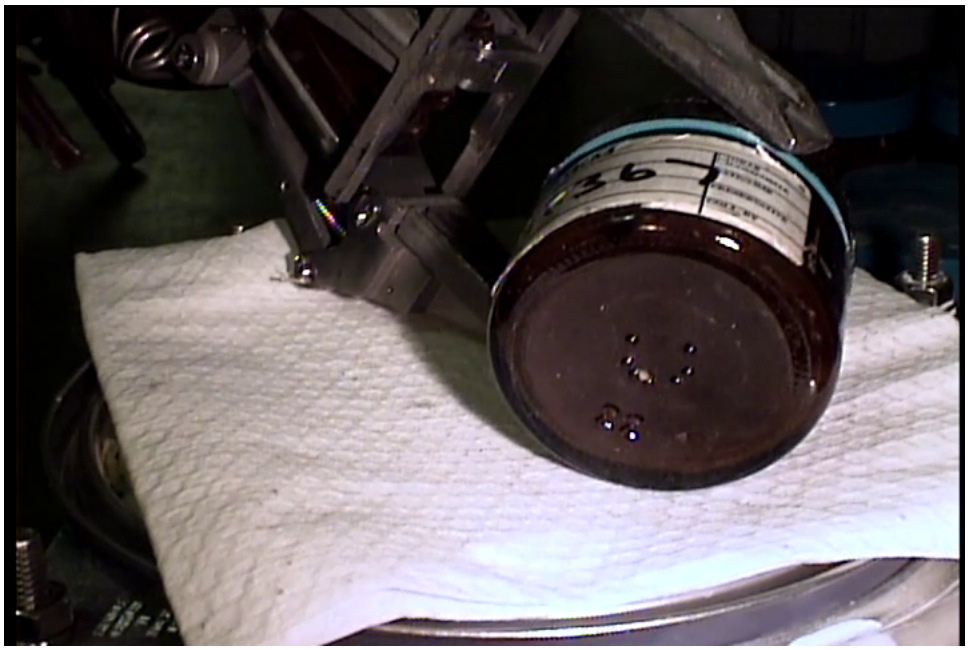


Figure A.56. Bottom view of Jar 21367 (Tank AN-106, Core Segment 339-22 UH)



Figure A.57. Solids view of Jar 21367 (Tank AN-106, Core Segment 339-22 UH)

A.20 Tank AW-105, Core Segment 322-8 LH

Tank: 241-AW-105
Core: 322
Segment: 8 LH
Jar: 19257
Lab ID: S06T000221
Initial Mass: 171.98 g
Final Mass: 171.98 g
Reference: RPP-RPT-42913, Rev.0



Figure A.58. Side view of Jar 19257 (Tank AW-105, Core Segment 322-8 LH)

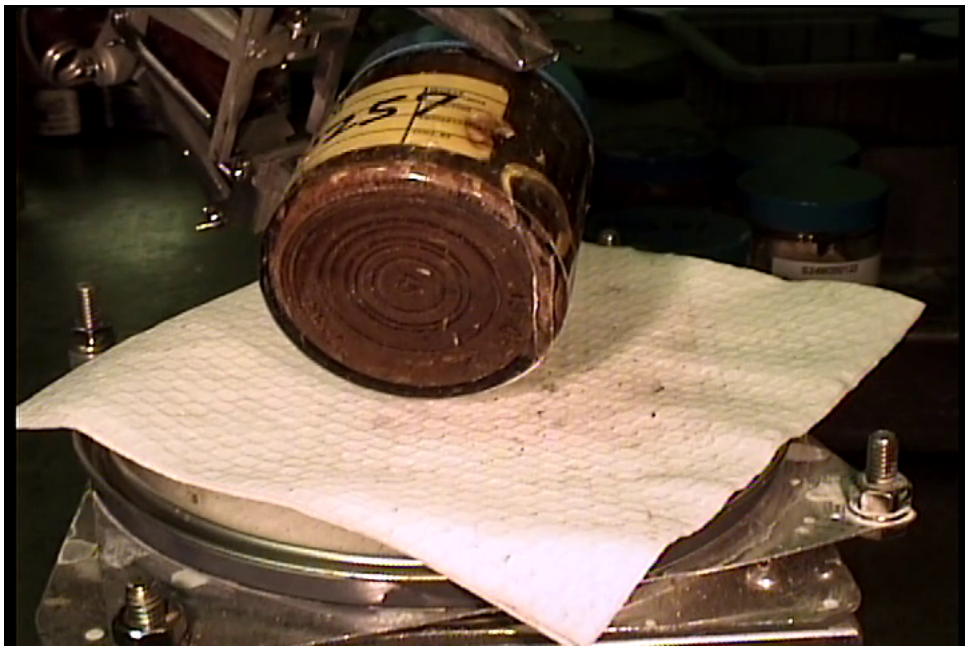


Figure A.59. Bottom view of Jar 19257 (Tank AW-105, Core Segment 322-8 LH)

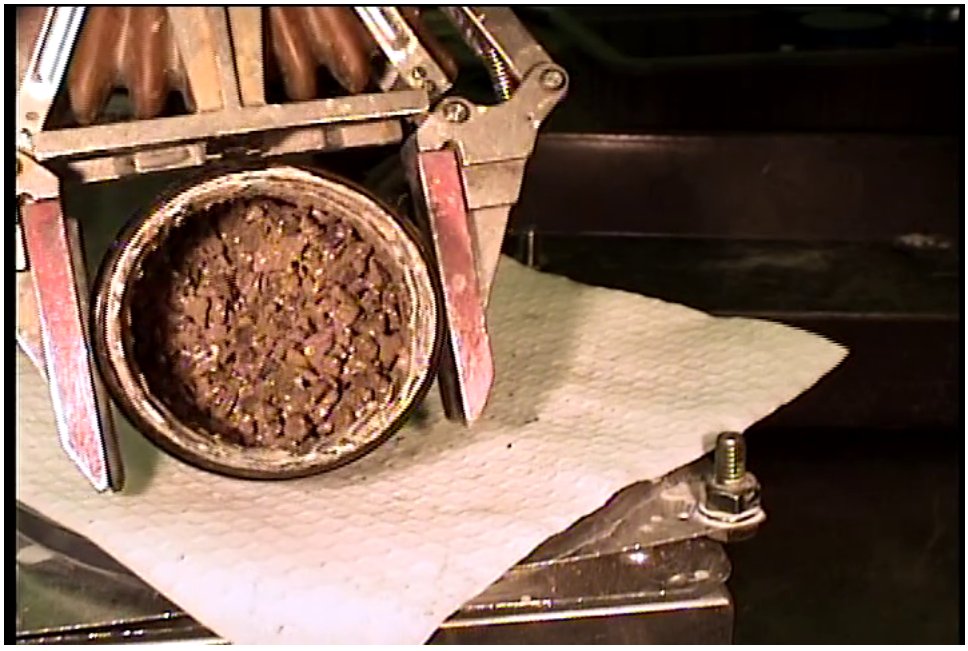


Figure A.60. Solids view of Jar 19257 (Tank AW-105, Core Segment 322-8 LH)

A.21 Tank AW-105, Core Segment 322-8 LH

Tank: 241-AW-105
Core: 322
Segment: 8 LH
Jar: 20326
Lab ID: S06T000217
Initial Mass: 117.95 g
Final Mass: 117.05 g
Reference: RPP-RPT-42913, Rev.0



Figure A.61. Side view of Jar 20326 (Tank AW-105, Core Segment 322-8 LH)



Figure A.62. Bottom view of Jar 20326 (Tank AW-105, Core Segment 322-8 LH)

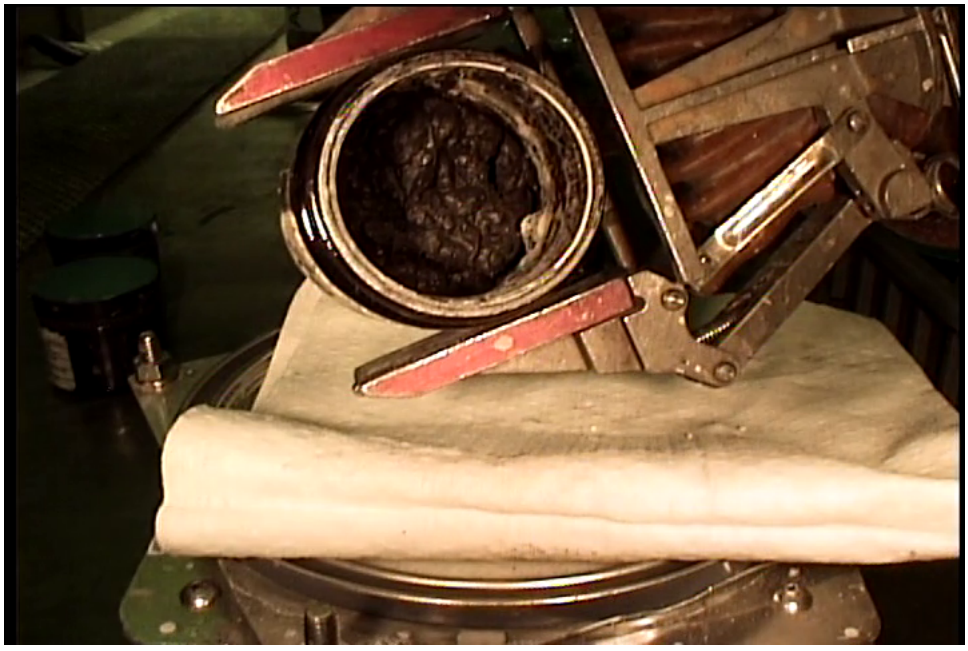


Figure A.63. Solids view of Jar 20326 (Tank AW-105, Core Segment 322-8 LH)

A.22 Tank AW-105, Core Segment 322-8 UH

Tank: 241-AW-105
Core: 322
Segment: 8 UH
Jar: 19262
Lab ID: S06T000220
Initial Mass: 179.87 g
Final Mass: 179.22 g
Reference: RPP-RPT-42913, Rev.0



Figure A.64. Side view of Jar 19262 (Tank AW-105, Core Segment 322-8 UH)

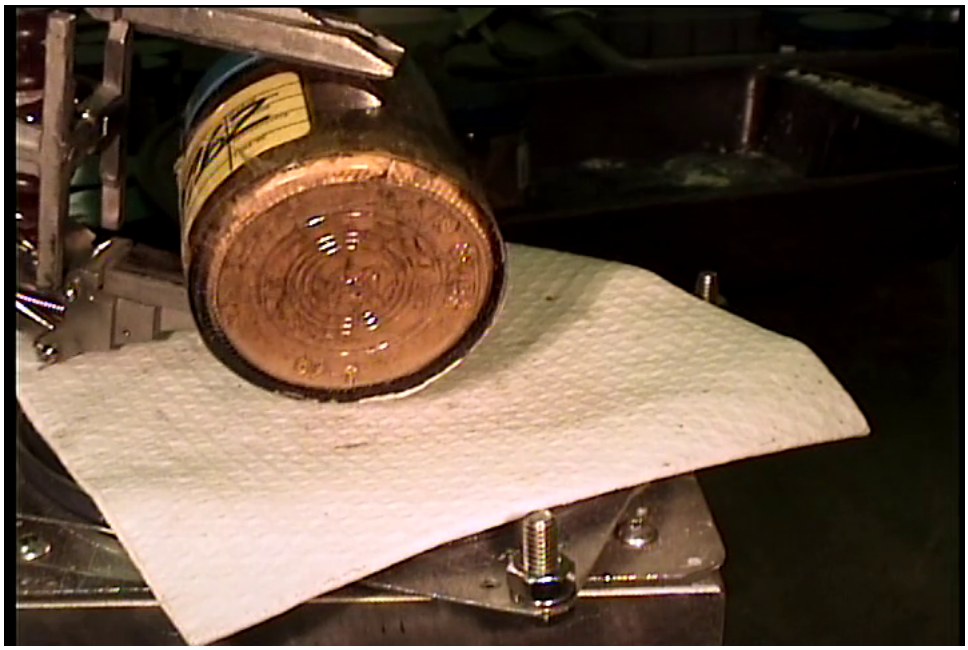


Figure A.65. Bottom view of Jar 19262 (Tank AW-105, Core Segment 322-8 UH)



Figure A.66. Solids view of Jar 19262 (Tank AW-105, Core Segment 322-8 UH)

A.23 Tank AW-105, Core Segment 322-8R2 CS 1

Tank: 241-AW-105
Core: 322
Segment: 8R2 CS 1
Jar: 20507-1
Lab ID: S08T009997
Initial Mass: 178.99 g
Final Mass: 178.99 g
Reference: RPP-RPT-42913, Rev.0

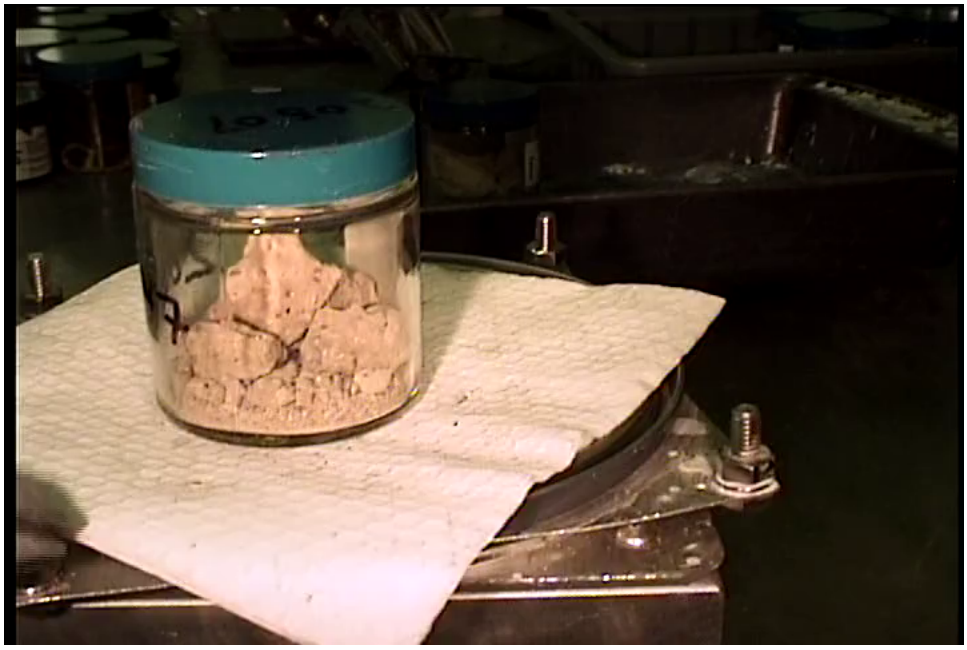


Figure A.67. Side view of Jar 20507-1 (Tank AW-105, Core Segment 322-8R2 CS 1)



Figure A.68. Bottom view of Jar 20507-1 (Tank AW-105, Core Segment 322-8R2 CS 1)



Figure A.69. Solids view of Jar 20507-1 (Tank AW-105, Core Segment 322-8R2 CS 1)

A.24 Tank AW-105, Core Segment 322-8R2 CS 2

Tank: 241-AW-105
Core: 322
Segment: 8R2 CS 2
Jar: 20507-2
Lab ID: S08T009997
Initial Mass: 173.65 g
Final Mass: 173.65 g
Reference: RPP-RPT-42913, Rev.0



Figure A.70. Side view of Jar 20507-2 (Tank AW-105, Core Segment 322-8R2 CS 2)



Figure A.71. Bottom view of Jar 20507-2 (Tank AW-105, Core Segment 322-8R2 CS 2)

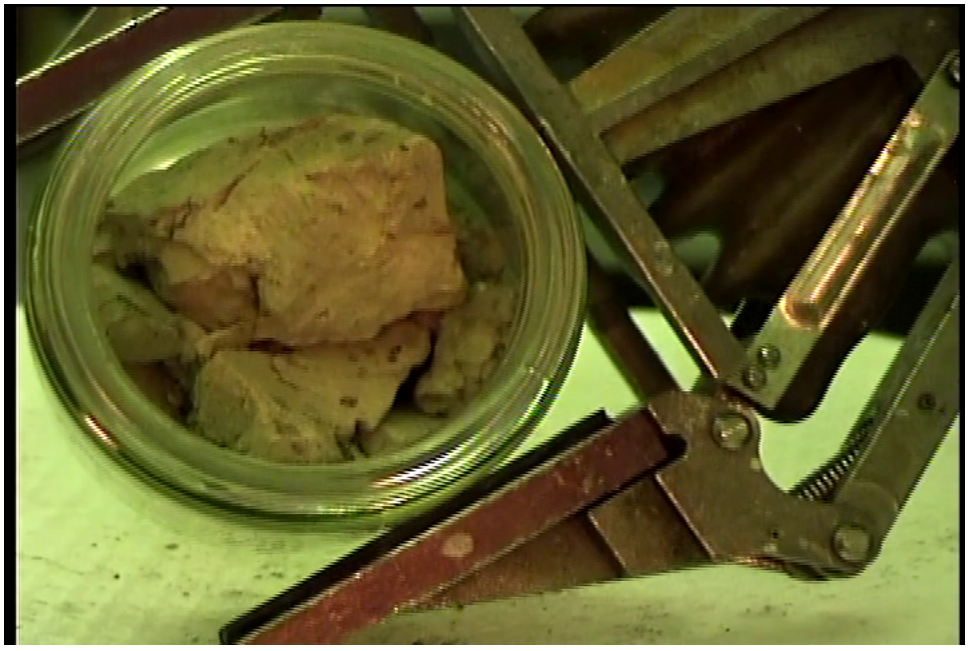


Figure A.72. Solids view of Jar 20507-2 (Tank AW-105, Core Segment 322-8R2 CS 2)

Appendix B – Composite Settling Curves

This appendix presents the full set of settling data measured during the characterization of the five SE quadrant composites. Figures B.1 through B.5 provide settling curves at various UDS contents for individual composites. Figures B.6 through B.9 show grouped settling curves at fixed UDS concentrations, ranging from nominal values of 5 to 20 %. Settling curve behaviors are discussed in greater detail in the main body of the report (see Section 6) and will not be analyzed further in this appendix.

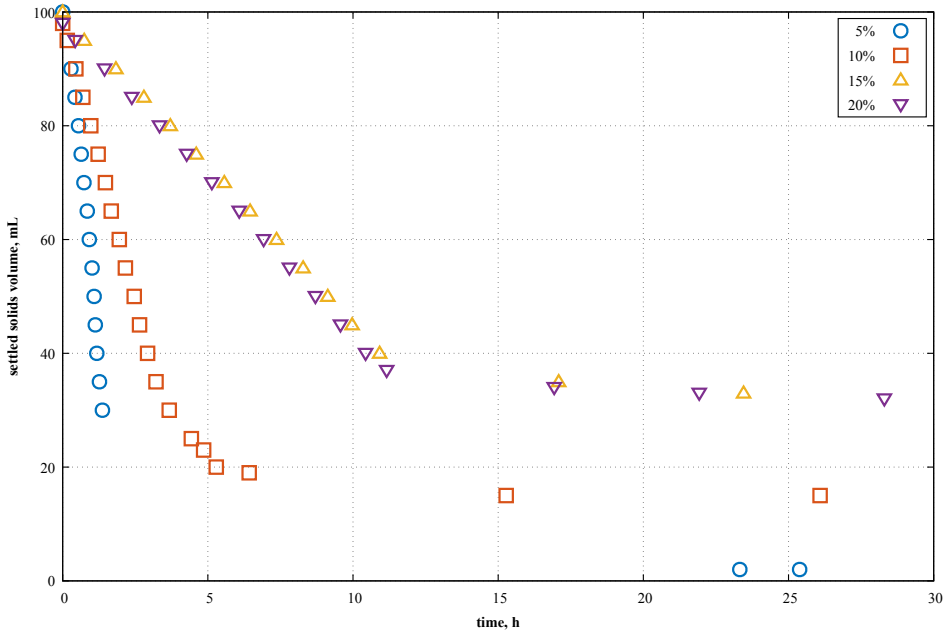


Figure B.1. Measured settling curves for Al composites.

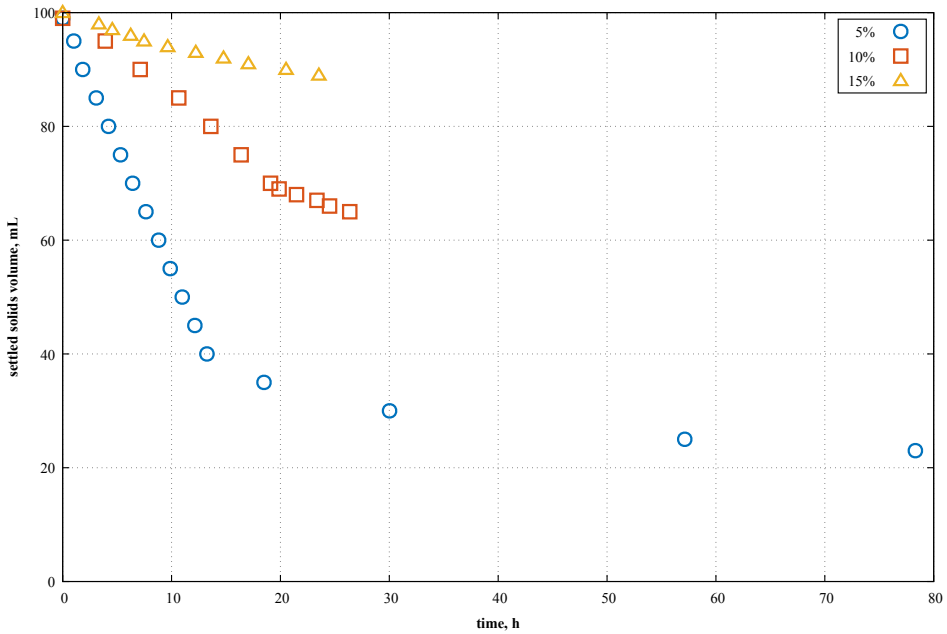


Figure B.2. Measured settling curves for Fe composites. The rate at 20 % was not measured.

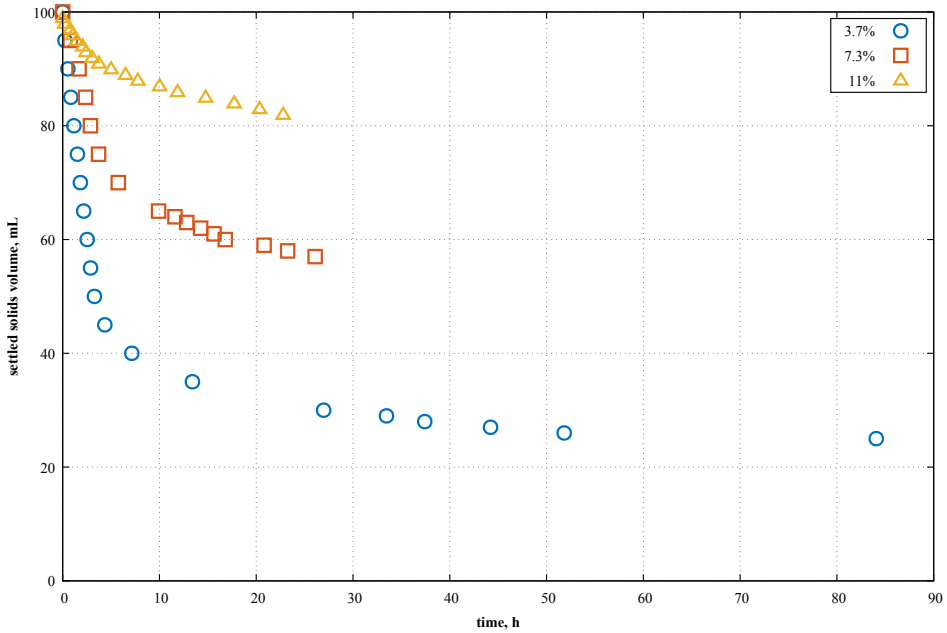


Figure B.3. Measured settling curves for PO_4 composites. The rate at 20 % was not measured.

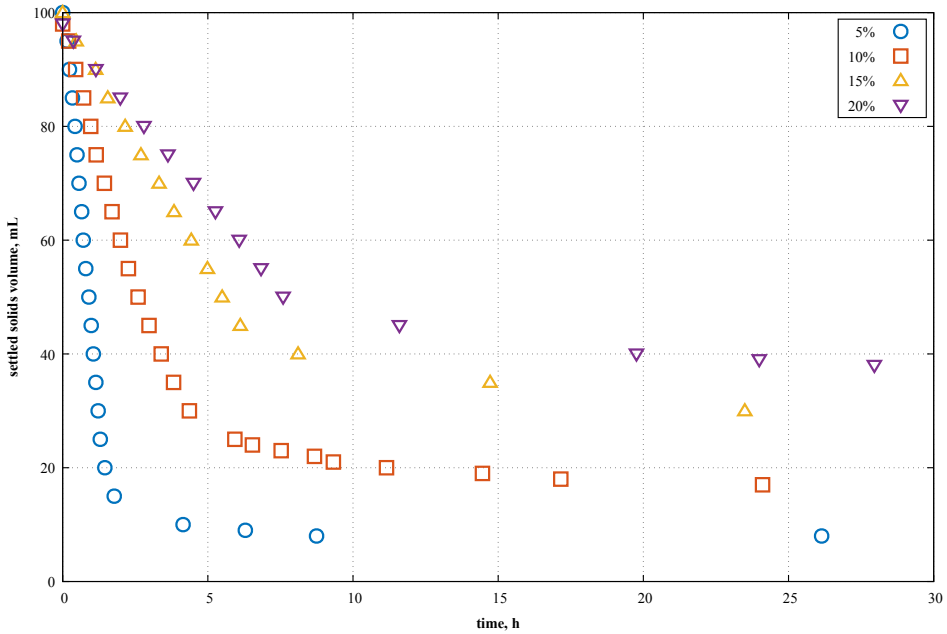


Figure B.4. Measured settling curves for U composites.

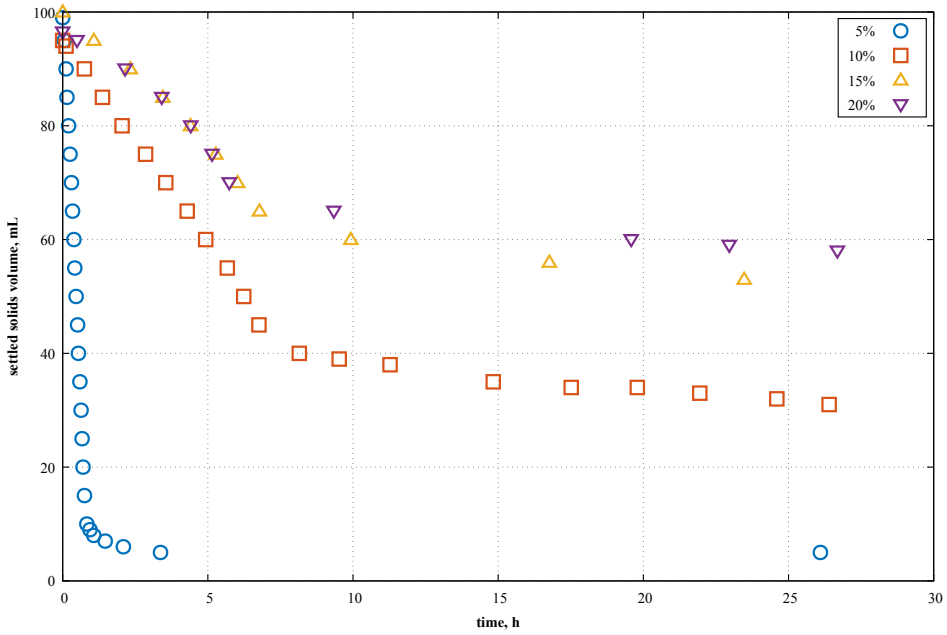


Figure B.5. Measured settling curves for Zr composites.

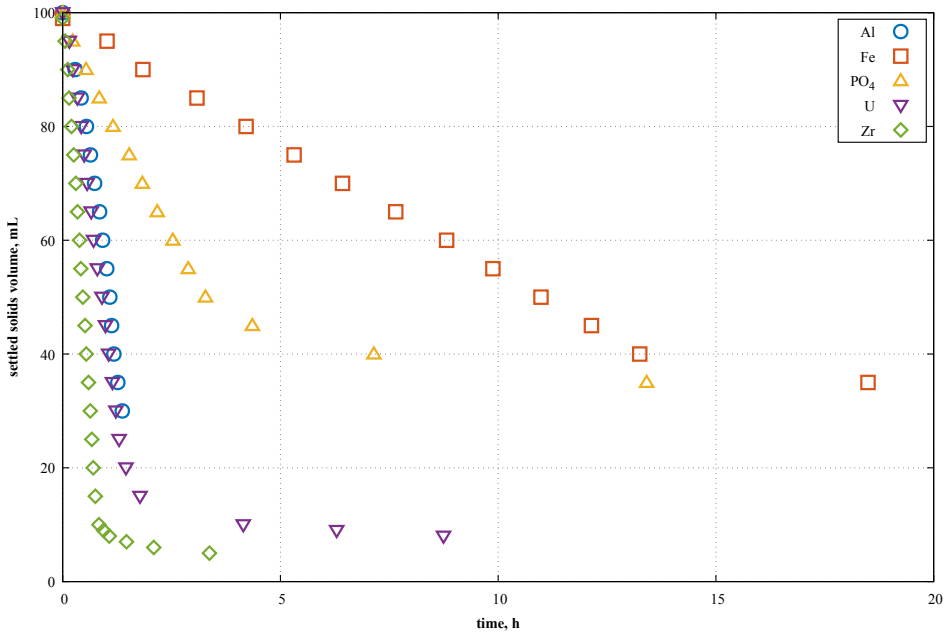


Figure B.6. Measured settling curves for all nominally 5 % composites. All slurry UDS contents were approximately 5 % except the PO_4 slurry, which was 3.7 %.

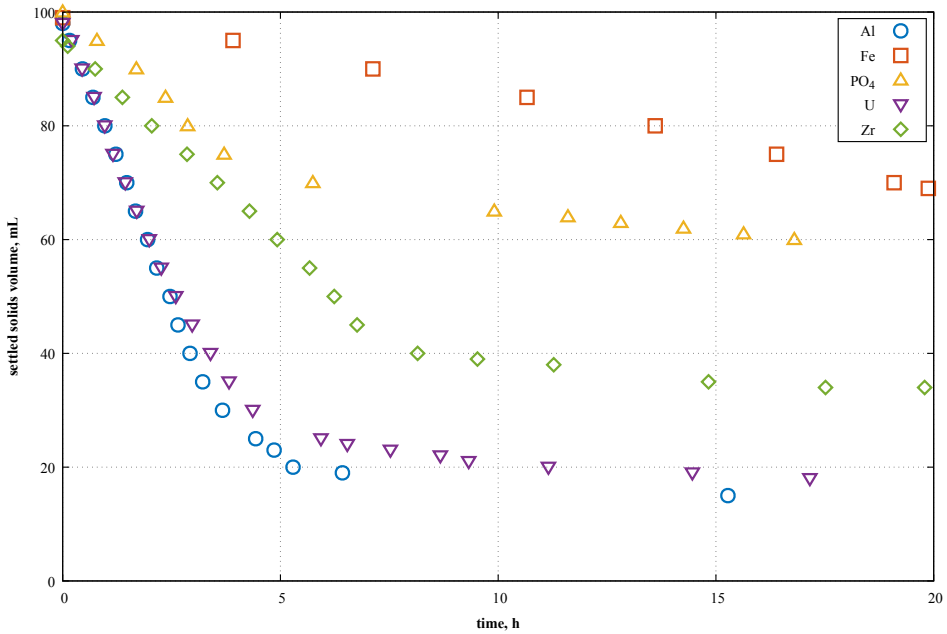


Figure B.7. Measured settling curves for all nominally 10 % composites. All slurry UDS contents were approximately 10 % except the PO_4 slurry, which was 7.3 %.

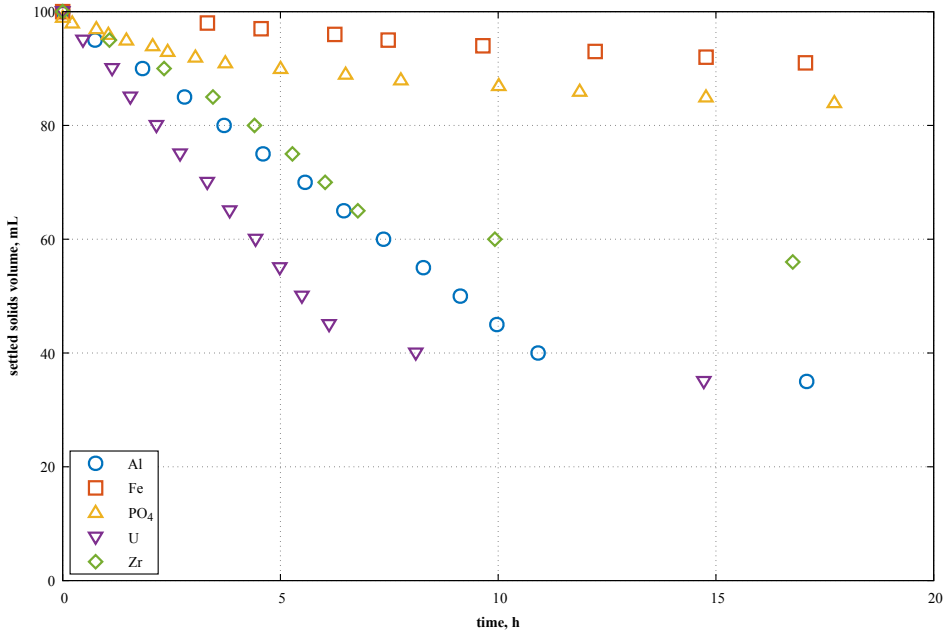


Figure B.8. Measured settling curves for all nominally 15 % composites. All slurry UDS contents were approximately 15 % except the PO_4 slurry, which was 11.0 %.

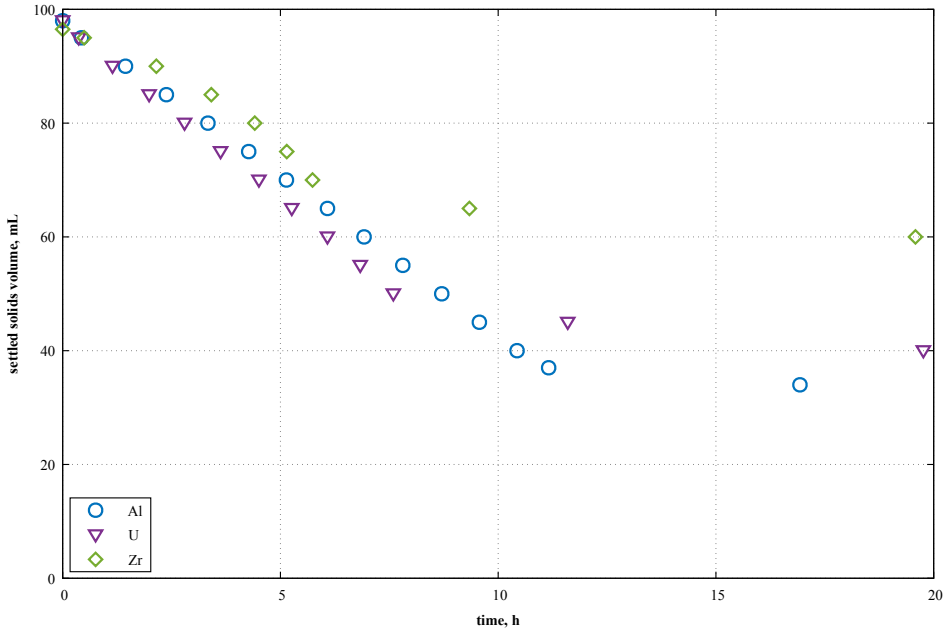


Figure B.9. Measured settling curves for all nominally 20 % composites. Settling curves for the Fe and PO_4 composites were not quantified due to limited settling over the 24 h period.

Appendix C – Composite Flow Curves

This appendix provides a summary of the measured flow curve "down-ramps" (typically 1000 to 0 s^{-1}) used to determine the constitutive parameters listed in Table 24. Flow curves were measured for most, but not all, composite and UDS combinations. Table C.1 summarizes the measured conditions. In general, low solids content Al and U flow curves were forgone due to their Newtonian behavior and similarity of their viscosity to their supernatant. Figures C.1 to C.16 show the measured decelerating rate flow curves for these measured combinations. Composite UDS matched the listed nominal value for all composites but PO_4 (see Table 20). All flow curves were generally measured using the 1 mm gap M5-MV1 concentric cylinder viscometer system discussed in Section 5. Select measurements at 20 % UDS content were measured with a 2 mm MV2 measuring system due to concerns about particle jamming in the annular measuring gap. Measurements made with the MV2 geometry are noted in their respective figure captions.

Table C.1. Summary of measured flow curves for the SE quadrant composites. Conditions marked with "X" were measured. Conditions marked with "–" were not.

Nominal UDS	Composite				
[%]	Al	Fe	PO_4	U	Zr
5	–	X	X	–	X
10	–	X	X	–	X
15	X	X	X	X	X
20	X	X	X	X	X

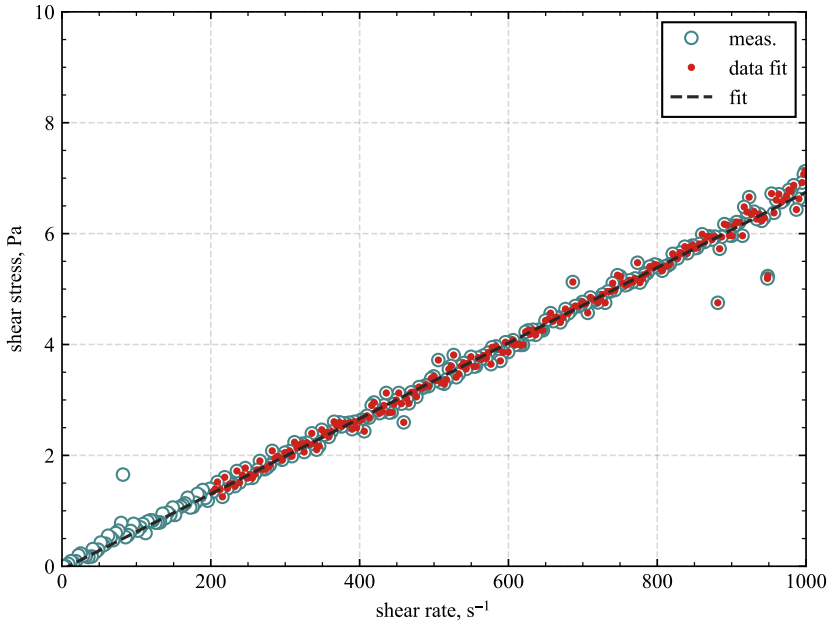


Figure C.1. Measured down-ramp flow curve for the 5 % UDS Fe composite.

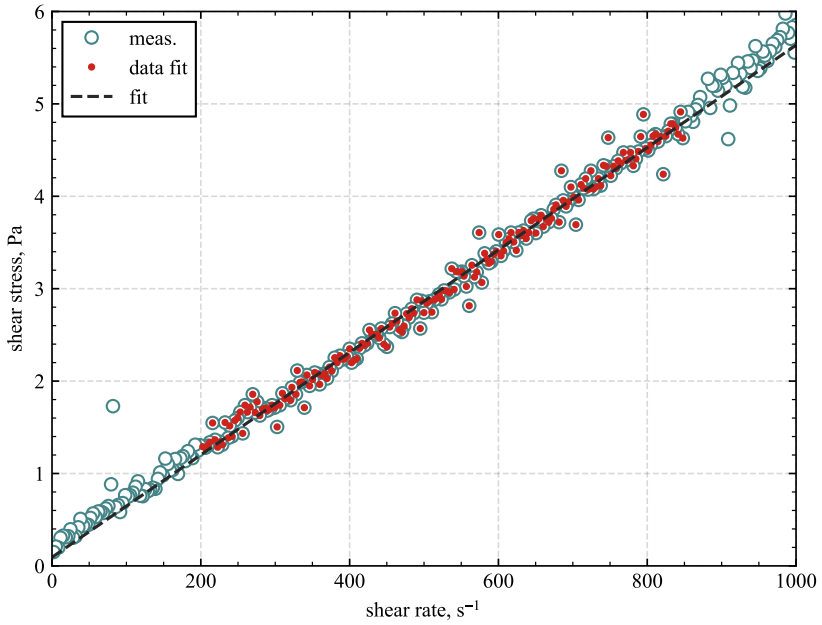


Figure C.2. Measured down-ramp flow curve for the 3.7 % UDS PO_4 composite.

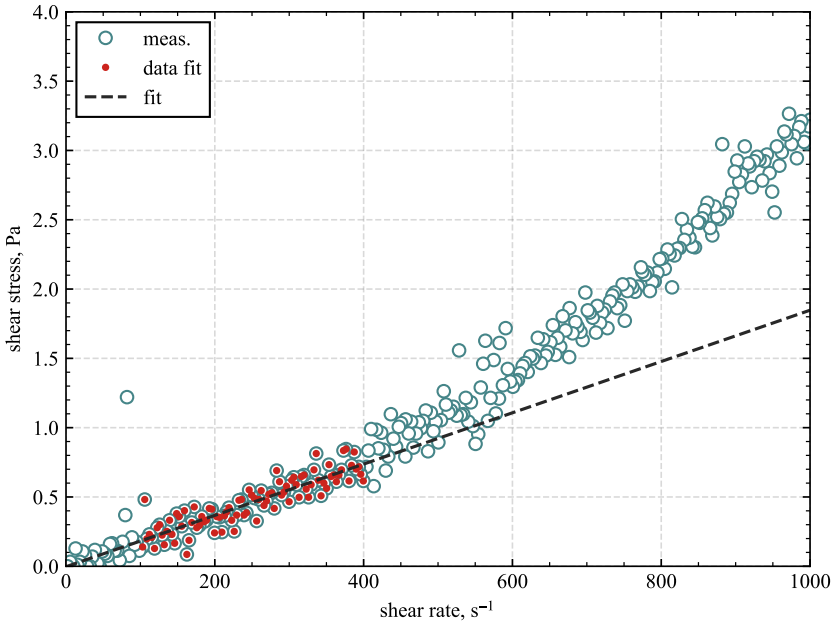


Figure C.3. Measured down-ramp flow curve for the 5 % UDS Zr composite.

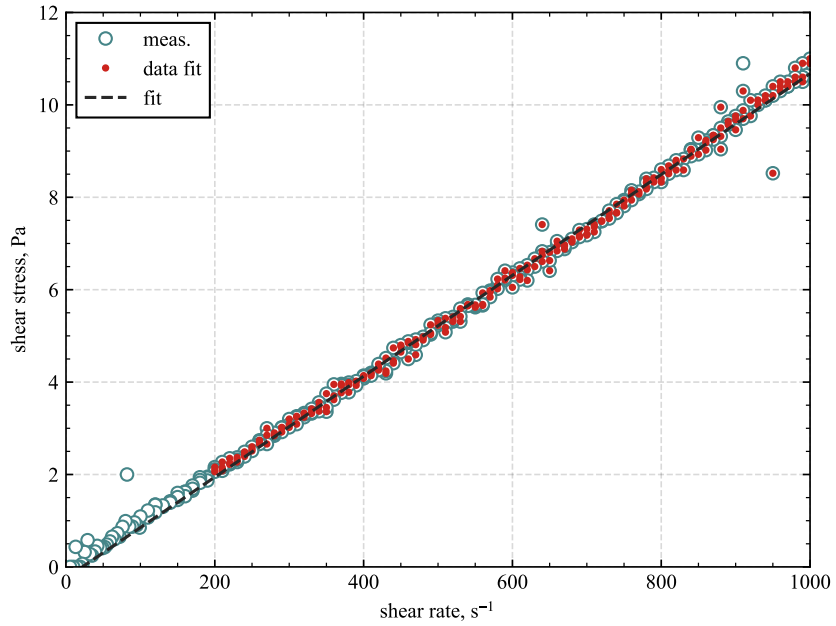


Figure C.4. Measured down-ramp flow curve for the 10 % UDS Fe composite.

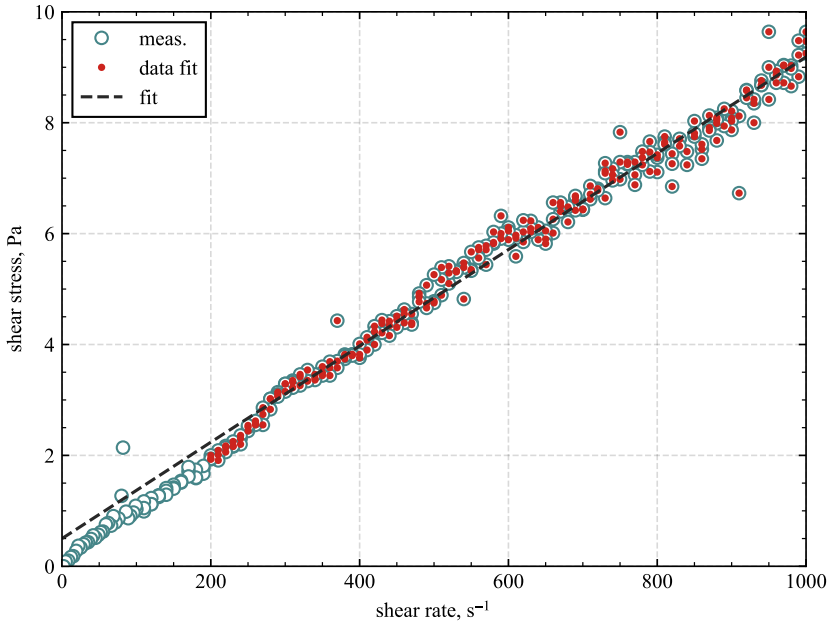


Figure C.5. Measured down-ramp flow curve for the 7.3 % UDS PO_4 composite.

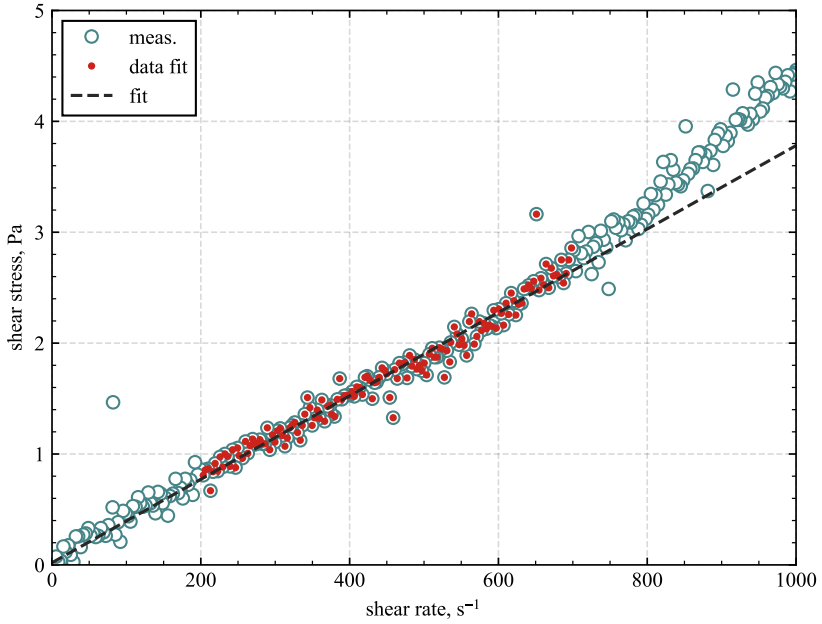


Figure C.6. Measured down-ramp flow curve for the 10 % UDS Zr composite.

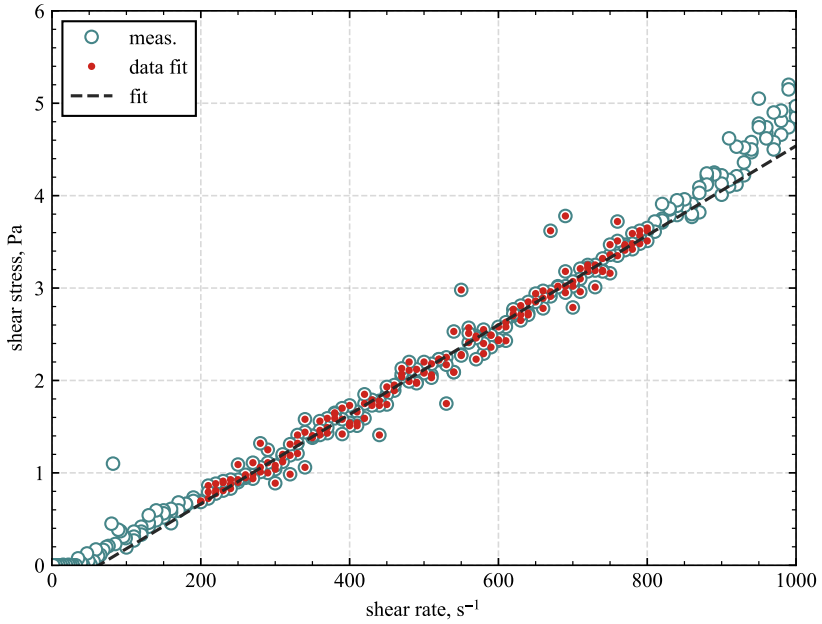


Figure C.7. Measured down-ramp flow curve for the 15 % UDS Al composite.

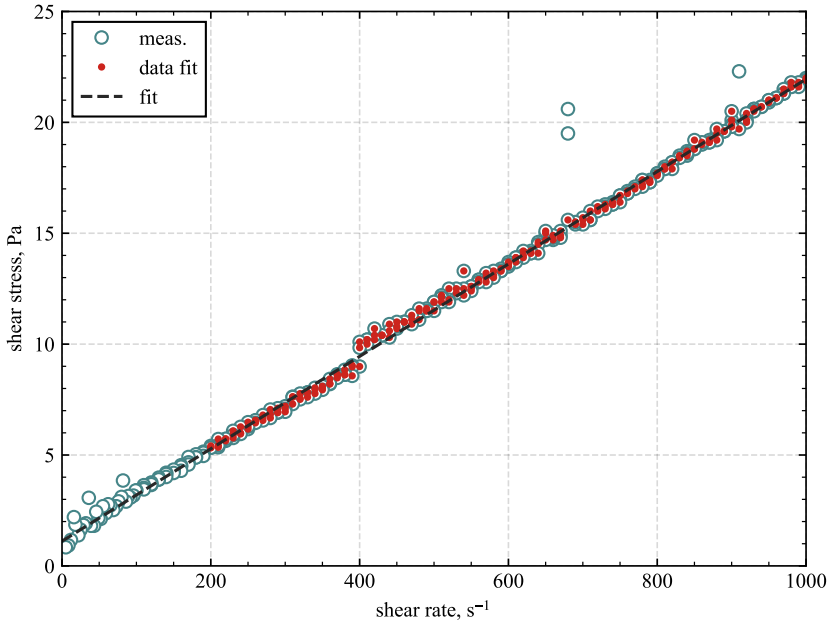


Figure C.8. Measured down-ramp flow curve for the 15 % UDS Fe composite.

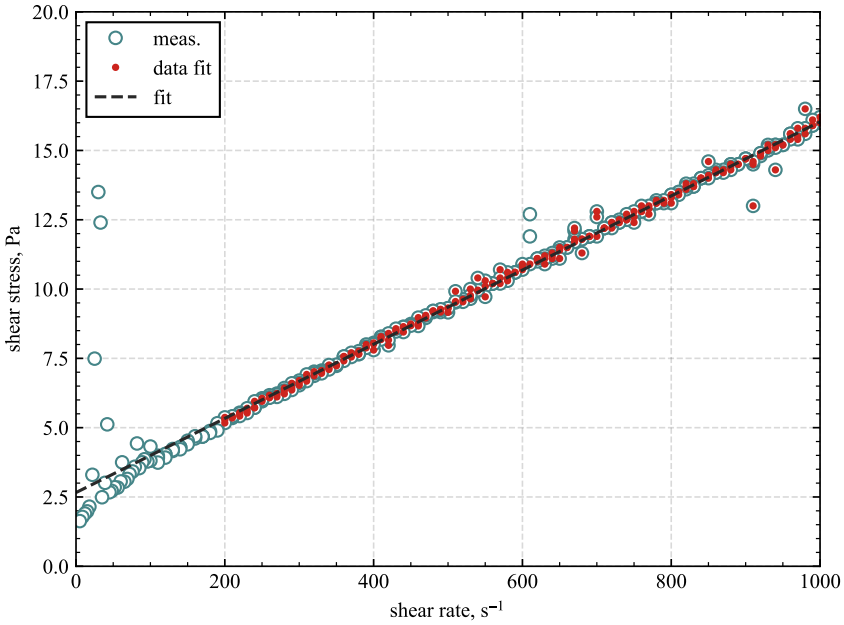


Figure C.9. Measured down-ramp flow curve for the 11.0 % UDS PO_4 composite.

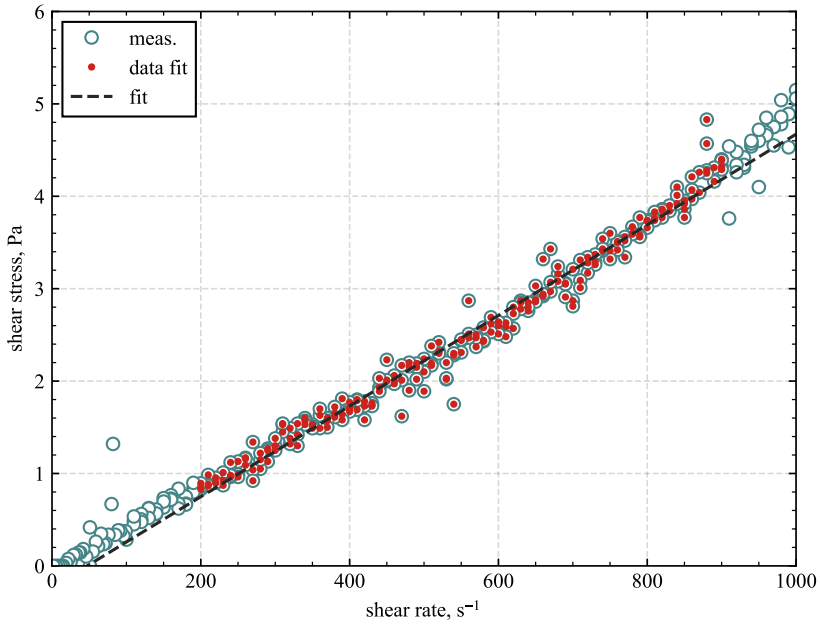


Figure C.10. Measured down-ramp flow curve for the 15 % UDS U composite.

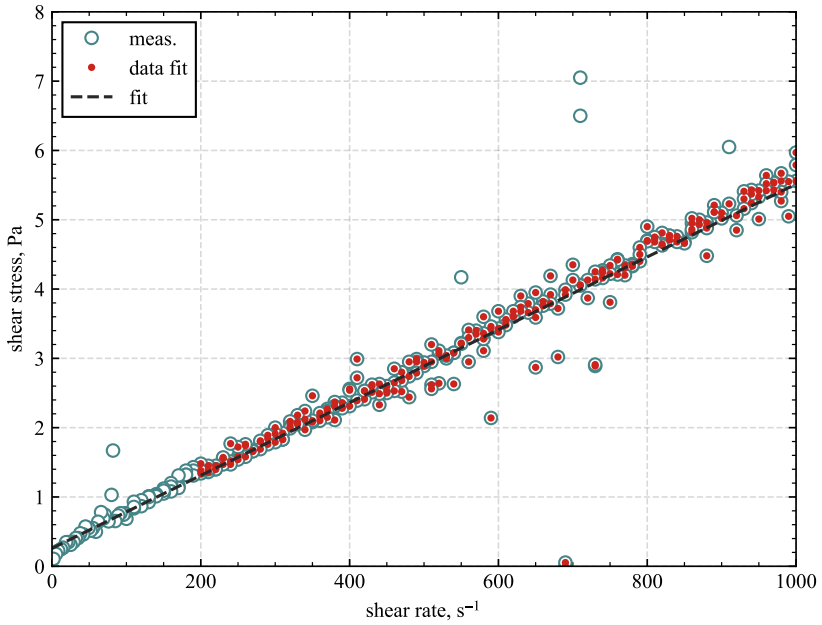


Figure C.11. Measured down-ramp flow curve for the 15 % UDS Zr composite.

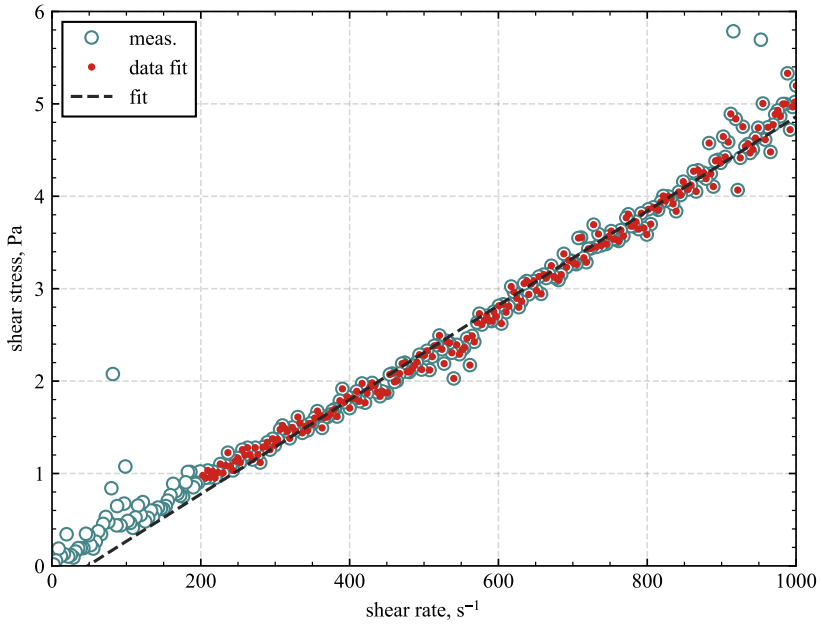


Figure C.12. Measured down-ramp flow curve for the 20 % UDS Fe composite.

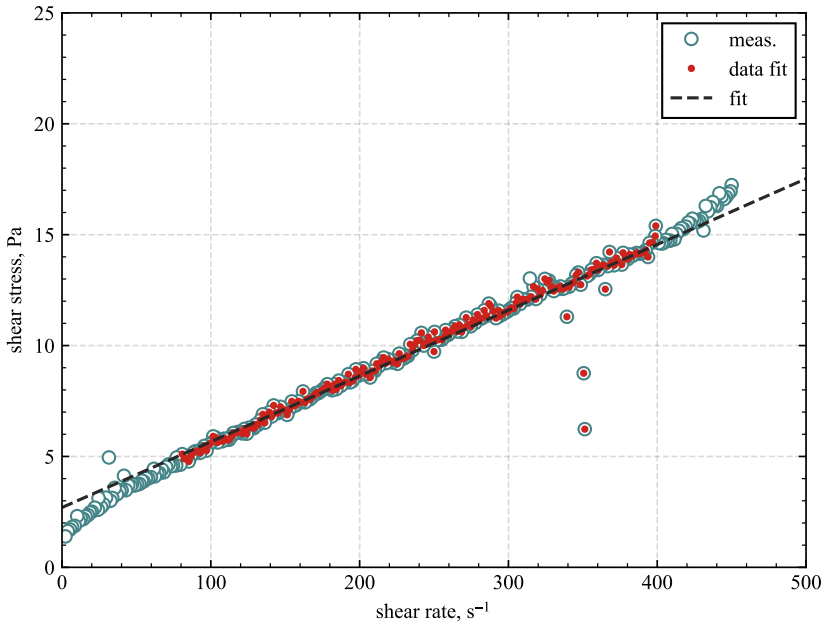


Figure C.13. Measured down-ramp flow curve for the 20 % UDS Fe composite. Measurement used the MV2 measuring geometry.

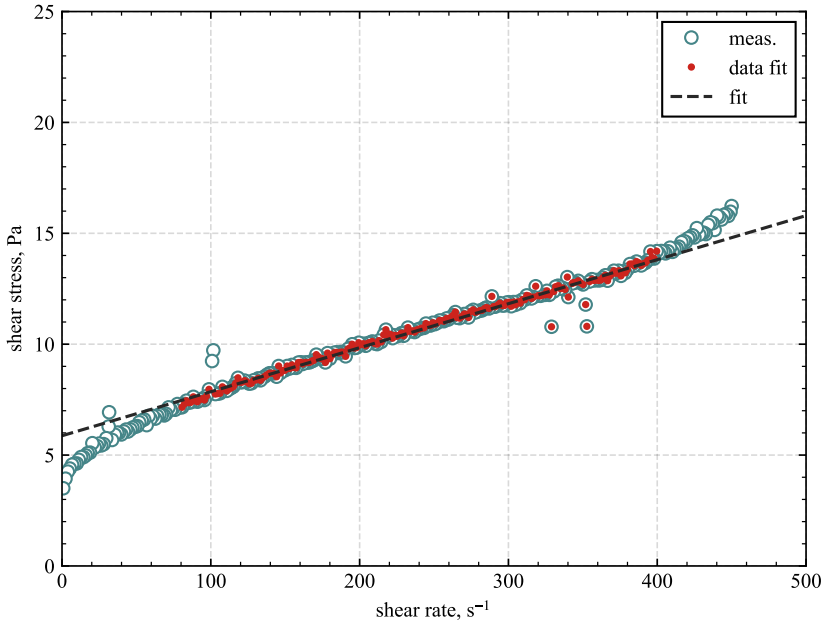


Figure C.14. Measured down-ramp flow curve for the 14.6 % UDS PO_4 composite. Measurement used the MV2 measuring geometry.

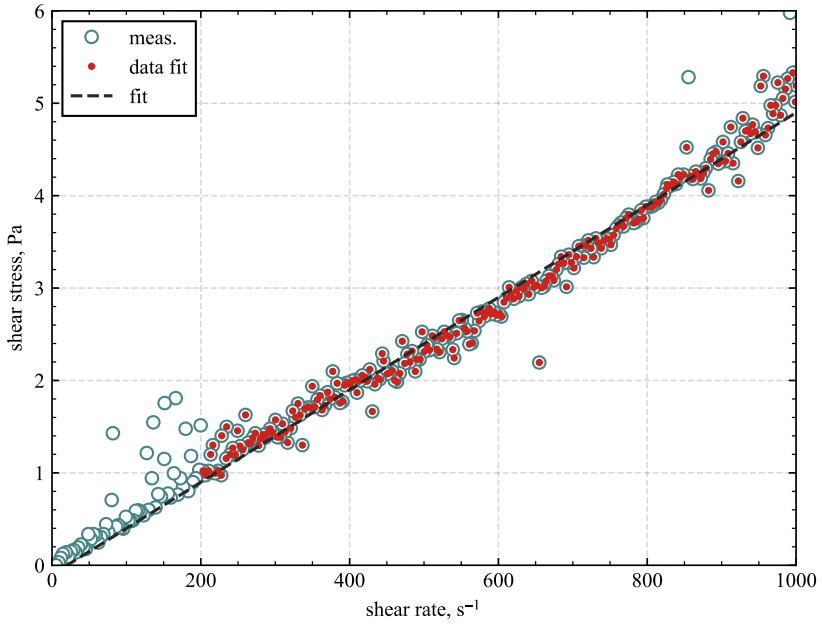


Figure C.15. Measured down-ramp flow curve for the 20 % UDS U composite.

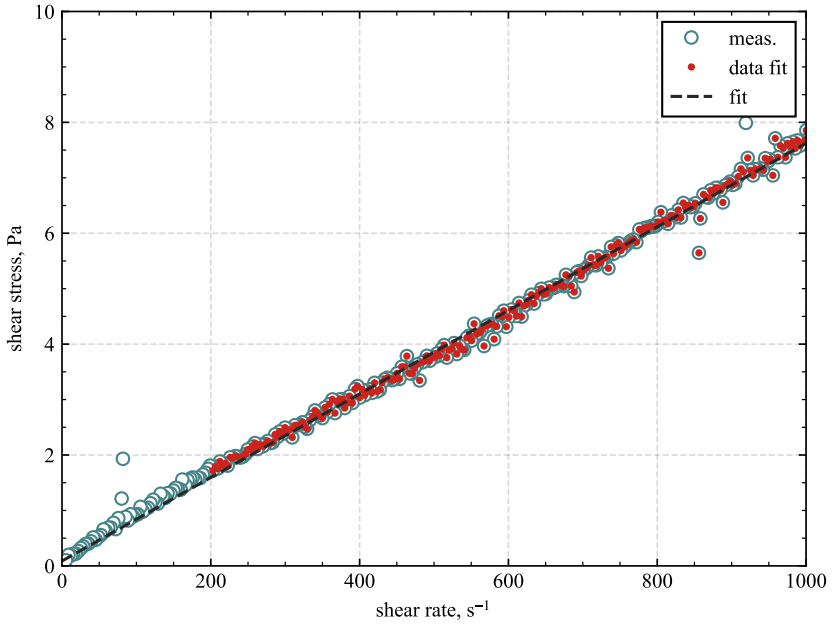


Figure C.16. Measured down-ramp flow curve for the 20 % UDS Zr composite.

Pacific Northwest National Laboratory

902 Battelle Boulevard
P.O. Box 999
Richland, WA 99354

1-888-375-PNNL (7665)

www.pnnl.gov